DISSERTATION

SEASONAL, SYNOPTIC, AND INTRASEASONAL VARIABILITY OF THE WEST AFRICAN MONSOON

Submitted by

Rachel Rose McCrary

Department of Atmospheric Science

In partial fulfillment of the requirements

For the Degree of Doctor of Philosophy

Colorado State University

Fort Collins, CO

Fall 2012

Doctoral Committee:

Advisor: David A. Randall

A. Scott Denning
Susan C. van den Heever
Michele Betsill

ABSTRACT

SEASONAL, SYNOPTIC, AND INTRASEASONAL VARIABILITY

OF THE WEST AFRICAN MONSOON

The simulation of the West African monsoon is examined in two coupled general circulation models (CGCMs). The first model is the standard Community Climate System Model (CCSM) which uses traditional parameterizations to represent convective processes. The second model is the superparameterized-CCSM (SP-CCSM), in which convective parameterizations have been replaced by embedding a two-dimensional cloud resolving model into each gridbox. Superparameterization is intended to improve simulation of the complex multiscale interactions that occur between the large-scale environment and clouds.

Key features of West African climate are analyzed in both models including: the mean annual cycle of the monsoon, African easterly wave (AEW) activity and dynamics, and the intraseasonal modulation of precipitation. Adding superparameterization improves the position and intensity of the summer maximum in precipitation which is shifted from over the Gulf of Guinea in CCSM (not realistic), to over the continent in SP-CCSM which is in keeping with the observations. AEWs and their relationship with convection are also improved in the SP-CCSM: In the standard model, little to no easterly wave activity occurs over West Africa, and the relationship with convection is tenuous at best. SP-CCSM on the other hand produces strong AEWs over the region that exhibit similar horizontal and vertical structures to observations. AEWs in SP-CCSM are strongly coupled to convection, more so than is supported by

observations. An examination of the energetics of the simulated AEWs suggests that convection drives the generation and propagation the waves in SP-CCSM. Consistent with observations, intraseasonal variations in West African precipitation in SP-CCSM appear to be linked to variations in convection in the Indo-Pacific region corresponding with the MJO and the Indian monsoon. Because of these physically-realistic relationships, SP-CCSM has potential to deepen our understanding of the teleconnections between the MJO and West Africa, helping to improve seasonal rainfall forecasts.

ACKNOWLEDGEMENTS

I would like to thank my advisor, Dr. David A. Randall, for his support and enthusiasm. Without his constant faith in my abilities and his never ending patience, this dissertation would not have been possible. I would also like to thank my committee members, Dr. A. Scott Denning, Dr. Susan C. van den Heever, and Dr. Michele Betsill for taking the time to read and review this dissertation.

Special thanks is owed to both the Randall and Maloney research groups. I would particularly like to thank Mark Branson for his endless help with supercomputers and model simulations. Thank you to Gus Alaka, Dr. Jim Benedict and Dr. Charlotte DeMott for helping me understand tropical convection and waves. Special thanks to Dr. George Kiladis and Dr. Eric Maloney for taking the time to meet with me and for their enthusiasm about my research.

I wish to thank Dr. Cristiana Stan at George Mason University for providing the CCSM3 and SP-CCSM model output used in this dissertation. I would also like to acknowledge the World Climate Research Programme's Working Group on Coupled Modelling, which is responsible for CMIP, and I thank the climate modeling groups (listed in Table 2.1 of this dissertation) for producing and making available their model output. For CMIP the U.S. Department of Energy's Program for Climate Model Diagnosis and Intercomparison provides coordinating support and led development of software infrastructure in partnership with the Global Organization for Earth System Science Portals.

I would also like to thank the funding agencies that made this work possible. This research was supported in part by the National Science Foundation Science and Technology Center for MultiScale Modeling of Atmospheric Processes, managed by Colorado State

University under cooperative agreement ATM-0425247. This research was also supported by the National Science Foundation managed by Colorado State University under agreement AGS-1049041.

Last but not least, I would like to thank my friends and family. To my parents, my sister, and my best friends Erika, your willingness to believe in me and your constant support throughout my life has made me the person that I am today. Without you I would not have been able to achieve this goal. To all of my friends who have gone through this process with me, thank you for all of the wonderful distractions from school and thank you for being there to commiserate about how difficult the path to the PhD. can be. To my partner Ben, thank you for brining joy and happiness into my life during a time when all I could think about was work. But most of all, thank you for dealing with my "crazy" for the past few years. As I have promised, things will only get better from this point forward.

TABLE OF CONTENTS

ABSTRACT....ii
ACKNOWLEDGEMENTS....iv
TABLE OF CONTENTS....vi

CHAPTER 1: INTRODUCTION....1
CHAPTER 2: DATA AND MODELS....13
2.1 MODEL SIMULATIONS....13
2.2 ADDITIONAL SIMULATIONS....15
2.3 OBSERVATIONAL DATASET....17
CHAPTER 3: THE SEASONAL CYCLE OF THE MONSOON....20
3.1 INTRODUCTION....20
3.2 MODELS AND OBSERVATIONS....22
3.3 PRECIPITATION AND LOW LEVEL WINDS....23
3.3.a Observations....23
3.3.b SP-CCSM and CCSM....28
3.3.c Comparison with CMIP5 models....31
3.4 SAHARAN HEAT LOW....32
3.5 AFRICAN EASTERLY JET....34
3.6 AFRICAN EASTERLY WAVES....36
3.7 CONCLUSIONS....38
3.8 FIGURES....40
CHAPTER 4: AFRICAN EASTERLY WAVES....57
4.1 INTRODUCTION....57
4.2 DATA AND METHODOLOGY....60
4.3 AEW VARIABILITY....63
4.4 AEW STRUCTURE....67
4.4.a Basepoint 10ºN, 10ºW....67
4.4.a.i Horizontal Structure....67
4.4.a.ii Vertical Structure....70
4.4.b Basepoint 15ºN, 17.5ºW....73
4.4.b.i Horizontal Structure....73
4.4.b.ii Vertical Structure....74
4.5 ENERGETICS OF AEWs....75
4.6 DISCUSSION....85
4.7 FIGURES....88
CHAPTER 5: INTRASEASONAL VARIABILITY....117
5.1 INTRODUCTION....117
5.2 VARIABILITY OF WEST AFRICAN MONSOON PRECIPITATION....119
5.2.a Mean and Variance Fields....119
5.2.b Power Spectra....122

5.2.c Relationship with the Global MJO Signature....123
5.3 SPATIAL-STRUCTURE OF 30-90 DAY VARIABILITY....124
5.4 RELATIONSHIP WITH CONVECTION OVER THE INDO PACIFIC....127
5.5 CONCLUSIONS....128
5.6 FIGURES....130
CHAPTER 6: CONCLUSIONS AND DISCUSSION....143
REFERENCES....149

CHAPTER 1

INTRODUCTION

West Africa is typically defined as the portion of the African continent that is north of the Equator and that curves westward into the Atlantic Ocean. This region experiences both the distinct seasonal shift in the prevailing winds and the alternation between winter dry conditions and summer rainy conditions that are characteristic of monsoon climates (e.g. Janicot et al., 2011). The sharp seasonal differences in low-level winds and rainfall in the so-called West African Monsoon are shown in Figure 1.1. This figure illustrates that during winter, West Africa is influenced by dry northeasterly winds coming from the Sahara Desert and experiences little-to-no rainfall. In contrast, the summer season is characterized by low-level southwesterly winds and high rainfall rates (Hall and Peyrille, 2006).

Monsoon rains are the lifeblood of people living in West Africa, and their cultures and lifestyles have evolved around the cyclic nature of the monsoon rains and the growing season. West Africans are heavily reliant on climate-dependent economic activities such as agriculture and herding. For example, in sub-Saharan Africa, 65% of the labor force (Tarhule et al. 2009; FOA 2006) and 95% of land use are devoted to agriculture production (Rockstrom et al. 2004). The lack of irrigation infrastructure in West Africa implies an overwhelming dependence on rain-fed agriculture, thus leaving the ~317 million people living in West Africa today (Figure 1.2) highly vulnerable to variability in monsoon rainfall (Baron et al., 2005).

The West African monsoon exhibits significant year-to-year variations in the timing of the onset of the rainy season as well as in total rainfall accumulation in an individual year. The monsoon also experiences distinct active and break cycles throughout the rainy season. Thus, seasonal forecasts regarding the timing and intensity of the active monsoon cycles can be critically important for determining when to plant crops, what crops to plant, and how to manage water resources throughout each year (Ndomba, 2010). Unfortunately, based on the current state of the science, seasonal and weather forecasts for West Africa are unreliable (Wang, 2008; Tompkins and Feudale, 2010). Also, there is little-to-no infrastructure to disseminate this information from the scientific level down to individual farmers (Boko et al., 2007). This leaves the people of West Africa unprotected from and unprepared for wet season precipitation variability.

Over the past 40 years, sub-Saharan Africa has also been in the throes of a severe drought which has compounded the impacts of the interannual and intraseasonal variability in monsoon rainfall (Nicholson, 2000; Figure 1.3). This drought has had devastating agricultural, economic and societal consequences for the region and has made many of us aware of the overall vulnerability of people living in West Africa.

In addition to climatic conditions, such as droughts, floods and heat waves, a number of socio-economic issues unrelated to climate also influence the overall vulnerability of communities in this region. Studies have attempted to assess the overall vulnerability of Africa by examining the complex web of interacting factors that cause stress to societies (e.g., Joiner et al., 2012). Figures 1.4 and 1.5 both highlight important aspects of life in West Africa that make people increasingly vulnerable. These figures not only include climate and weather related

hazards (Figure 1.4b, Figure 1.5b) but also access to food, clean water and health care (Figure 1.4a, Figure 1.5c); exposure to disease epidemics (Figure 1.5c,d, Figure 1.5c); population density (Figure 1.5d); and the ability of governments to help communities in times of need (Figure 1.5e). Given the high level of vulnerability people in West Africa face, it is argued that human induced climate change will only exacerbate the already poor conditions in the region. The question plaguing scientists today is how extreme will the changes in the climate over West Africa be during the next 50-100 years?

Based on the findings from Working Group I of Fourth Assessment Report of the Intergovernmental Panel on Climate Change (IPCC, 2007), the current answer to this question is, we don't know. Figure 1.6 shows the multi-model ensemble prediction for the changes in rainfall that can be expected to occur in the next 100 years. Cool colors in this figure show regions where rainfall is expect to increase in a warming climate and warm colors are regions where rainfall totals are expected to decrease. In contrast, white areas are regions where less than 66% of the models are in agreement about the sign of the expected change in rainfall. In other words, white areas on this figure highlights regions where there is considerable uncertainty among the IPCC AR4 models about future changes in precipitation. While there is relative agreement among the models that decreases in rainfall can be expected over the already dry Sahara in North Africa in both the winter (DJF) and summer (JJA), over much of West Africa, there is no consensus among the models about the expected change in rainfall in a warming climate. This indicates that the models not only disagree about how large the expected change in rainfall will be over the next century, but they also disagree about the sign of the change. Deeper investigation into model differences show that about half of the models show small increases in

precipitation over West Africa while the other half indicate that precipitation will decrease over West Africa in the next Century (Cook, 2008).

There are a number of reasons why coupled general circulation models (CGCMs) used to make climate change projections exhibit a broad range of solutions for potential changes to the monsoon over West Africa. These models typically have different horizontal and vertical resolutions, they use different parameterizations to represent sub-gridscale processes such as clouds and boundary layer turbulence, and they represent ocean physics and land-surface processes using different techniques which will influence the coupling between the atmosphere, ocean and land surface. The WAM is a complicated system which involves many interactions between the atmosphere, ocean and land surface. The WAM is also influenced by processes that occur over a range of temporal and spatial scales, from propagating mesoscale convective systems to the planetary scale circulation that drives the monsoon winds (Hall and Peyrille, 2006). The inter-model differences in how the complex features of the WAM are represented is ultimately what causes the overall uncertainty in climate change projections over this region.

Further investigation into the simulation of the West African monsoon in CGCMs shows that many models are unable to accurately represent the timing, spatial patterns and magnitude of monsoon precipitation over West Africa (Cook and Visy, 2006). Traditional CGCMs have difficulty capturing the monsoon because they are unable to represent the complex, multi-scale interactions known to be associated with the monsoon (Yang and Slingo, 2001). One major limitation of traditional models is that they must parameterize sub-gridscale processes and are therefore unable to capture the important feedbacks that occur between small scale convection

and the large-scale dynamics. It is possible that an improved representation of sub-gridscale physics may increase the fidelity of climate simulations of the West African monsoon.

In this study, I examine how the inclusion of the multi-scale modeling framework (MMF) in a standard CGCM modifies and potentially improves the representation of the West African monsoon. The MMF is an innovative computational strategy that investigates the interactions between clouds and global circulation of the atmosphere. MMFs have been uniquely designed to examine multi-scale interactions between small-scale circulations and large-scale dynamics. While traditional GCMs must parameterize small-scale physical features such as dry and moist convective processes, in MMFs, embedded within each GCM grid cell is a two-dimensional cloud resolving model (CRM) which allows for explicit simulation of small-scale cloud and boundary-layer processes (Randall et al. 2003). This approach of embedding CRMs within a GCM is sometimes referred to as "superparameterization."

Throughout the remainder of this dissertation I examine the simulation of the West African monsoon in two CGCMS. The first is the standard Community Climate System Model (CCSM) and the second is the superparameterized-CCSM (SP-CCSM). This study has two main goals, the first is to use the SP-CCSM to gain important understanding of the West African monsoon focusing on the seasonal, synoptic and intraseasonal variability of precipitation over the region. The second goal is to identify the strengths and weakness of the improved model in the simulation of the WAM which may help to guide future improvements in the MMF.

The remainder of this dissertation is outlined as follows. Chapter 2 describes the observational datasets and model simulations used in this dissertation. In Chapter 3 the seasonal evolution of key features of the West African monsoon are analyzed. This chapter includes an

examination of the seasonal cycle of precipitation, low-level winds, sea surface temperatures, the African easterly jet, the Saharan heat low, meridional gradients of temperature and moisture as well as African Easterly Waves (AEWs). The relationship between convection and AEWs is extensively studied in Chapter 4. In this chapter I use statistical diagnostics of convection to compare the horizontal and vertical structure of AEWs from the models with observations. I then examine the energy characteristics of the waves to try to understand the generation, development and propagation of these waves. In Chapter 5 the intraseasonal variability of precipitation is examined in both observations and the SP-CCSM. Here I look at the relationship between other tropical climate features such as the Madden Julian Oscillation and the Indian monsoon and the West African Monsoon. Finally in Chapter 6 I end with some overall conclusions and discussion of future work.

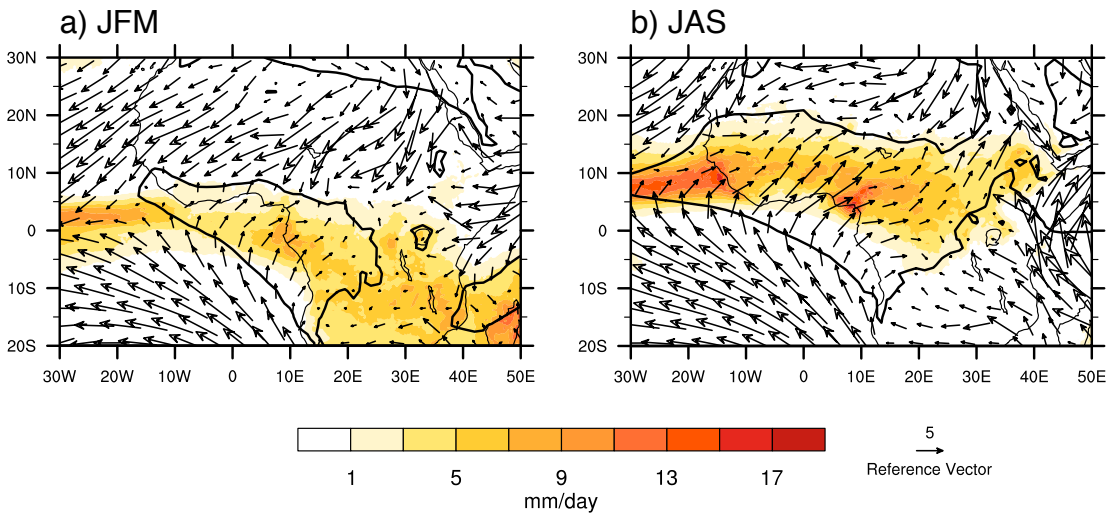


Figure 1.1 Seasonal distribution of rainfall and low-level winds from boreal winter (JFM, left) and summer (JAS, right). Data are from the ERA-I reanalysis and TRMM precipitation.

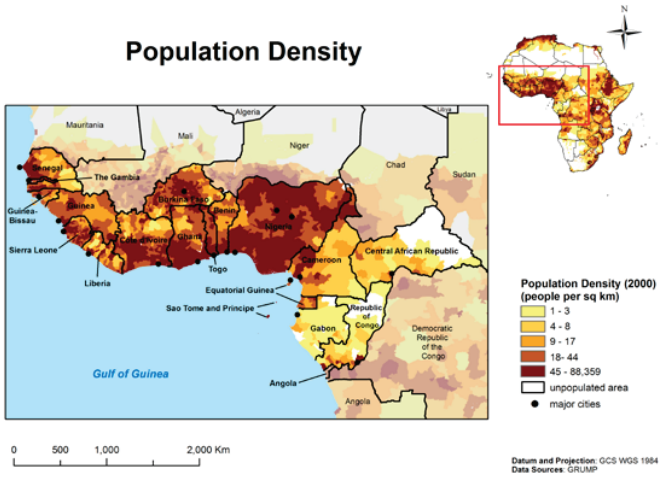


Figure 1.2 Population density of West Africa. Source: Joiner et al. (2012) Appendix H. Vulnerability to Climate Change in West Africa: Adaptive Capacity in the Regional Context. Student Working Paper No. 4 from Climate Change and African Political Stability program.

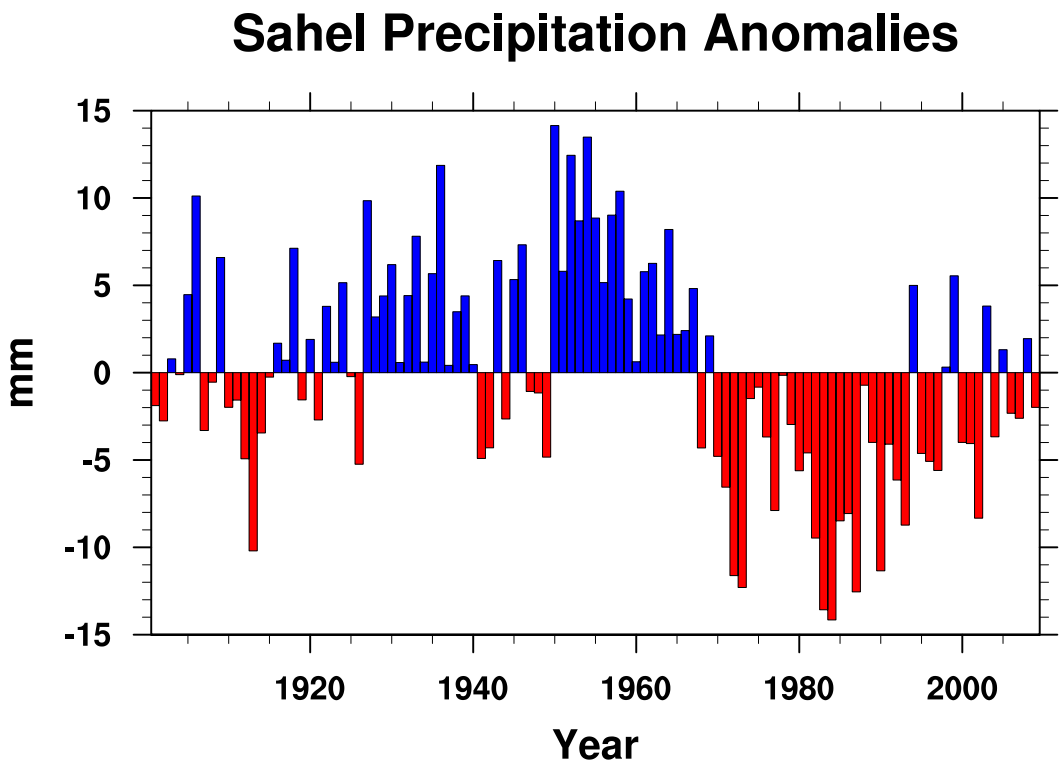
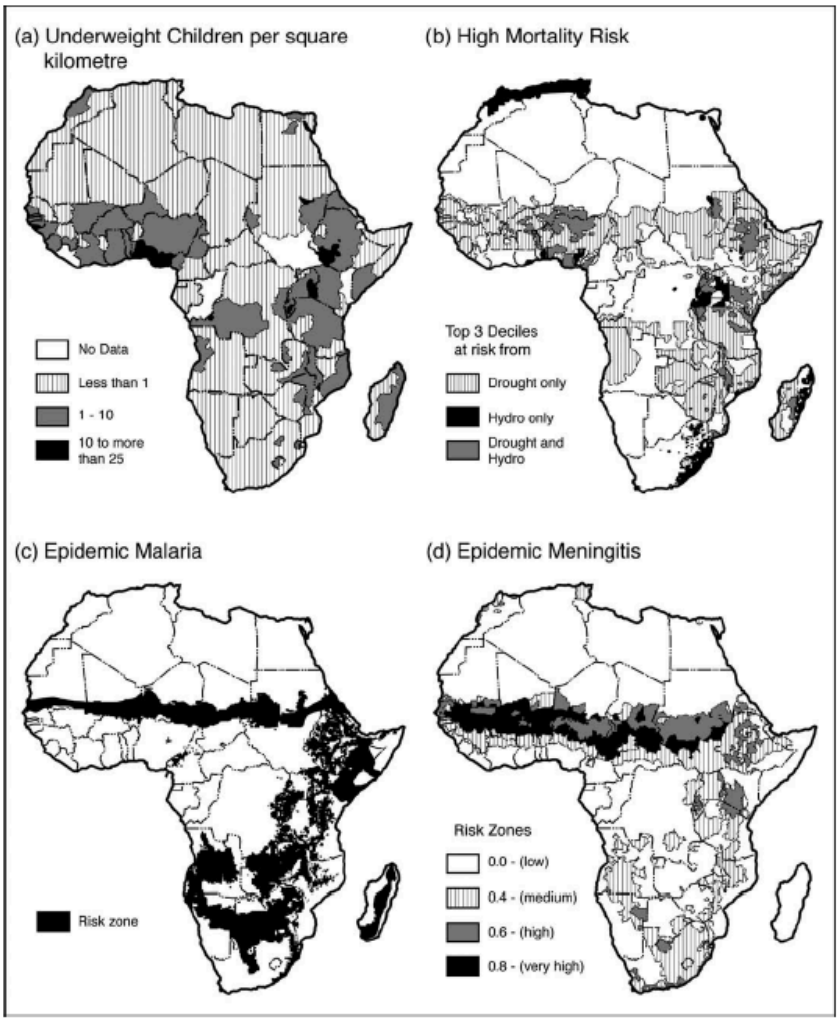


Figure 1.3 Longterm rainfall fluctuations over the Sahel region of West Africa from the CRU TS3.1 gauge based rainfall dataset. Anomalies are based on the 1901-2010 average.



\

Figure 1. 4 Examples of current risk areas for Africa based on a) Hunger, b) natural disaster related risks c) regions prone to malaria outbreaks, d) regions prone to meningitis outbreaks. Source: Boko et al. (2007), Figure 9.1.

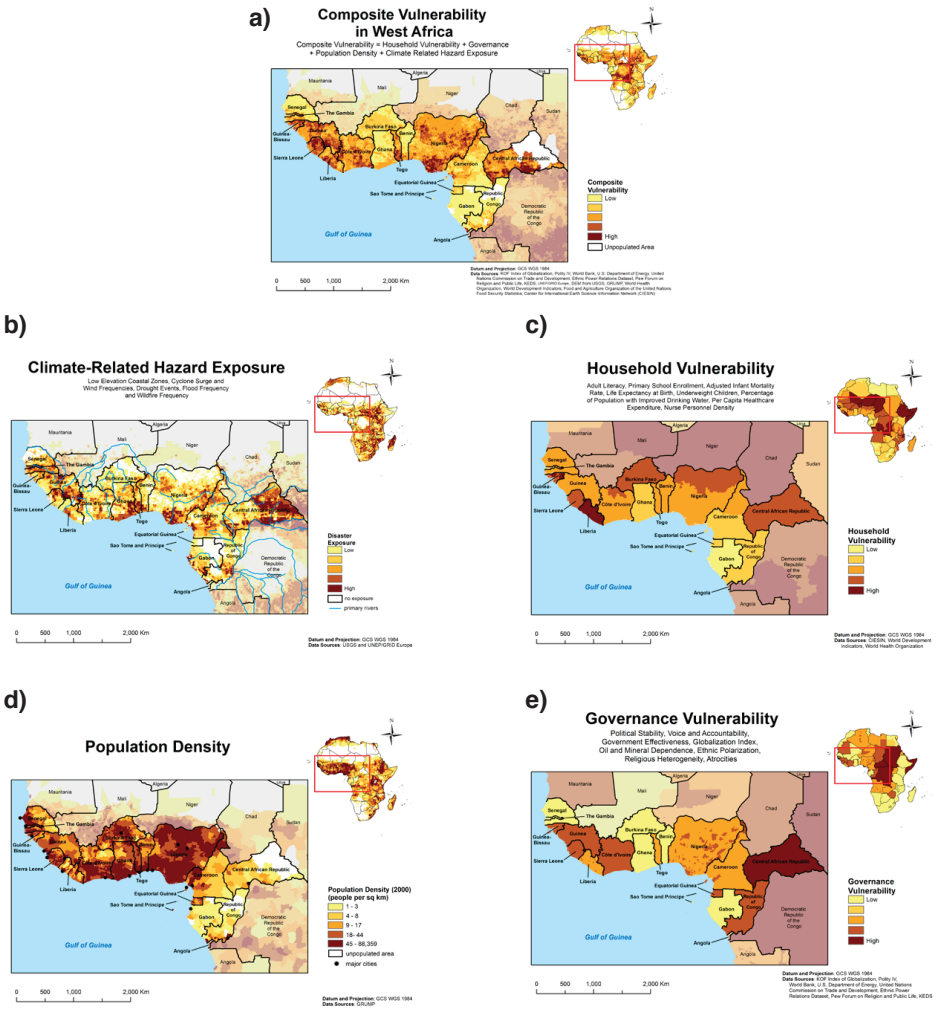


Figure 1.5 Estimated composite vulnerability based on the influence of climate related hazard exposure (b), household vulnerability (c), population density (d) and Governance (e). Source: Joiner et al. (2012). From the top Figure 6, Appendix G, Appendix F, Appendix H, and Figure 5. Vulnerability to Climate Change in WEst AFrica: Adaptive Capacity in the Regional Context. Student Working Paper No. 4 from Climate Change and African Political Stability program.

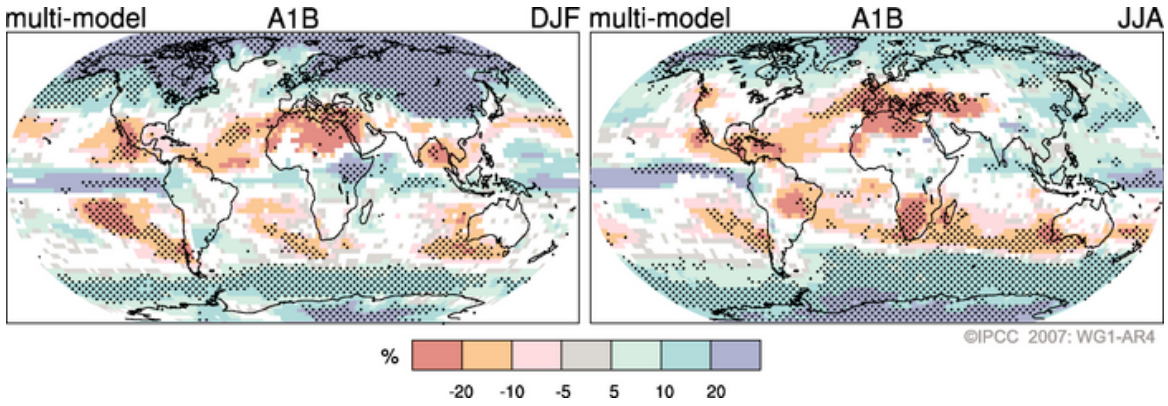


Figure 1.6. Relative changes in precipitation (in percent) for the period 2090-2099, relative to 1980-1999. Values are multi-model averages based on the SRES A1B scenario for December to February (left) and June to August (right). White ares are where less than 66% of the models agree in the sign of the change and stippled areas are where more than 90% of the models agree in the sign of the change. Source: IPCC (2007) Figure 10.9.

CHAPTER 2

MODELS AND OBSERVATIONS

2.1. MODEL SIMULATIONS

In this study I analyze simulations of the West African monsoon from two coupled general circulation models (CGCMs). The first is the standard Community Climate System model, version 3 (CCSM, Collins et al., 2006), which uses conventional cumulus parameterizations to represent cloud-scale processes. The second is the state-of-the-art Super-parameterized-CCSM (SP-CCSM; Stan et al., 2010) in which the traditional parameterizations have been replaced by embedding a two-dimensional (2D) cloud system resolving model (CRM) into each atmospheric grid column.

Both models were run using T42 resolution (2.8º x 2.8º grid) for the atmosphere with a semi-Lagrangian dynamical core. The standard CCSM was run with 26 vertical levels, where as the SP-CCSM was run with 30 levels. The CRMs embedded within SP-CCSM have 32 columns oriented in the north-south direction, a horizontal resolution of 4km, and 28 levels that are collocated with the lowest levels of the large-scale model. In both simulations, the atmospheric model is coupled to the low-resolution 3º version of the Parallel Ocean Program (POP) ocean model (Smith and Gent, 2002) and the community land surface model version 3 (CLM3; Bonan et al., 2002) version 3. Both simulations are 25 years in length, with daily mean output.

In the standard model, deep convection is parameterized using Zhang and McFarlane (1995), shallow convection is represented using Hack (1994) and stratiform clouds are

parameterized following Sundqvist (1988). In the SP-CCSM the 2D CRMs replace the conventional parameterizations of moist physics, convection, turbulence, and boundary layer processes. Cloud microphysics and radiation are still parameterized, but are applied now on the CRM scale. The momentum transport associated with the 2D CRM is unrealistic, so momentum feed back from the CRM to the large scale is prohibited (Khairoutdinov et al., 2005). The CRMs are forced by the large-scale advection of heat, moisture and momentum. The GCM, in turn, is modified by domain averaged CRM tendencies of temperature, water vapor and non-precipitating liquid water. The CRMs embedded within each gridbox have periodic boundary conditions, so information is not translated across the large-scale at the CRM scale. More detailed information about the embedded CRM and coupling between the GCM and the CRM please see Khairoutdinov and Randall (2001, 2003) and Khairoutdinov et al. (2005).

As with traditional parameterizations the CRM results are assumed to be representative of the cloud processes that occur in the entire grid column, and not an exact representation of specific clouds. Essentially both the embedded CRM and the traditional parameterizations have the same "job": to estimate the characteristics that clouds would have based on the large-scale conditions in the gridbox. The difference here is that the CRM can explicitly represent some of the sub-gridscale features.

When compared to the standard CCSM, the SP-CCSM has been shown to improve a number of important features from the climate system. As shown in Stan et al. (2010) the SP-CCSM improves the representation of global mean precipitation patterns, the structure of the equatorial cold tongue and the associated double intertropical convergence zone (ITCZ), the periodicity and amplitude of the El Nino-Southern Oscillation (ENSO), the Asian monsoon, and

the MJO. In general, the most notable improvement of the superparameterization in both coupled and uncoupled simulations is the increase in tropical variability including convectively coupled waves (e.g. Benedict and Randall, 2009 or Thayer-Calder and Randall, 2009). DeMott et al. (2011) further demonstrated that SP-CCSM simulates the eastward-, westward-, and northward-propagating components of the Asian summer monsoon, features that are often misrepresented by coupled and uncoupled GCMs.

In the remainder of this dissertation I will show that the SP-CCSM improves the representation of the West African monsoon when compared to the standard CCSM, including the mean climatology, synoptic and intraseasonal variability.

2.2. ADDITIONAL SIMULATIONS

I also examine the influence that observed SST forcing has on the simulation of the West African monsoon. I do this by showing results from an atmosphere only simulation using the superparameterized Community Atmosphere Model (SP-CAM; Khairoutdinov et al., 2005). The configuration of this model is the same as for the SP-CCSM, only the atmosphere is forced by the 1986-2003 observed monthly-mean SSTs which have been interpolated to daily mean values.

In this study, the superparameterization has been embedded in an older version of CCSM. People often ask how the mean distribution of precipitation compares with more up-to-date coupled climate models. To do this I briefly look at the simulation of the West African monsoon and its relationship to SSTs in 18 of the climate simulations that were submitted to the Coupled Model Intercomparison Project Phase 5 (CMIP5; Taylor et al., 2012) data archive. The models used in this study can be found in Table 2.1. This table includes the model name, modeling center and the resolution of both the atmosphere and ocean components of the coupled models.

The model output is from the 20th Century historical experiment from the CMIP5 archive. All simulations were at least 20 years in length covering the end of the 20th Century and the beginning of the 21st Century. The specific models were chosen because they provided daily mean output from both the atmosphere and ocean. Determining the resolution of the ocean models was not a trivial task, so I include the number of lat/lon gridpoints from each ocean model, and when available any other information I could find about the model grid.

Table 2.1 Table of coupled models used in this study from the CMIP5 data archive.

Model Name	**Modeling Center/Group**	**Atmosphere Resolution # Grid points Resolution**	**Ocean Resolution # Grid points Resolution**
BCC-CSM1.1	Beijing Climate Center, China Meteorological Administration	64×128 T42L26	232×360 tripolar, 1 lon x (1-1/3) lat, L40
BNU-ESM	College of Global Change and Earth System Science, Beijing Normal University	64×128	200×360
CanESM2	Canadian Centre for Climate Modelling and Analysis	64×128 T63L35	256×192L40
CMCC-CM	Centro Euro-Mediterraneo per I Cambiamenti Climatici	240x480	149×182
CNRM-CM5	Centre National de Recherches Meteorologiques / Centre Europeen de Recherche et Formation Avancees en Calcul Scientifique	128×256 TL127L31	292×362
CSIRO-Mk3.6.0	Commonwealth Scientific and Industrial Research Organization in collaboration with Queensland Climate Change Centre of Excellence	96×192 T63 spectral, 1.875 degrees EW x approx. 1.875 degrees NS, 18 levels	1.875 degrees EW × approx. 0.9375 degrees NS, 31 levels

Model Name	Modeling Center/Group	Atmosphere Resolution # Grid points Resolution	Ocean Resolution # Grid points Resolution
GFDL-ESM2G	NOAA Geofluid Dynamics Laboratory	90×144	210×360 tripolar grid
GFDL-CM3	NOAA Geofluid Dynamics Laboratory	90×144 C48L48	Tripolar360×200L50
HadGEM2-CC	Met Office Hadley Centre	145×192 N96L60	216×360 lat: 1.0-0.3 lon: 1.0 L40
FGOALS-s2	LASG, Institute of Atmospheric Physics, Chinese Academy	108×128	196×360
INM-CM4	Institute for Numerical Mathematics	120×180	340×360
IPSL-CM5A-LR	Institute Pierre-Simone Laplace	96×96	149×182
IPSL-CM5A-MR	Institute Pierre-Simone Laplace	143×144	149×182
MIROC4h	Atmosphere and Ocean Research Institute (The university of Tokyo), National Institute for Environmental Studies, and Japan Agency for Marine-Earth Science and Technology	320×640 T213L56	rotated pole 1280×912 L48
MIROC5	Atmosphere and Ocean Research Institute (The university of Tokyo), National Institute for Environmental Studies, and Japan Agency for Marine-Earth Science and Technology	128×256 T85L40	256×224 L50
MPI-ESM-LR	Max Planck Institute for Meterology	96×192 T63L47	220×256
MRI-CGCM3	Meterological Research Institude	160×320 TL159L48	1×0.5L51
NorESM1-M	Norwegian Climate Centre	96×144 1.9ºx2.5º f19L26	384x320 gx1v6L53

2.3 OBSERVATIONAL DATASETS

Several observational and reanalysis datasets are used to evaluate the simulated West African Monsoon. Model simulated precipitation is compared against rainfall from the Tropical Rainfall Measure Mission (TRMM) 3B32 precipitation data. The years 1998-2010 are used in

this study and the TRMM 3B42 dataset covers the tropics between 40ºS-40ºN at 0.25ºlat/lon resolution, and three times daily data (Huffman et al., 2007). To compare with the models, the TRMM data product was averaged to daily means and used to create the monthly climatologies and examine the intraseasonal variability of West African precipitation.

The Climate Research Unit (CRU) time-series precipitation data set version 3.1 (CRU TS 3.1) is also used to examine the seasonal cycle of precipitation over West Africa. This is a monthly mean land-surface only precipitation data product interpolated from rain gauge estimates that extends from 1901-2009 (Mitchell and Jones, 2005).

The simulated OLR from each model is compared against the daily mean NOAA interpolated OLR dataset (Liebmann, 1996). The NOAA OLR dataset has a resolution of 2.5ºx2.5º and extends from 1979-2010. While there are OLR products with higher space and time resolutions, the NOAA OLR dataset is comparable to the output available from the models and has a long 32 year record which increases our confidence in the results presented here.

Climatological SST patterns in the Atlantic are compared against the NOAA Optimal Interpolation Sea Surface Temperature High Resolution Dataset (version 2) (Reynolds et al. 2007). This dataset provides daily mean SSTs for the period 1981-2010 and has a resolution 0.25ºlat/lon. These SSTs were retrieved from the Advanced Very High Resolution Radiometer (AVHRR) infrared satellite SST data.

All other meteorological fields such as winds, streamfunction, vertical velocity, temperature and humidity are from European Centre for Medium-Range Weather Forecasts (ECMWF) Interim reanalysis product (ERA-I; Dee et al., 2011). The ERA-I data product was retrieved with 4 times daily output on a 1.5º grid. The data have been averaged to daily mean

values to compare with the model output. The lack of consistent and spatially coherent observational soundings over West Africa does impose a challenge, here reanalysis products such as ERA-I are necessary for long-term studies such as this one. As with all reanalysis products, variables such as specific humidity are strongly influenced by the model physics and so should be considered a good estimates of humidity, but not direct observations.

Table 2.2 summarizes the information described here for the model simulations and observational datasets.

Table 2.2 List of models and observational data sets used in this study. Table contains information about the horizontal, vertical and temporal resolution of each data set.

Dataset	Origin/ platform	Horizontal Resolution	Temporal Resolution	Vertical levels	Selected Variables
CCSM	Model	T42 2.8º×2.8º	Daily mean 25 years	26 - interpolated to standard pressure levels	Precipitation, winds, SSTs, specific humidity, temperature
SP-CCSM	Model	T42 2.8º×2.8º	Daily mean 25 years	30 - interpolated to standard pressure levels	Precipitation, winds, SSTs, specific humidity, temperature
SP-CAM	Model	T42 2.8º×2.8º	Daily mean from 1986-2003	26 - interpolated to standard pressure levels	Precipitation, winds, SSTs
TRMM	Satellite and rain guage	0.25º×0.25º	3 hourly 1998-2010	Surface	Precipitation
NOAA OLR	Satellite	2.5º×2.5º	Daily mean from 1979-2010	Top of Atmosphere	OLR
SST	Satellite	0.25º×0.25º	Daily mean from 1981-2010	Surface	SST
ERA-I	Radiosonde, Satellite, model forecast	1.5º×1.5º	4 times daily from 1979-2010	25- 1000-100 hPa	winds, specific humidity, temperature, geopotential height

CHAPTER 3

THE SEASONAL CYCLE OF THE MONSOON

3.1. INTRODUCTION

The West African Monsoon (WAM) is a complex system that involves coupled interactions between the ocean, atmosphere and land surface. The processes that couple the different components of the WAM system occur on multiple time and spatial scales. The key features of the WAM are highlighted in the schematics found in Figure 3.1. These schematics are a good visual representation of the dynamical features of the monsoon which will be explored in this chapter.

Prominent in Figure 3.1a is the inter-tropical convergence zone (ITCZ) which represents the north-south migration of the primary rain band near Africa. The ITCZ is positioned over the equatorial Atlantic during the winter to over the continent in summer. In the broadest sense the WAM is the large-scale response to differential heating of the hot African continent and the relatively cool Atlantic ocean during summer. The development of the Atlantic cold tongue along the equator helps to strengthen the thermal contrast between the ocean and land surface further driving the monsoon (Figure 3.1a, Okumura and Xie, 2004). The thermal contrast between the continent and ocean results in relatively low surface pressures to the north over the Sahara and high pressures over the Atlantic. This pressure gradient drives the southwesterly

monsoon winds at low levels, pushing cool moist air on to the continent and driving convection (Figure 3.1a, blue arrow, monsoon winds).

In the north, the high surface temperatures and low surface pressures result in the Saharan heat low (Figure 3.1a, SHL, red contours). The SHL is a major component of the WAM system and has been found to be important for the monsoon flow, the timing of the monsoon onset and the maintenance of the African easterly jet (AEJ). The hot dry northeasterly winds associated with the SHL, commonly referred to as the Harmattan winds (orange arrow), converge with the southwesterly monsoon flow along the Intertropical discontinuity (Figure 3.1a, ITD, dashed line). Much like the ITCZ, the ITD migrates north/south throughout the annual cycle and is always positioned to the north of the ITCZ itself.

The large temperature and moisture gradients along this discontinuity between the two air masses results in the development of the AEJ (Figure 3.1a, black arrow). The AEJ is a mid-level jet centered at approximately 600 hPa it exhibits large horizontal and vertical wind shears and has been found to be both baroclinicly and barotropicly unstable. The instabilities associated with the AEJ are important for the maintenance and propagation of African easterly waves (Figure 3.1b, AEWs, black waves). AEWs are synoptic weather systems and are the dominant source of variability over West Africa during the monsoon. These waves mix the hot-dry air over the Sahara desert with the cool moist air over the Gulf of Guinea, helping to reduce the large temperature and moisture gradients found over the region. AEWs are also important for organizing precipitation over the continent and strongly influence the total amount of precipitation that falls during the monsoon season over the Sahel (Mathon et al., 2002; Fink and Reiner, 2003; Kiladis et al., 2006; Mekonnen et al., 2006). As will be discussed further in

Chapter 4, AEWs are thought to be coupled to convection where convection has been found to be important for the generation and maintenance of the waves, but the waves themselves help to excite convection. AEWs are also act as seed disturbances for the generation of tropical cyclones in the Atlantic (Figure 3.1b)

As discussed in the introduction chapter of this dissertation, general circulation models (GCMs) and models used for numerical weather prediction (NWP) currently have difficulty representing the WAM system. These models are notoriously unreliable in their seasonal and weather predictions of African rainfall. It has long been argued that many of the problems GCMs and NWP models have in prediction the WAM are due to a misrepresentation of the mean annual cycle and their inability to simulate the complex dynamical systems described above.

As a first step toward examining the WAM in the SP-CCSM, I evaluate the simulation of the seasonal cycle of the WAM, focusing on the dynamical elements mentioned above. In the next section a brief description of the observational datasets used in this chapter are described. This is followed by a comparison of the simulated and observed WAM. The main emphasis in this chapter is on the simulation of the seasonal cycle of precipitation and the low-level winds (Section 3), the seasonal evolution of the SHL (Section 4), the simulation of the summer AEJ (Section 5), and a brief examination of AEW activity (Section 6).

3.2. MODELS AND OBSERVATIONS

For a complete description of the models and observational datasets please see chapter 2 of this dissertation. Briefly, the primary focus of this chapter is on a comparison of the seasonal cycle of the simulated monsoon from SP-CCSM and CCSM with observations. I also include a short description of the summer climatology in SP-CAM, in which the atmospheric component

of the SP-CCCSM is forced with observed SSTs. The summer monsoon is also examined in some of the models that were submitted to the CMIP5 archive.

Several observational and reanalysis datasets are used to evaluate the simulated West African Monsoon. Dynamical fields such as the winds and geopotential height are obtained from the European Centre for Medium-Range Weather Forecasts (ECMWF) Interim reanalysis product (ERA-Interim; Dee et al., 2011). The NOAA Optimal Interpolation Sea Surface Temperature High Resolution Dataset (version 2) was used in this study to examine SSTs (Reynolds et al., 2007). The precipitation climatology shown in this study was calculated from the Tropical Rainfall Measure Mission (TRMM) 3B32 daily mean precipitation data 1998-2010 and covers the tropics between 40ºS-40ºN at 0.25ºlat/lon resolution, and three times daily data (Huffman et al., 2007). The TRMM data product was averaged to daily means and used to create the monthly climatologies. The CRU TS 3.1 long-term surface observation based precipitation data set is also used to examine the seasonal cycle of rainfall over West Africa.

3.3. PRECIPITATION AND LOW LEVEL WINDS

3.3.a. Observations

The mean annual cycle of rainfall over West Africa is presented here in two ways, first through spatial maps based on seasonal averages (Figure 3.2) and second through a time-latitude cross-section (Figure 3.3). The spatial maps of observed precipitation in Figure 3.2 are from two data sources, the CRU precipitation data set which is based on surface observations and TRMM which is satellite derived precipitation. In Figure 3.2, the 925hPa wind field from ERA-I is shown over the TRMM precipitation dataset.

Precipitation over West Africa during the boreal summer is influenced by the north-south displacement of the inter-tropical convergence zone (ITCZ), which follows the annual march of the sun. While the typical picture of the West African monsoon (WAM) is thought of as a smooth transition of rainfall from the Gulf of Guinea onto the continent and then a return to the ocean, research over the past 10 years has shown that the progression of the ITCZ is actually characterized by a succession of active phases and pauses in convective activity. The intraseasonal variability in WAM precipitation will be explored further in Chapter 5.

During boreal winter (December-February), when rainfall near West Africa is at its weakest, the primary band of rainfall resides offshore of the Guinea coast just north of the Equator and extends out into the Atlantic ocean (Figure 3.2a,b). During this time period, northeasterly winds from the African deserts push warm dry air to the southern edge of the content. These winds converge with the southeasterly winds associated with the Santa Helena high just off the Guinea coast (Figure 3.2b). In boreal spring (March-June), the ITCZ transitions onto the continent and the WAM begins (Figure 3.2c,d). At this time, the southwesterly low-level monsoon winds extend from across the equator and bring moisture onto the continent that is essential for precipitation (Figure 3.2d). The monsoon winds converge with the dry northerly Harmattan winds just to the north of the 1mm/day precipitation band at the intertropical discontinuity (ITD, thick black line Figure 3.2d). The seasonal evolution of the WAM then undergoes several transitions involving various active phases and pauses (Figure 3.3; e.g. Le Barbe et al., 2002; Sultan and Janicot, 2003). The first is an intensification of rainfall along the Guinean coast during May and June (Figure 3.3). This is typically referred to as the "preonset" phase of the WAM, when the ITD reaches 15ºN and rainfall occurs along the coast (Sultan and

Janicot 2003). This is followed by a sudden northward jump of the ITCZ into the Sahelian region (~12ºN) in late June and July (Figure 3.3, e.g. Sultan and Janicot, 2000). In fall (October-December) rain rates decrease gradually and the ITCZ follows a relatively smooth progression back to its position over the Gulf of Guinea (Figure 3.2g,h).

A number of hypotheses have been developed to describe why the main band of precipitation jumps from 5ºN in April, May and June to 10ºN in July, August and September. Some argue that the deepening of the Saharan Heat Low and the cooling of SSTs in the Atlantic increases the pressure gradient force across the continent, pushing monsoon air further north (Okumura and Xie, 2004; Sultan and Janicot, 2003; Gu and Adler, 2004; Ramel et al., 2006). Others argue that the northward shift of the AEJ and its associated horizontal and vertical wind shears are critical for the monsoon jump (Sultan and Janicot, 2003). Still others show support for the idea that the development of a shallow meridional circulation that influences where the maximum in meridional wind and moisture convergence occurs is important for the sudden shift in precipitation (Hagos and Cook, 2007).

Embedded within the zonally elongated rain band associated with the WAM are three three distinct maxima in precipitation (Figure 3.2 e,f); one over the Ethiopian Highlands, one near the Bight of Bonny near Cameroon, and a third just off the the west coast that extends into the Atlantic Ocean. These maxima are all located near mountainous regions, the Ethiopian Highlands, the Adamawa Highlands of Cameroon, and the Guinea Highlands respectively, and the mountains may be the cause of the localized precipitation maxima. The peak in precipitation near Cameroon is also thought to be influenced by the diurnal forcing of precipitation over the small islands in the Bight of Bony, most notably the island of Bioko (Personal communication

with Matthew Janiga). The maximum off the west coast is thought to be influenced by both the diurnal propagation of convection away from the Guinea Highlands as well as a coastal convergence zone associated with a land-sea breeze circulation (Personal communication with Matthew Janiga).

During the peak monsoon season (JAS) a distinct drying occurs along the Guinea Coast, where rain rates decrease as the primary rain band pushes northward onto the continent. The decrease in precipitation along the coast is thought to be influenced by the rapid development of cool sea surface temperatures (SST) along the equator in what is known as the Atlantic equatorial cold tongue. Figure 3.4 shows the seasonal evolution of SSTs in the Atlantic.

The coupled relationship between SSTs in the Gulf of Guinea and the WAM is complex, and although a few studies have tried to understand the feedback mechanisms between these physical systems, more work still needs to be done. The basic picture, based on the state of the current science, is as follows. The Atlantic equatorial cold tongue develops due to the seasonal evolution of the winds associated with the onset and progression of the WAM (Mitchell and Wallace, 1992; Vizy and Cook, 2001; Caniaux et al., 2011; Nguyen et al., 2011). To a first order, Ekman theory can explain the observed cooling in the equatorial atlantic during Boreal spring and summer. During the cold season in the southern Hemisphere (April - September), the trade winds intensify in the souther hemisphere resulting surface winds that blow northwestward in the southern hemisphere and turn northeastward after crossing the equator due to Coriolis. The surface wind stress on the ocean results in divergence of mixed layer waters and upwelling south of the equator and convergence and upwelling north of the equator. Where upwelling results in a cooling of surface temperatures. This helps also explain why the equatorial atlantic cold tongue

tends to be confined south of the equator itself (Figure 3.4 JAS, Caniaux et al., 2011). Other factors such as vertical mixing due to equatorial ocean currents, as well as the advection of cold water from the southern coastal upwelling region also help give the cold tongue its characteristic shape.

While the development of the Atlantic cold tongue is dependent on the monsoon, cool SSTs in the Atlantic are also critical for the development of the monsoon itself. Cool SSTs in the Atlantic act to suppress convection along the coast and increase convection in the Sahel. Along the coast, cool SSTs result in a reduction of surface fluxes and a stabilization of the atmosphere which acts to suppress convection in the coastal region. Cool SSTs also intensify the cross-equatorial southerly flow in the Gulf of Guinea and help to push the continental rain band inland (Okumura and Xie, 2004).

Forced SST experiments in which the cold tongue was removed from the seasonal cycle show that the southerly monsoon flow is significantly weaker without the development of these cold SSTs (Okumura and Xie, 2004). The weakening of the cross-equatorial southerlies results in increased rainfall along the Guinea Coast and decreased rainfall over the Sahel (Okumura and Xie, 2004). Similar results were found in studies that investigated the interannual variability of monsoon rainfall. In years where the equatorial Atlantic was anomalously warm, precipitation is found to increase along the Guinea coast and decrease over the Sahel (Eltahir and Gong, 1996). The opposite is true for years where the cold tongue is anomalously cool. As will be shown in the next section, the misrepresentation of the Atlantic cold tongue is potentially one of the main regions why GCMs have large errors in WAM precipitation.

3.3.b. SP-CCSM and CCSM

When compared to the standard CCSM, SP-CCSM better represents the magnitude, as well as the spatial patterns associated with West African precipitation (Figure 3.5c, 3.7c). Most notably, the region of maximum precipitation during the peak monsoon season (JAS) is shifted from an incorrect placement over the Gulf of Guinea in CCSM, to over the continent in SP-CCSM. In CCSM the main band of precipitation is much broader and weaker than observed (Figure 3.6). Maximum precipitation rates always occur over the ocean, never on the continent. Throughout all months of the year, CCSM exhibits consistent southward bias in rainfall. The seasonal cycle of rainfall in CCSM appears to expand and contract, rather than displaying a true northward shift onto the continent. In SP-CCSM on the other hand, monsoon rains do display more of a northward shift onto the continent, although the rain band is still too wide, and rainfall never truly stops over the Gulf of Guinea or along the coast (Figure 3.8). The coarse (~3º) resolution of both models may explain why the north-south rainband tends to be too expansive. Rain rates in the SP-CCSM tend to be much larger than observed and rainfall during the peak monsoon period does not penetrate as far northward. While there are clear active phases and pauses in the monsoon rains from SP-CCSM, there is no distinct "jump" in precipitation from the coastal region to the Sahel as is found in observations. This may also be due in part to the coarse resolution of both the model. The SP-CCSM does capture the local maximum in precipitation just off the west coast that extends into the Atlantic as well as the maxima over the Ethiopian Highlands, although precipitation rates are lower than observed in the mountains, most likely due to their coarse representation. Unfortunately SP-CCSM does not capture the maximum in precipitation near Cameroon nor does it capture the dry region that occurs along the Guinea

Coast between the two coastal precipitation maxima. Rain along the coast is consistently greater than observed and may explain why overall the seasonal rainfall totals are greater.

One potential explanation for the excessive rainfall along the Guinea Coast and Gulf of Guinea, is a misrepresentation of the development of the Atlantic Equatorial cold tongue. Both SP-CCSM and CCSM exhibit consistent warm biases in the equatorial Atlantic, although these biases are much larger in CCSM (Figure 3.4). The models both misrepresent air-sea exchanges in the equatorial Atlantic, resulting in increased rainfall south of the observed monsoon during JAS. The misrepresentation of the Atlantic cold tongue is a common problem for coupled GCMs (CGCMs) and is an issue that has not yet been fully diagnosed (Richter et al., 2008). Most likely the combination of the misrepresentation of the low-level trade winds as well as an incorrect response of the mixed layer to surface wind stress are the causes of errors in both the development of the cold tongue as well as the monsoon winds.

Although more detailed experiments need to be performed in order to determine why both models do not simulate the seasonal cooling of SSTs along the equatorial Atlantic, an examination of the low-level wind biases in each model provides interesting insight into the problem. Figure 3.9 shows the difference between the mean zonal winds in ERA-Interim and each model for AMJ and JAS, while the difference in the meridional winds is found in Figure 3.10. Both models have large westerly wind biases over the Atlantic as well as along the coastal region of the continent. The westerly wind biases lead to a weakening of the trade winds which reduces equatorial upwelling in the Atlantic and suppresses the development of the cold tongue. The westerly wind bias is thought to cause the excessive rainfall along the Guinea Coast, and is unfortunately found in many CGCMs (Gates et al., 1999). During spring, at the time of the

monsoon onset, the cross-equatorial southerly flow in both models is weaker than observed, especially along the west coast of Africa near Gabon. These biases in the meridional wind likely reduce the cooling of the Atlantic SSTs by weakening the local upwelling and surface fluxes in this region. A reduction in the southerly winds also indicates that onshore flow near Cameroon will be less, and may explain why there are negative precipitation biases in the models in this region. During the main monsoon season (JAS) CCSM exhibits a reduction of the southerly winds over the continent, which may help explain why the main band of precipitation occurs over the Gulf of Guinea in this model. SP-CCSM on the other hand actually exhibits larger than observed southerly winds in the Gulf, although these positive biases do not extend onto the continent. This combined with the excessive westerly winds and warmer than observed SSTs may help to explain why SP-CCSM has a large positive bias in precipitation along the Guinea Coast.

To further support the claim that warm biases in SSTs in the Gulf of Guinea combined with the misrepresentation of the southwesterly monsoon flow are the causes of the excessive precipitation found along the Guinea Coast in SP-CCSM, we can look at a simulation in which the atmospheric component of the SP-CCSM, the SP-CAM, is forced with observed SSTs. By forcing the atmosphere with the correct development of the Atlantic cold tongue, we see from Figure 3.11 that rainfall along the Guinea Coast in JAS is greatly reduced, and is comparable to observations. Unfortunately in the case of the atmosphere only simulation, the monsoon rains do not penetrate as far northward as is observed. This may be due to an incorrect response of the southerly winds to the large-scale pressure gradient that occurs across West Africa, potentially due to a weaker Saharan Heat Low.

3.3.c. Comparison with CMIP5 models

It is also of interest to see how the SP-CCSM and the CCSM compare to the state-of-the-art climate simulations that were produced for the up and coming Intergovernmental Panel on Climate Change (IPCC) report. Figure 3.12 shows latitude-height cross sections of precipitation averaged between 10ºW and 5ºE, spatial maps of JAS mean precipitation, and the average SST conditions from the same season.

As with the previous generation of CGCMs (Cook and Visy, 2006) the CMIP5 models show a broad range of representations of the West African monsoon. In some models precipitation rates are much lower than observed (BCC-CSM1.1, INM-CM54, FGOALS-s2). In many models the continental precipitation is much more zonally uniform than is found in observations (MIROC4h, MIROC5, GFDL-ESM2G, CanESM2). In most of the models, the northward extent of the monsoon rainfall over Africa is farther south than observed (BCC-CSM1.1, CMCC-CM, INM-CM4, IPSL-CM5AMRI-CGCM3 etc.). None of the models appear to represent the monsoon jump. While many models do show interesting intraseasonal modulations in precipitation, a few have very smooth transitions from the oceanic ITCZ to the continental monsoon (IPS_CM5A-LR)

As with both SP-CCSM and CCSM a number of models have large precipitation biases over the Gulf of Guinea and along the coast (CMCC-CM, CNRM-CM5, GFDL-ESM2G, GFDL-CM3, HadGEM2-CC, MPI-ESM-LR, NorESM1-M). Based on the corresponding SST figures, the argument that positive SST biases in the Gulf of Guinea results in excess precipitation during the summer season seems to hold true, except in the case of GFDL-CM3 where cold SST anomalies do develop during the summer, but perhaps their incorrect placement influences

rainfall near the coast. Several models do exhibit a drying between the west coast and Cameroon, which is similar to observations (BNU-ESM, MRI-CGCm3, IPSL-CM5A-MR, CISRO-Mk3.6.0, GFDL-CM3, HadGEM2-CC) and most of these do show significant cooling in along the equator near West Africa.

To fully understand biases in the SST and precipitation patterns further study would need to be done to investigate the biases in meridional and zonal winds. This was beyond the scope of the current study, but is something I hope to accomplish soon. I would also like to further investigate the relationship between the Atlantic cold tongue and precipitation biases in these models.

3.4. SAHARAN HEAT LOW

The West African Heat Low (WAHL) or what is commonly referred to as the Saharan Heat Low (SHL) due to its placement over the Sahara during summer, is another major dynamical element in the WAM system. The WAHL is critically important for the both low-level circulation in the monsoon as well as the development of the AEJ. The correct development, placement and intensity of the seasonal mean heat low in the models is important for the overall simulation of the WAM.

A heat low is characterized as an area of low surface pressure that results from heating of the lower troposphere and subsequent lifting of the isobaric surfaces resulting in divergence aloft. The WAHL occurs in an area where surface temperatures are high, surface pressures are low, insolation is high and evaporation is low. The WAHL is typically characterized as a zonally elongated heat trough, that is sometimes considered an extension of the planetary-scale thermal trough associated with the Asian monsoon, rather than a circular low (Wu et al., 2009). The

cyclonic circulation associated with the summer heat low acts to increase the southerly monsoon winds along its eastern flank and the northerly Harmattan winds along its western flank. The upward motion associated with the low generates an anticyclonic circulation aloft (near 700hPah) and is thought to help strengthen the AEJ. The WAHL has also been implicated in the dynamics of the observed monsoon jump in June/July (Sultan and Janicot, 2003, Ramel, 2006).

Figure 3.13 shows latitude-height cross sections of geopotential height anomalies and meridional and vertical winds averaged between 20ºW-10ºE from the observations and both models. Figure 3.13a is comparable to Figure 3.2 in Lavaysse et al. (2009). Anomalies of geopotential height are calculated by removing the meridional average geopotential height from each pressure level. This allows us to examine the north-south differences in geopotential height . In both the models and observations, the summer WAHL is characterized by negative geopotential hight anomalies centered at about 18ºN and extending up to 800hPa in the vertical. Anomalies of high geopotential height are found to the south of the heat low, over the Atlantic ocean. Significant uplift occurs within the ITCZ centered just south of 10ºN. The low-level southerly monsoon flow is also apparent from this figure.

To identify the seasonal position of the WAHL, I have used the objective detection methods developed by Lavaysse et al. (2009). This method measures the heat-induced dilation of the lower tropospheric levels to identify the heat low. To do this, first the low-level atmospheric thickness (LLAT) is calculated by determining the difference in geopotential height between 700hPa and 925hPa. The WAHL is the identified as any point with in the domain 0º-40ºN, 20ºW-30ºE, where the LLAT exceeds the 90% threshold of the daily cumulative probability distribution of the LLAT. The method outlined in Lavaysse et al. (2009) uses the

difference in geopotential height at 0600Z, however for this analysis I only had daily mean values for geopotential height. Comparisons of the LLAT and WAHL in ERA-Interim using 0600Z and daily means show qualitatively similar results, so I feel confident using the daily mean values in this study.

Spatial maps of the seasonal evolution of the WAHL from ERA-Interim and the models are shown in Figure 3.14. In these figures the frequency of occurrence of the WAHL for each grid point is plotted. In January the maximum frequency of occurrence of the WAHL is centered over central Africa in the observations and the models. In the observations, the placement of the WAHL is somewhat more variable than the models, so the frequency occurrence is lower. In the spring, the WAHL moves northward and exhibits a zonally elongated structure. In July the heat low moves northwestward and is positioned over the Sahara desert. During this season, the largest differences between the observations and models are found. In ERA-Interim, the SHL is a somewhat circular depression centered just west of the Greenwich meridian. In SP-CCSM and CCSM the heat low maintains a much more zonally elongated structure. This may have important implications for the simulated low-level winds or the AEJ. In October the WAHL moves south again, maintaining a zonally elongated structure.

3.5. AFRICAN EASTERLY JET

The AEJ is also an important component of the WAM system. This summertime jet develops due to the strong temperature and moisture gradients that exist between the cool moist ocean and the hot dry Sahara desert. Model experiments have shown that the meridional gradients of moisture, temperature and vegetation (and its influence on surface albedo) are important for the structure and maintenance of the observed AEJ (Wu et al., 2009). As

demonstrated in Cook (1999) the AEJ is essentially geostrophic, so by the thermal wind relation the positive surface temperature gradient over West Africa induces easterly shear in the winds. The vertical position of the AEJ occurs where the positive meridional temperature gradient reverses in sign to be come negative (approximately 600 hPa). The jet exhibits both barotropic instability (strong horizontal wind shear) and baroclinic instability (vertical wind shear). This instability is important for the growth and propagation of African easterly waves (AEWs) and will be discussed more later in this chapter. Figure 3.15 shows maps of the mean zonal wind speed during JAS at 600 hPa, the meridional cross sections of zonal wind at 0ºE, and zonal cross sections of zonal wind at 15ºN from ERA-Interm and the models. While the position and intensity of the AEJ varies between the different reanalysis products (primarily due to a lack of sounding data over this part of Africa), in ERAi peak winds reach about 12 m/s and are positioned at about 15ºN, 600 hPa and spread from 30ºW to 10ºE. Easterly winds also extend down in the vertical to about 850mb, where they transition to the westerly monsoon winds.

Both of the models do a reasonably good job representing the AEJ, although both models have their own unique biases. In SP-CCSM the AEJ is weaker than observed, with maximum wind speed only reach 10m/s. The AEJ's mean position is slightly higher than observed, at ~550 hPa and its zonal extent is restricted to the continent. In CCSM the jet is stronger than both the observations and SP-CCSM. Peak winds in this model reach up to 14m/s and the zonal extent of the AEJ is much broader than observed, with strong zonal wind speeds extending out to 60ºW over the Atlantic ocean.

To try to understand these differences between the observed and simulated AEJs, we can first look at the meridional cross sections of temperature and specific humidity during JAS.

Meridional gradients of these variables are important for the North-South placement of the jet as well as the vertical position of the jet. Figure 3.16 shows cross sections of temperature and specific humidity across 0ºE. The significant warm temperatures over the Sahara desert are evident in all three figures, with cooler temperatures to the south. The temperature gradients in SP-CCSM appear to be weaker than observed, given that temperatures over the Sahara are lower., hence potential issues with the heat low. The extreme moisture gradient across the continent is also clear from the figures. Specific humidity is much larger over the wester edge of the continent and in the Sahel in regions where rainfall is a maximum in this season and much lower over the Sahara where it is dry. The meridional gradient of specific humidity is also weaker in SP-CCSM, with higher than observed moisture content over the Sahara. Reductions in the meridional moisture gradients will influence the gradients in moist static energy, which are important for the development of the AEJ. The weak temperature and moisture gradients may be due to the excessively strong wave activity found in SP-CCSM, this will be discussed further in the next section and in Chapter 4.

As discussed in the next section, AEWs are known to take energy out of the AEJ through barotropic and baroclinic energy conversion. Differences in observed and simulated AEW activity may also help explain the differences found in the AEJ.

3.6. AFRICAN EASTERLY WAVES

AEWs are synoptic scale disturbances with wavelengths of 2000-6000 km, and periods of 3-6 days. These waves are the dominant mode of atmospheric variability for West Africa during the summer (June - September) and are important for organizing precipitation over this region. While our knowledge and understanding of these waves is ever changing and increasing, current

theory suggests that they are initiated by convective heating in central and eastern Africa (Berry and Thorncroft, 2005; Mekonnen et al., 2006; Hsieh and Cook, 2008) and propagate westward feeding off of the barotropic-baroclinic instability associated with the AEJ (Hall et al., 2006).

Eddy kinetic energy (EKE) is considered a reliable measure of AEW activity over West Africa, and is a good indicator of the location and intensity of AEWs. In this chapter we define EKE as $(1/2)(u'^2 + v'^2)$, where the primes are deviations from a 5-day running average. Figure 3.17 shows the July-September mean EKE fields from ERA-Interim, SP-CCSM and CCSM. In ERA-Interim, AEW activity occurs over West Africa west of 10ºE. Peak AEW activity occurs just off the coast at approximately 12ºN. Much like the AEJ, placement of peak AEW activity differs between the different reanalysis products, but they all show qualitatively similar results.

AEWs are clearly overly active in SP-CCSM and under active in CCSM. While CCSM exhibits little-to no variability in EKE over West Africa, the variability in EKE is much larger in SP-CCSM which compared against the observations. AEW activity in SP-CCSM extends from ~30ºE to 40ºW from 0º-25ºN, with peak activity centered over the region where precipitation is largest.

Given that AEWs are known to take energy out of the AEJ, it is possible that the strong AEW activity in SP-CCSM acts to weaken the AEJ, while the lack of AEW activity in CCSM actually strengthens the jet relative to observations.

Whatever the case, the large difference between the observed and simulated AEW variability needs to be investigated further, and is the subject of the next chapter of this dissertation. Given that AEW activity is known to be important for precipitation variability over

West Africa during the monsoon, the next chapter will also investigate the relationship between convection and AEWs in both models.

3.7 CONCLUSIONS

The addition of the super-parameterization into the CCSM improves the overall representation of the seasonal cycle of the West African monsoon. The mean position of the maximum in precipitation during the summer monsoon is shifted from an incorrect placement over the Gulf of Guinea in CCSM to onto the continent in SP-CCSM. Average precipitation rates are also closer to observations in SP-CCSM. The SP-CCSM is unfortunately not without its own biases. Rainfall rates are still too high over the Gulf of Guinea, and large positive precipitation biases are found along the southern coast in between the Guinea Highlands and Cameroon. Anomalously warm conditions in the Gulf of Guinea and the lack of development of the equatorial Atlantic cold tongue may result in large biases in the simulated zonal and meridional wind fields which cause the precipitation biases found in both models. I also showed that the CMIP5 models exhibit a broad range of solutions for the West African monsoon, with many models having similar biases to those found in SP-CCSM and CCSM. Further investigation will need to be done to try and understand if an improved representation of SSTs in the Gulf of Guinea ultimately results in an improved WAM.

This chapter also showed that including the super-parameterization increases the synoptic variability, in particular AEWs over West Africa. CCSM exhibits almost no variability on AEW time scales (3-6 days), however in SP-CCSM the variability found over Africa is significantly larger than is observed. The characteristics of AEWs will be examined further in the next chapter.

AEWs act to mix vertical and horizontal gradients in temperature and moisture. The overly active wave activity found in SP-CCSM may help to explain why the Saharan heat low, the AEJ and meridional gradients in temperature and moisture are weaker than found in observations.

Based on the results found in this chapter, I am hoping to be able to investigate further the overall influence that SSTs in the Gulf of Guinea have on the model simulated monsoon. I will do this by examining additional simulations with the SP-CCSM where the atmosphere model is forced by the SSTs generated in SP-CCSM. This will allow me to separate the influence of SST forcing and the importance of air-sea interactions

3.8 FIGURES

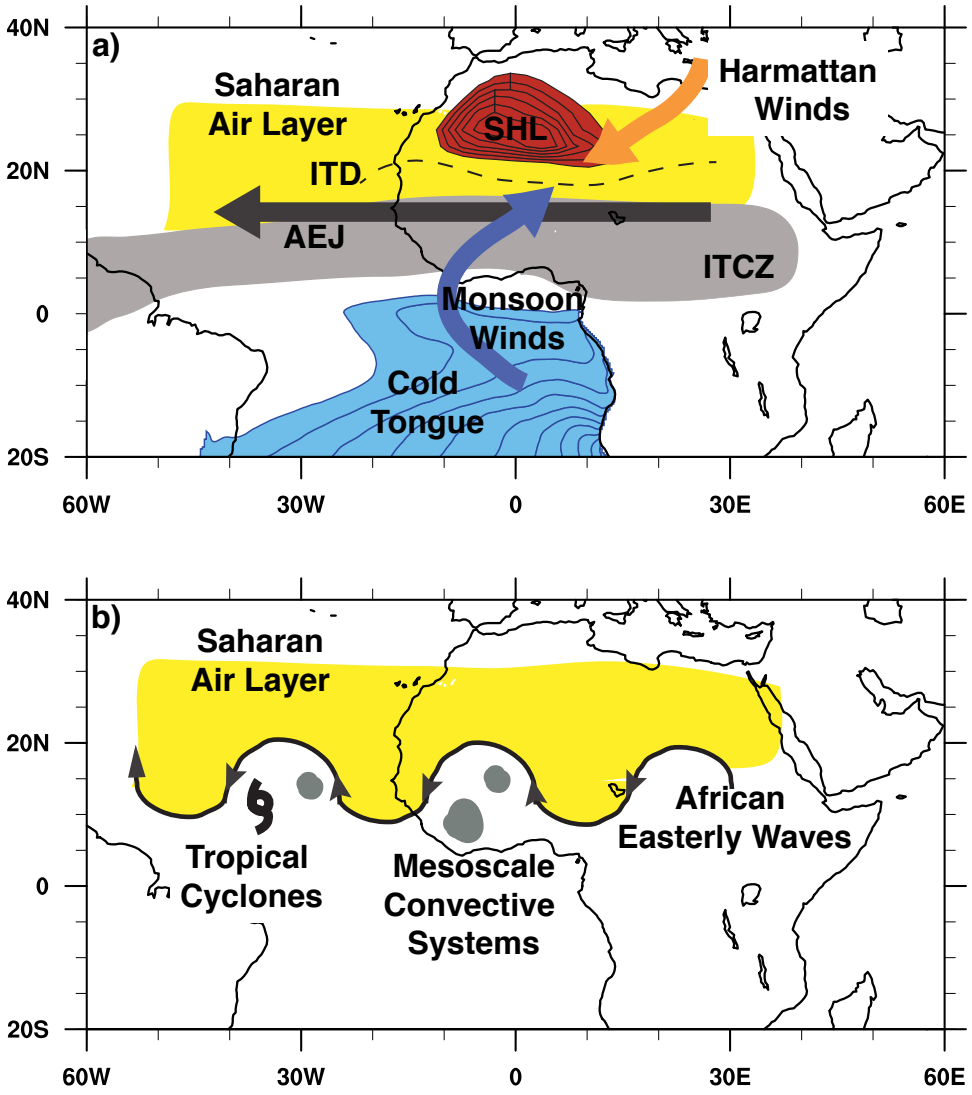


Figure 3.1. Two schematics that represent the different dynamical and physical features important for the West African monsoon. Key features on this diagram include: (a) Saharan air layer, Intertropical discontinuity (ITD), African easterly jet (AEJ), Intertropical convergence zone (ITCZ), Harmattan winds, Monsoon winds, Atlantic cold tongue, (b) Mesoscale convective systems, African easterly waves, and Tropical cyclones.

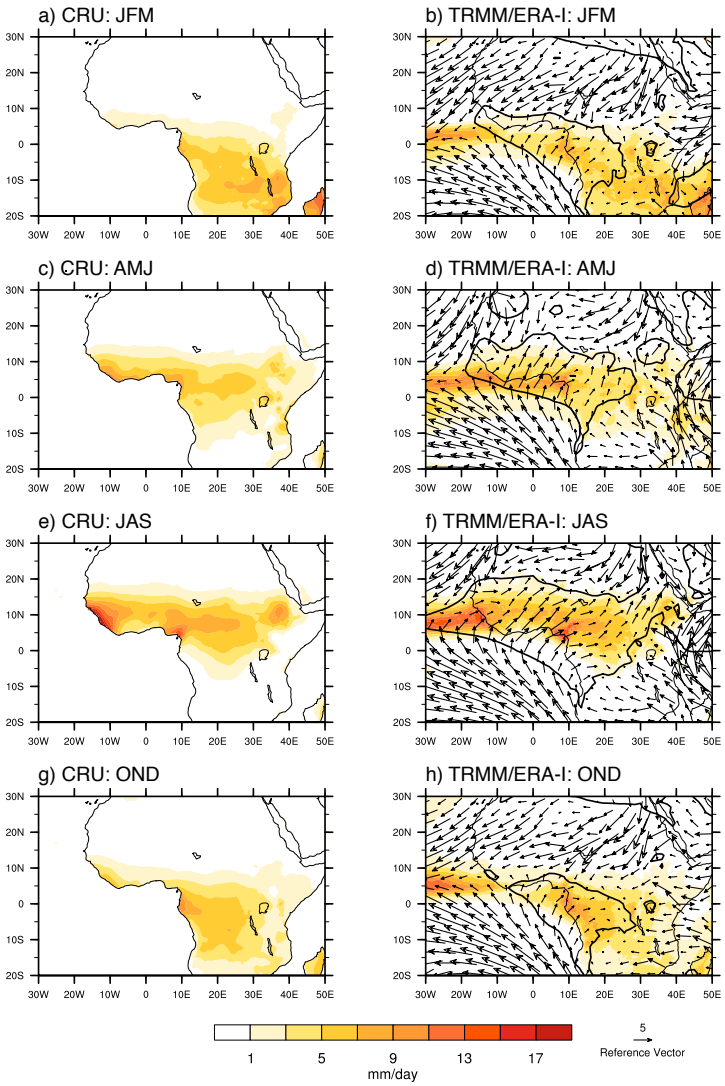


Figure 3.2. Seasonal mean precipitation maps from CRU (left) and TRMM (right) for the months January-March (JFM), April-June (AMJ), July-September (JAS), October-December (OND). 925hPa wind vectors are shown over the TRMM precipitation (right). Also shown is the zero line of the zonal wind (thick black line), which is used here to delineate the intertropical discontinuity. Units for precipitation are in mm day^{-1}.

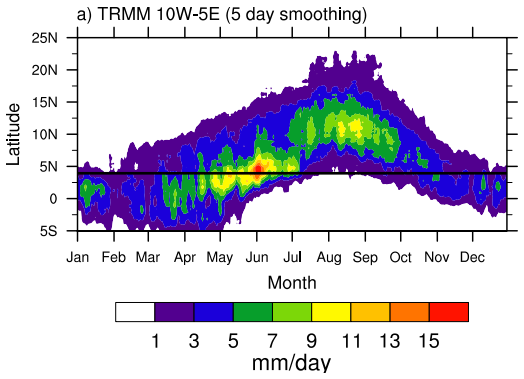


Figure 3.3. Latitude-time cross section of 5-day averaged seasonal cycle of precipitation averaged between 10ºW and 5ºW. The thick black line delineates the southern most edge of the West African continent. Precipitation is in mm day^{-1}.

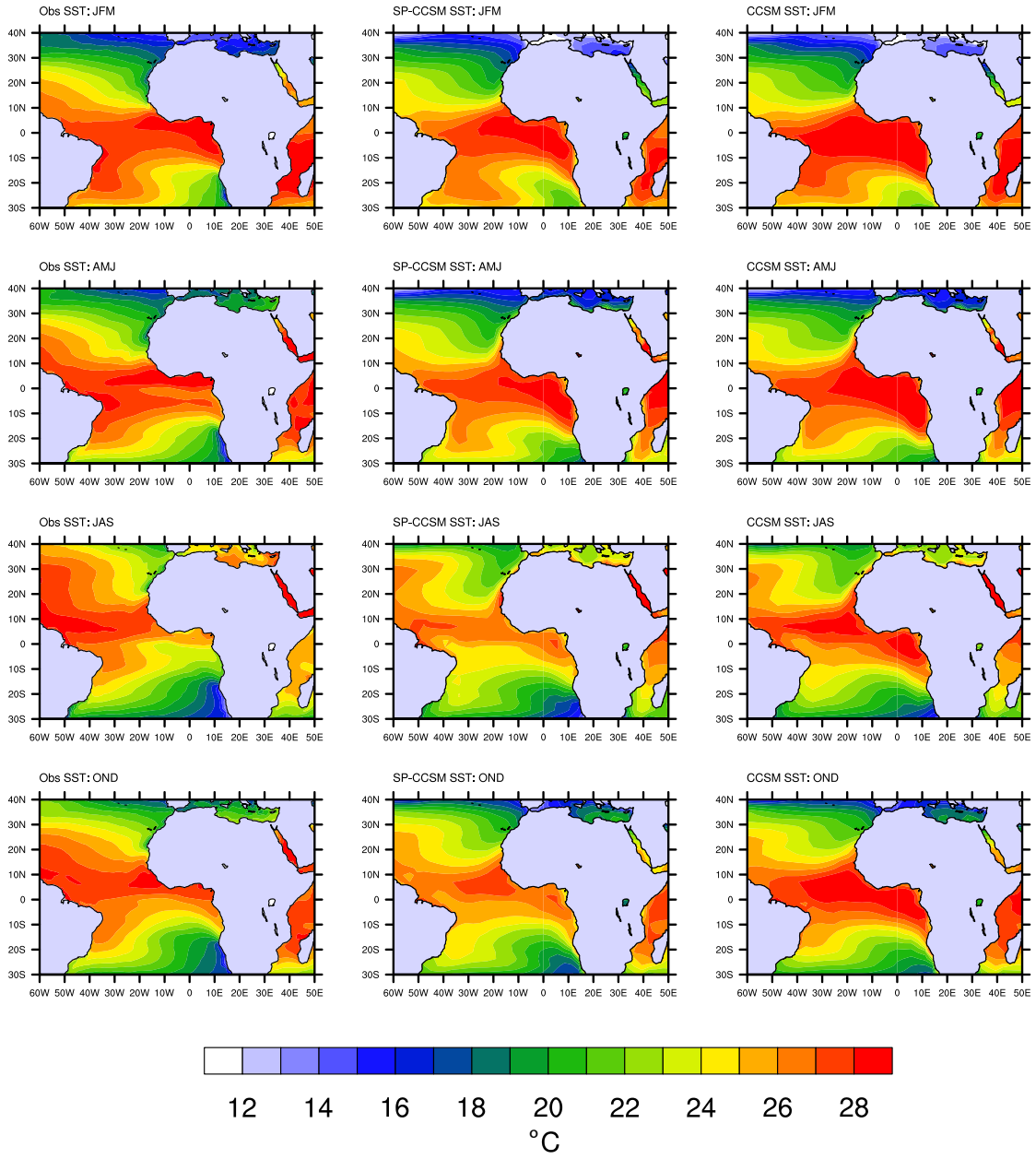


Figure 3.4. A 3-D schematic of the West African monsoon. Features relevant to this chapter are the ITCZ, ITD, AEJ, monsoon winds, SHL. This figure is from Lafore et al. (2010).

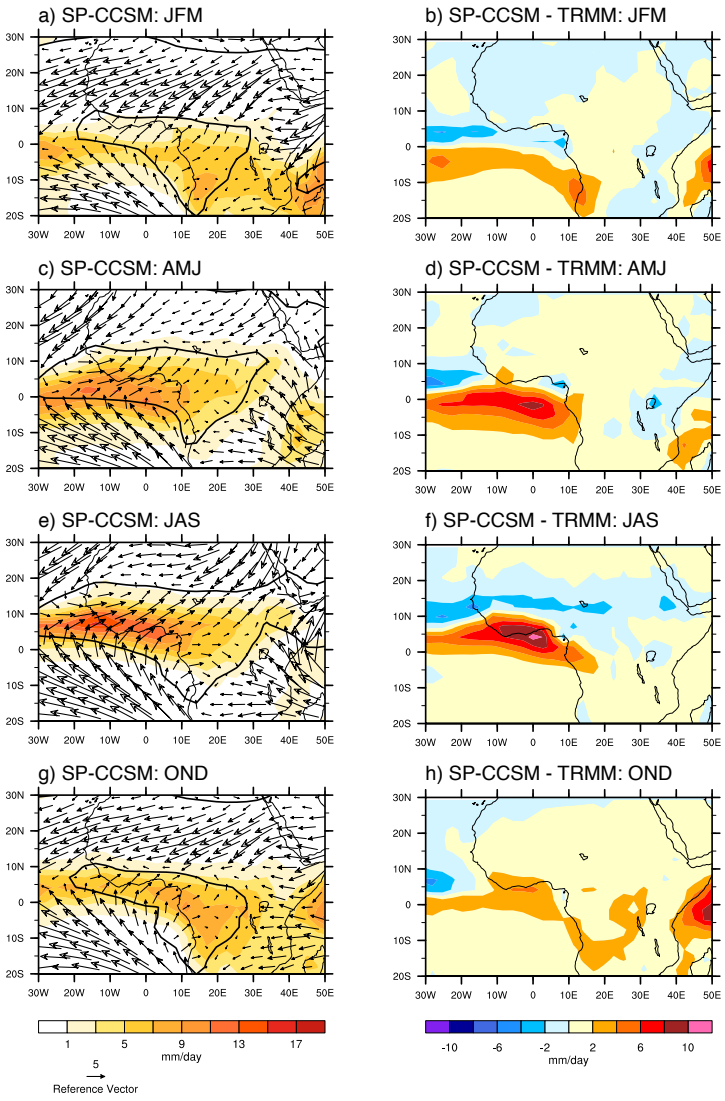


Figure 3.5. Seasonal mean precipitation maps from SP-CCSM (right) with 925hPa winds and the zero line of zonal wind (same as Figure 1). Difference between SP-CCSM and TRMM (left). Units of precipitation are in mm day^{-1}.

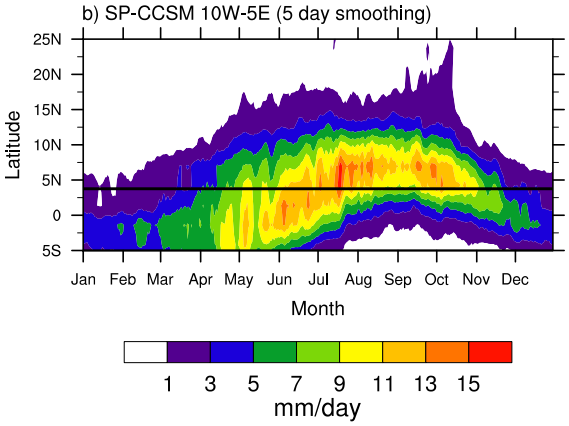


Figure 3.6. Same as Figure 3, except for SP-CCSM.

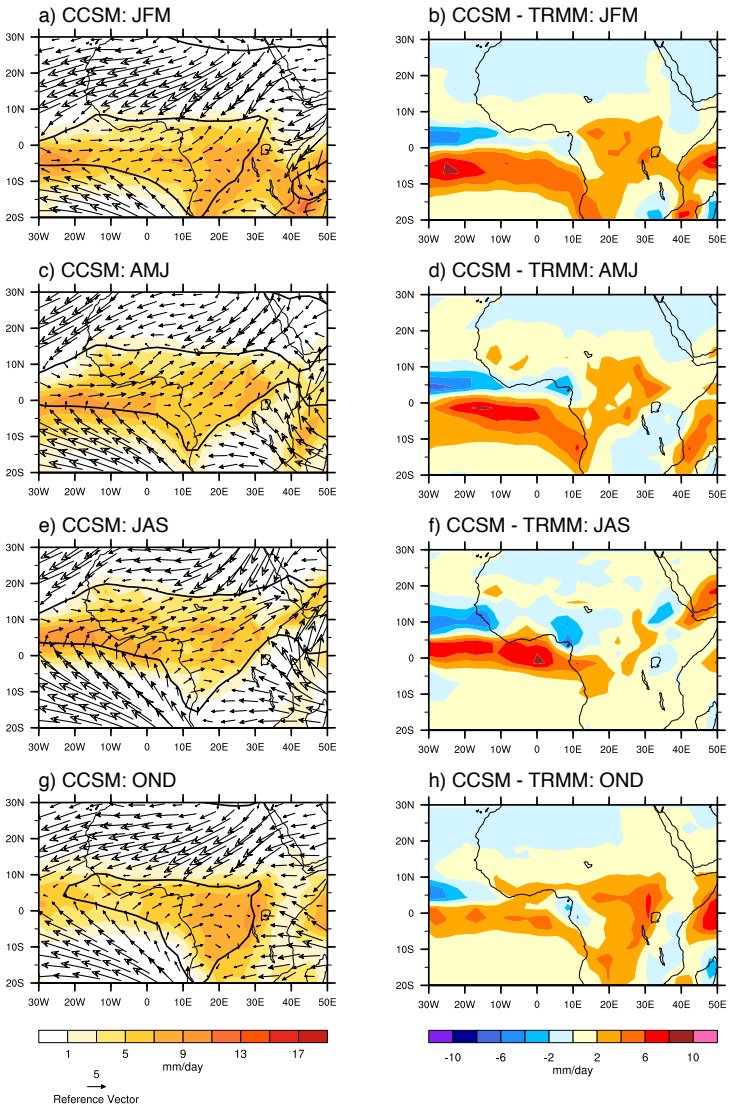


Figure 3.7. Seasonal mean precipitation maps from CCSM (right) with 925hPa winds and the zero line of zonal wind (same as Figure 1). Difference between CCSM and TRMM (left). Units of precipitation are in mm day^{-1}.

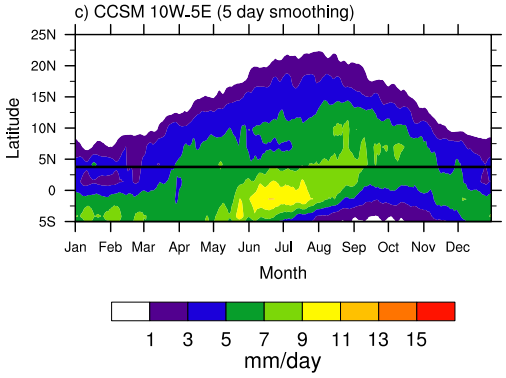


Figure 3.8. Same as Figure 3, except for CCSM.

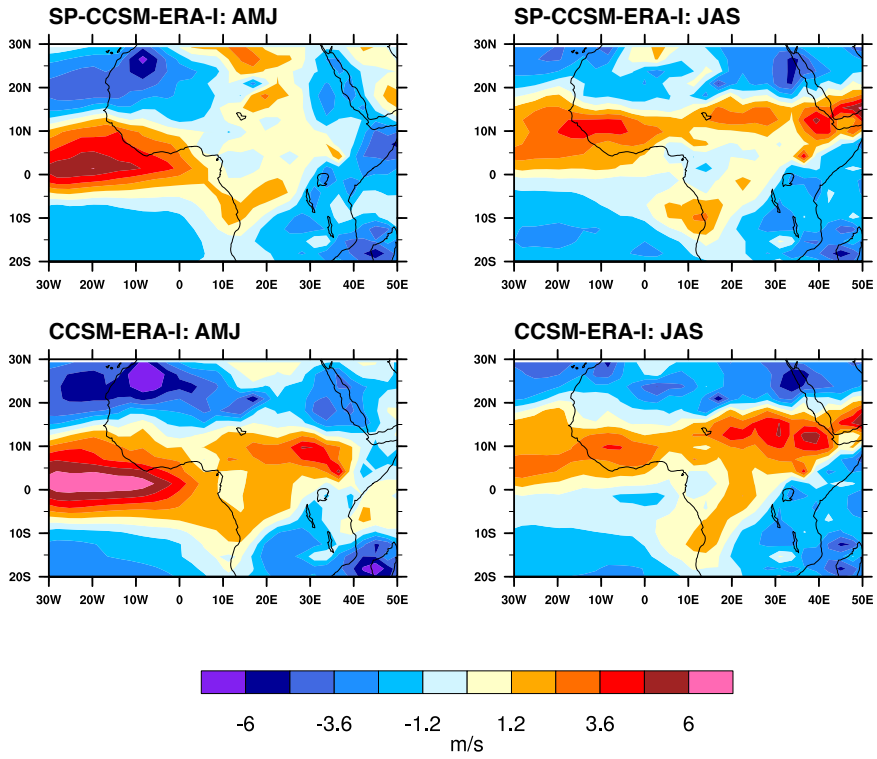


Figure 3.9. Difference between ERA-Interim zonal winds and the SPCCSM (top) and CCSM (bottom) for April-June (left) and July-August (right). Units are m s^{-1}.

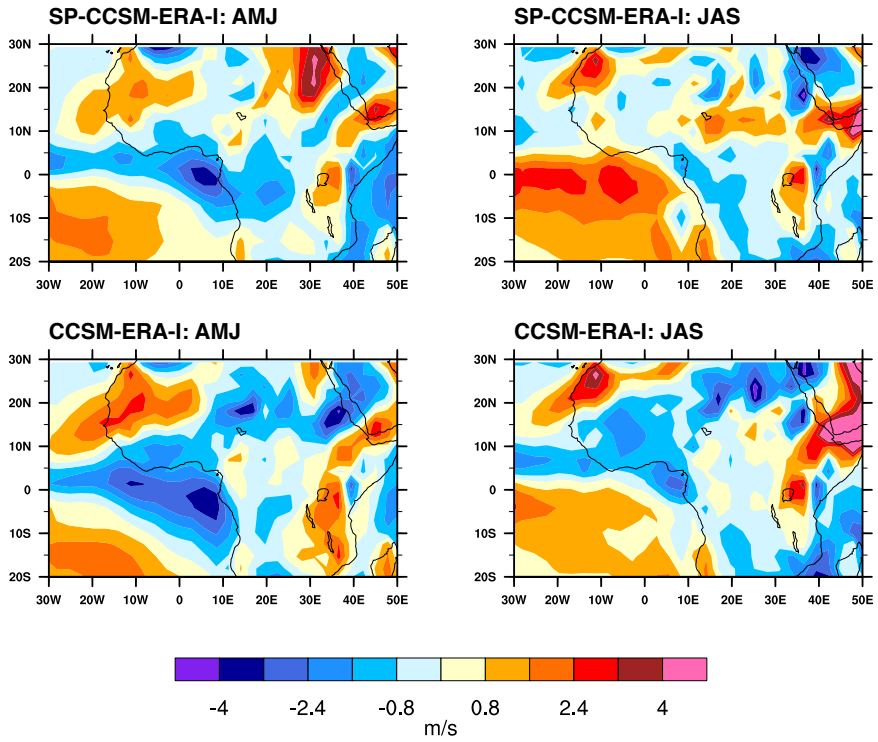


Figure 3.10. Difference between ERA-Interim meridional winds and the SPCCSM (top) and CCSM (bottom) for April-June (left) and July-August (right). Units are m s^{-1}.

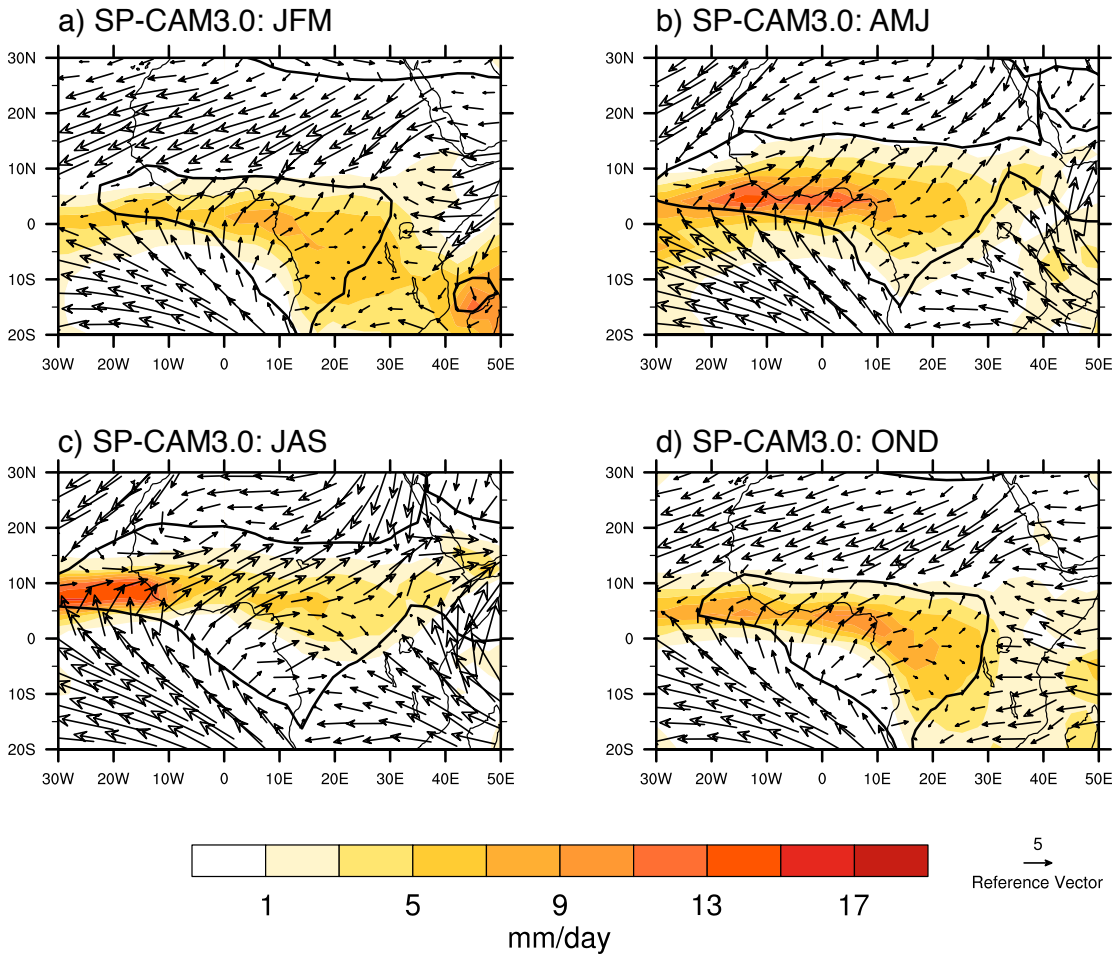


Figure 3.11. Seasonal averages of precipitation from SP-CAM3.0 (filled contours). 925 hPa zonal winds (vectors) and the zero line of zonal wind (black contour). Same as Figure 2.

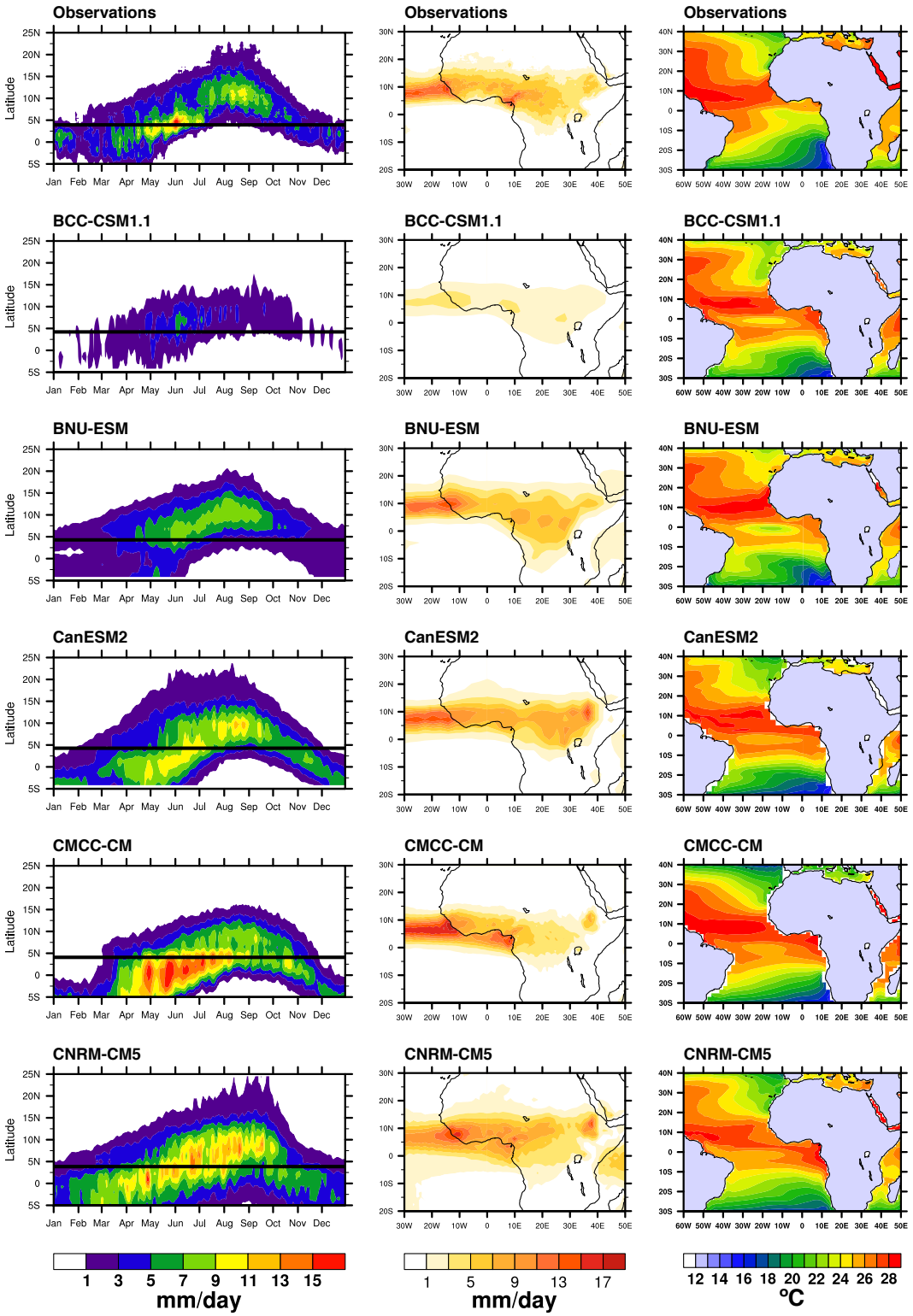


Figure 3.12. Seasonal averages of precipitation and SSTs from the CMIP5 models. Time-latitude cross sections of seasonal daily mean precipitation averaged between 10ºW and 5ºE and smoothed with a 5-day running average (left). July, August, September mean precipitation maps (middle). June-September averaged SSTs (right).

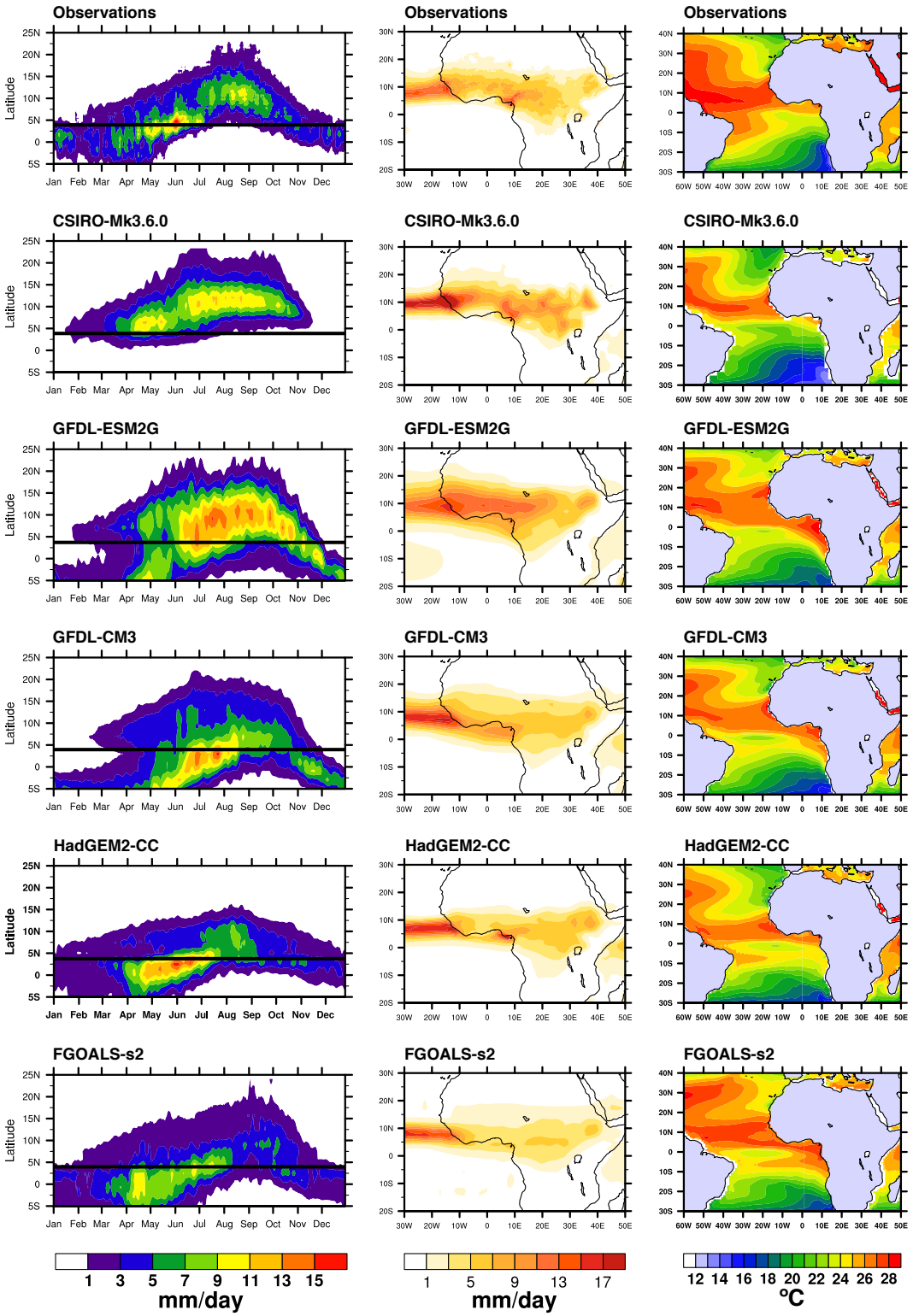


Figure 3.12 continued.

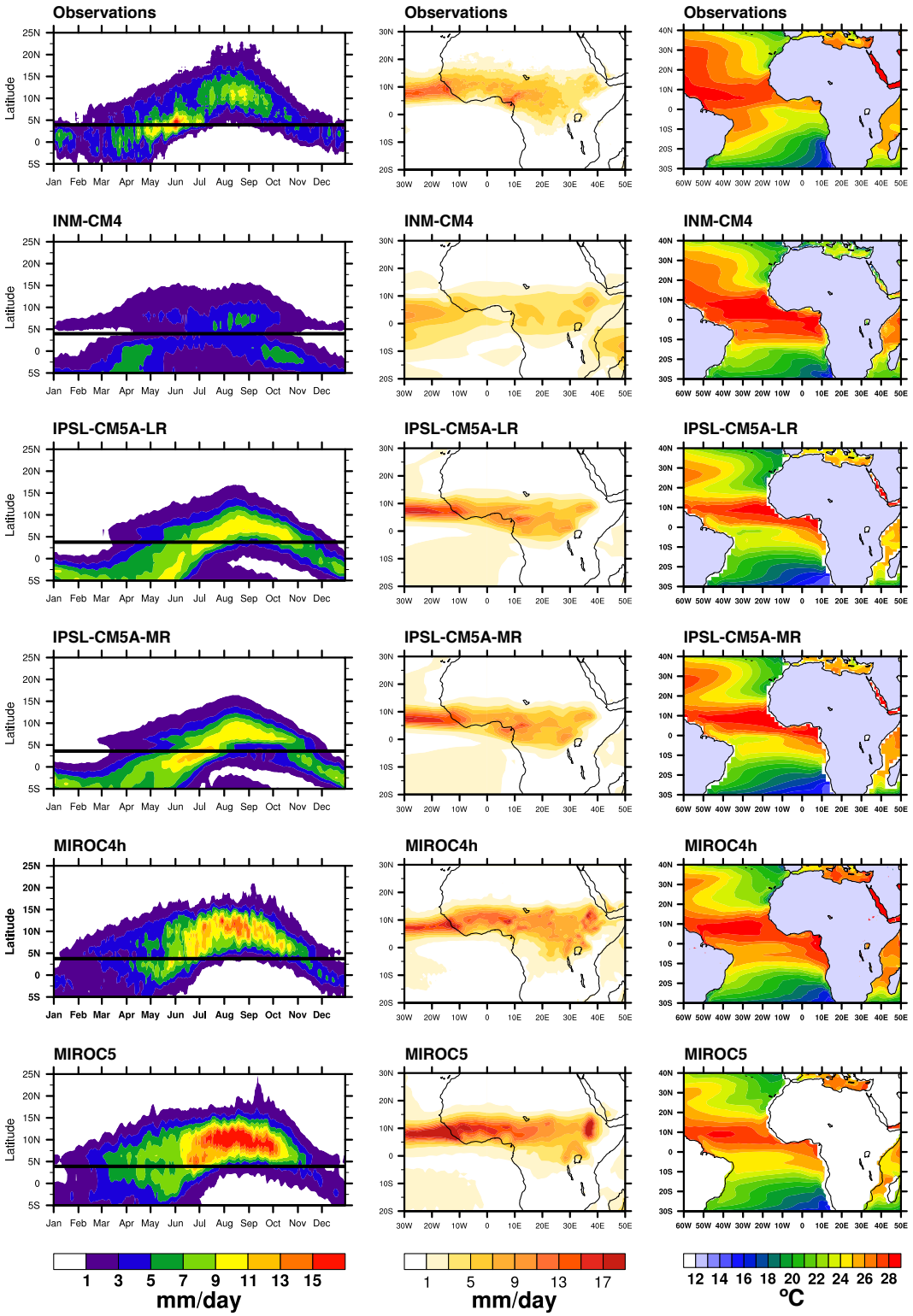


Figure 3.12 continued.

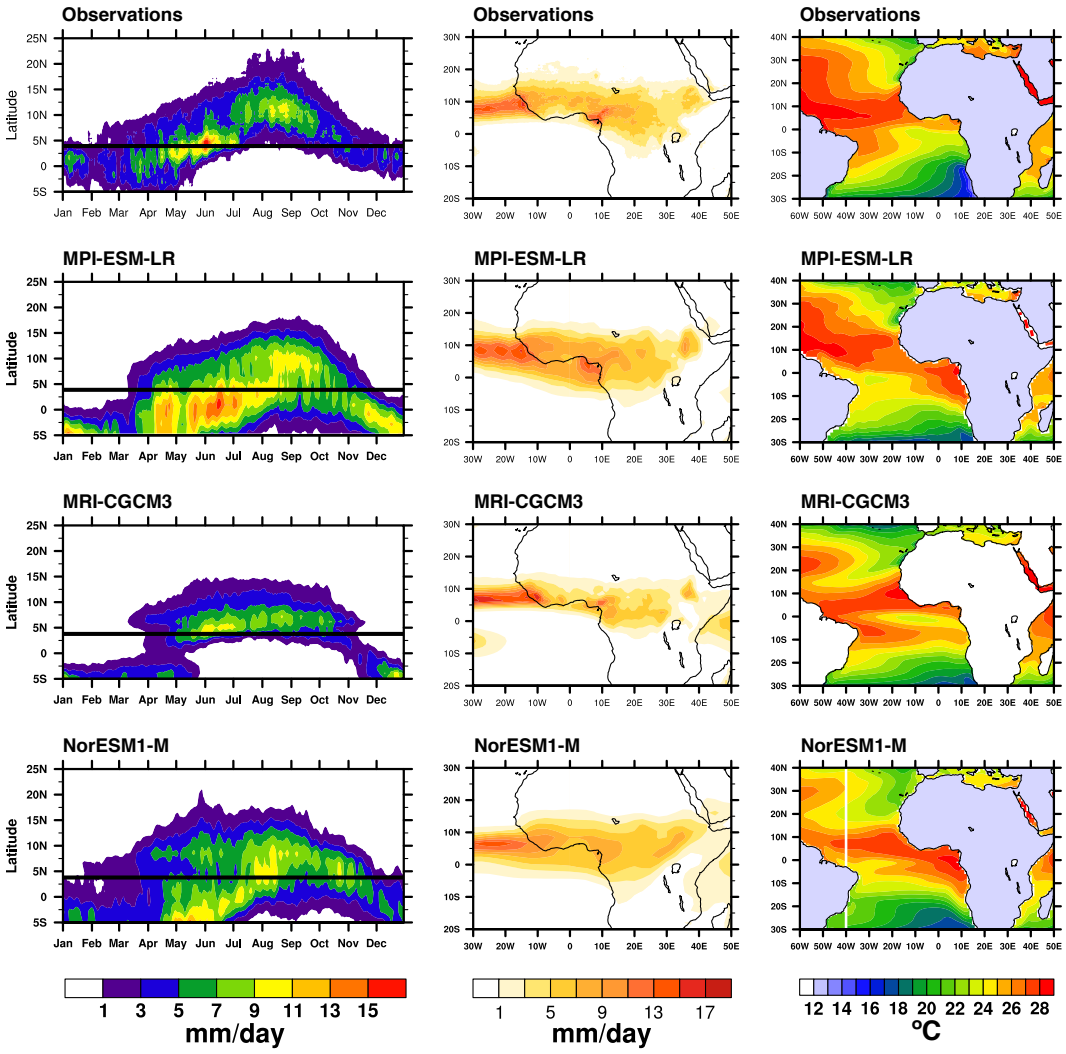


Figure 3.12 continued.

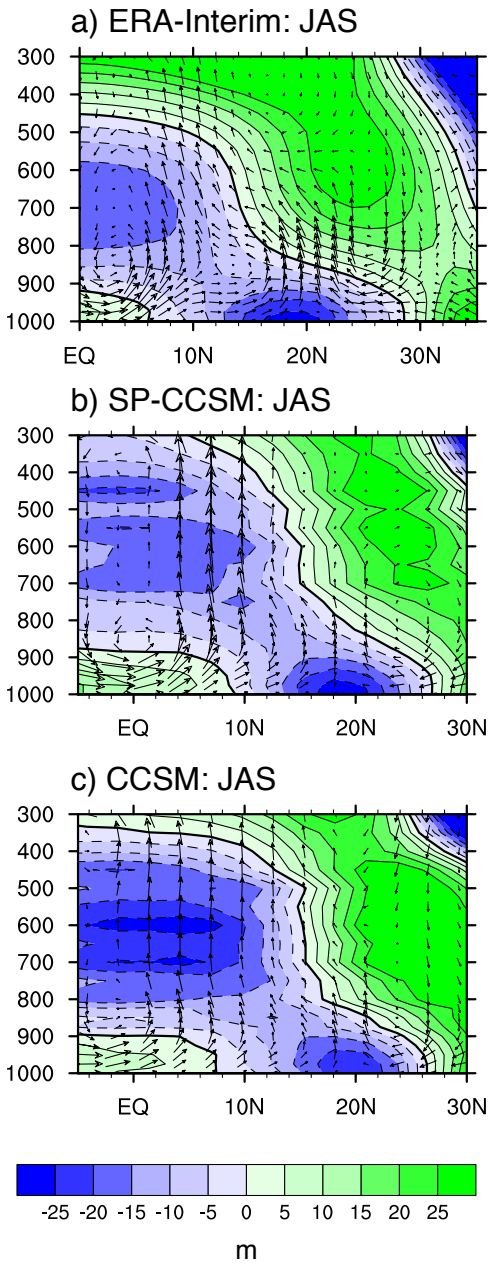


Figure 3.13. Latitude-height cross sections of anomalous geopotential height relative to the meridional average at each pressure level (filled contours). Wind vectors are the meridional and vertical winds. Vertical winds have been scaled to be shown on the plot.

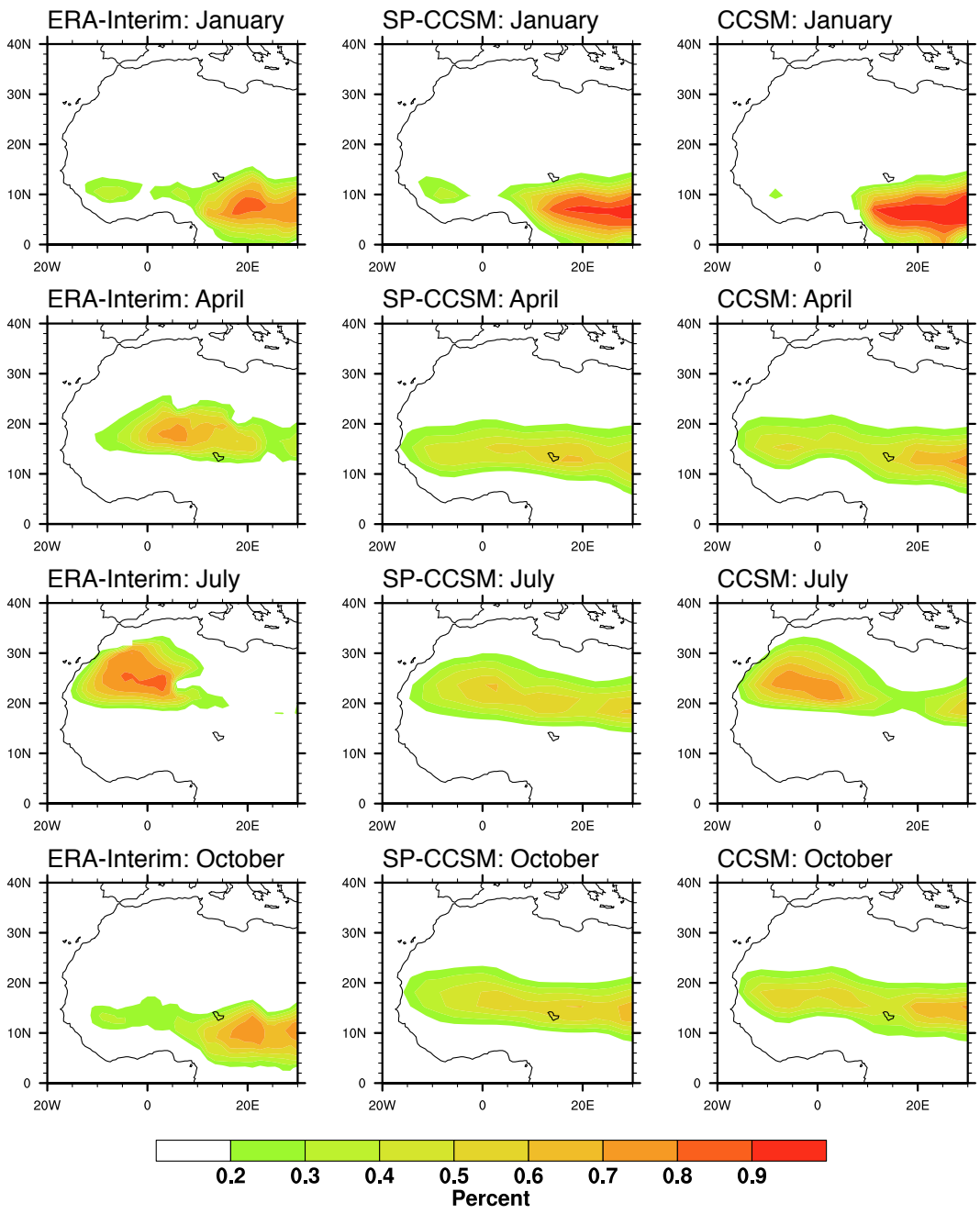


Figure 3.14. Seasonal cycle of the WAHL from ERA-Interim (left), SP-CCSM (middle) and CCSM (right). Plotted here is the frequency of occurrence of the WAHL position, based on the LLAT for January, April, July and October. Units are in percent.

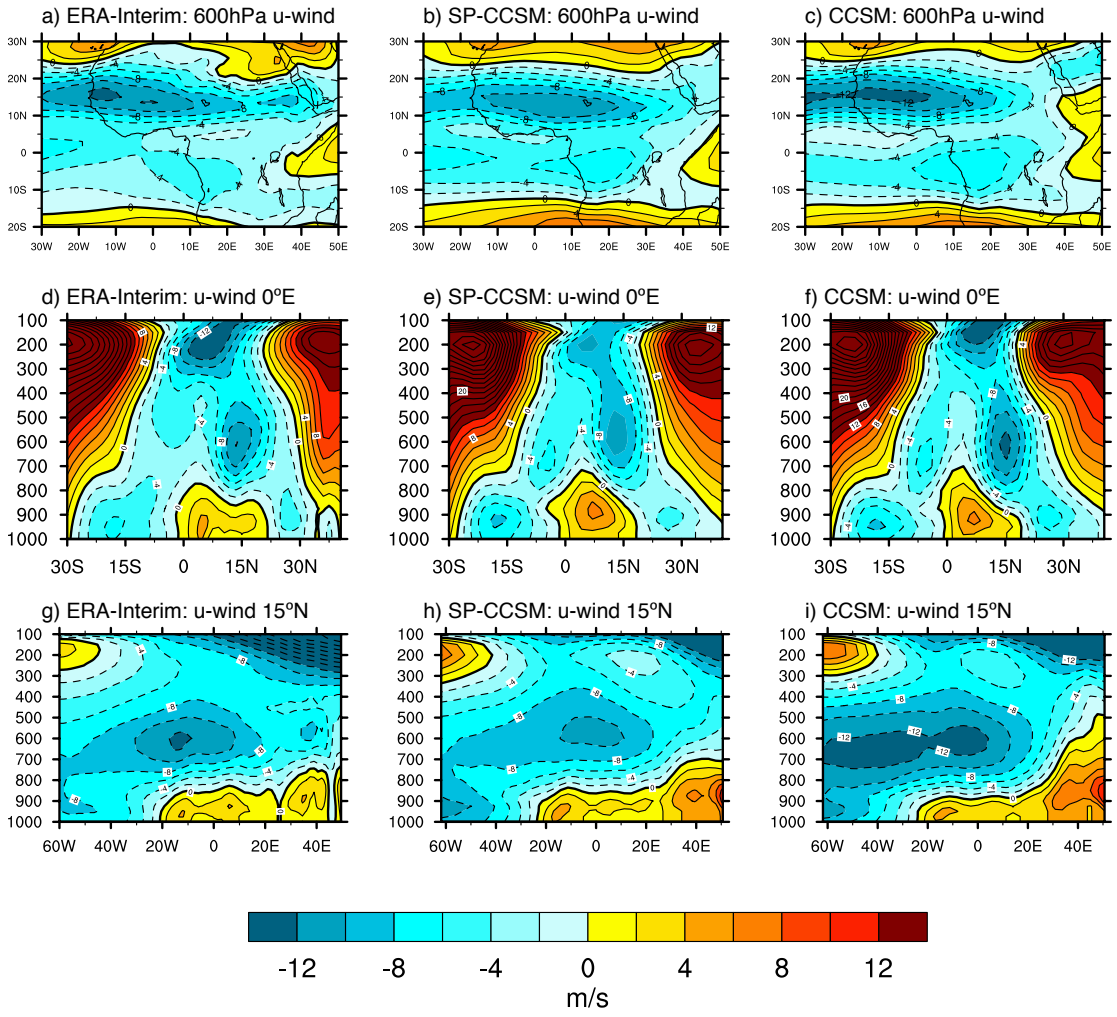


Figure 3.15. July-September averages of zonal wind at 600 hPa (top), meridional height cross section of zonal wind along 0ºE (middle) and, zonal height cross section of zonal wind along 15ºE for ERA-Interim, SP-CCSM and CCSM. Units are in m s^{-1}

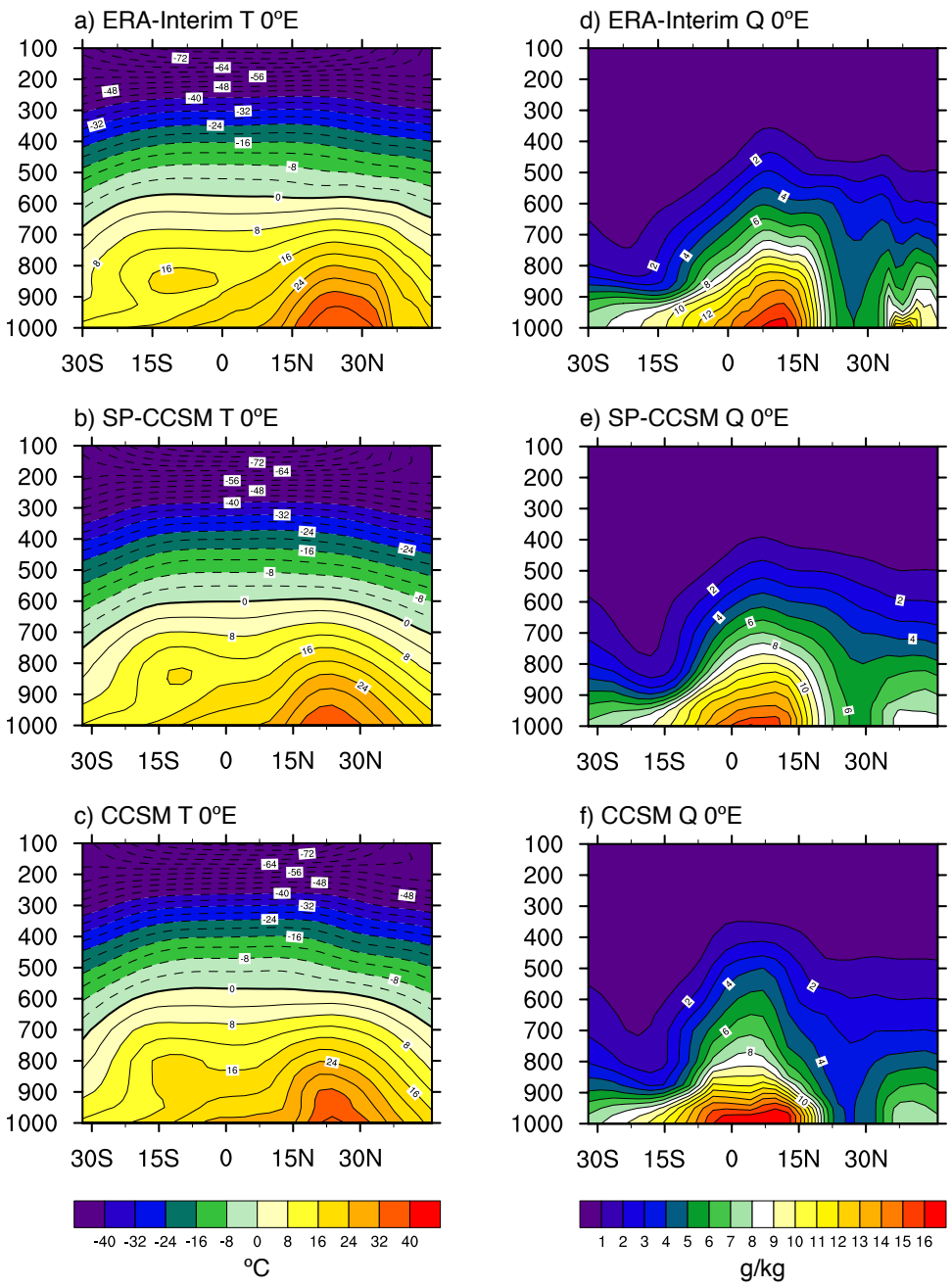


Figure 3.16. July-September averaged meridional cross sections at 0ºE of temperature (left) and specific humidity (right). Temperature is in degrees C and specific humidity is in g/kg.

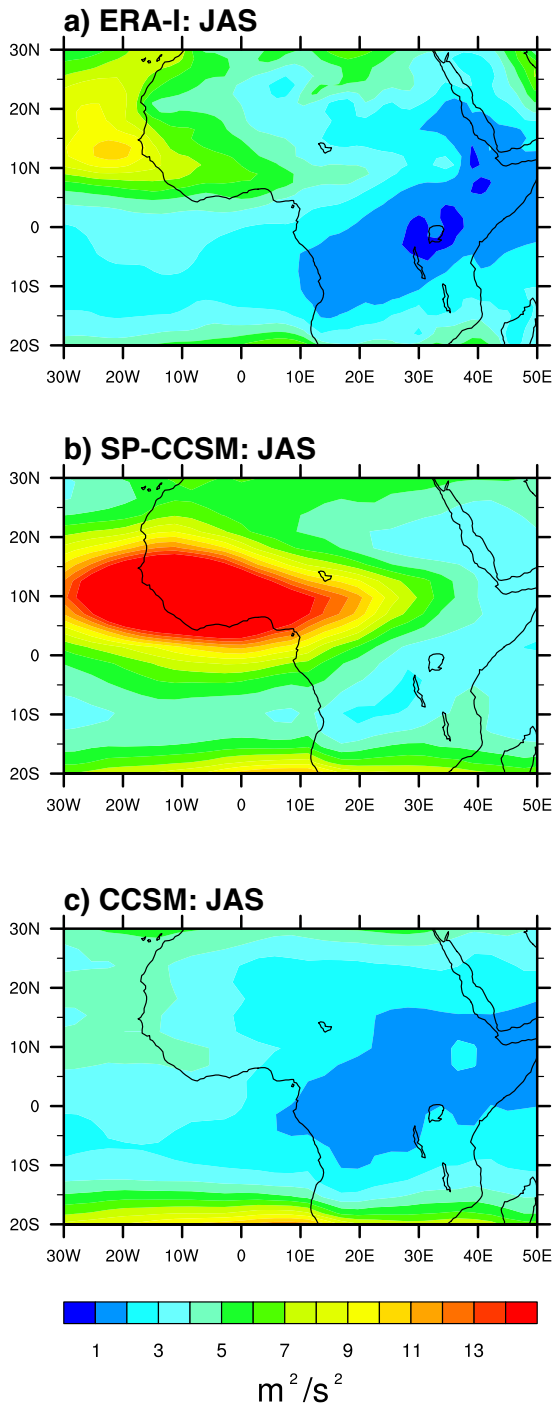


Figure 3.17. July-September averaged eddy kinetic energy (EKE) from ERA-Interim, SP-CCSM and CCSM. Units are in m2/s2. This is a measure of African easterly wave activity.

CHAPTER 4

AFRICAN EASTERLY WAVES

4.1 INTRODUCTION

African easterly waves (AEWs) are an important feature of the summer climate over West Africa and the tropical Atlantic. These waves are periodic oscillations of temperature, vertical motion and winds that propagate from east to west over West Africa. AEWs are synoptic-scale disturbances have periods of approximately 3-5 days, wavelengths of 2000-6000 km, and move at about 7-9 m s^{-1} (Burpee, 1972,1974; Reed et al., 1977). They are the dominant mode of variability over West Africa during the monsoon season and have been shown to be strongly linked to rainfall and convection (Reed et al., 1977, Duvel, 1990: Mathon et al. 2002; Fink and Reiner, 2003; Kiladis et al., 2006; Mekonnen et al., 2006). It is also well established that AEWs act as seed disturbances for Atlantic hurricanes (Carlson, 1969; Duvel, 1990; Avila and Pasch, 1992; Thorncroft and Hodges, 2001; Hopsch et al., 2010).

Given the clear societal relevance of AEWs for both rainfall over West Africa and hurricane development, it is important that global models used for weather and climate prediction are able to simulate these waves. Unfortunately, as with the seasonal cycle of monsoon rainfall (Chapter 3), general circulation models (GCMs) and numerical weather prediction (NWP) models show weak skill in capturing the observed variability, spatial distribution, and intensity of AEWs (Fyfe, 1999; Sander and Jones, 2008; Ruti and Dell'Aquila, 2010). In order to understand why models have difficulty representing AEWs, we must first

discuss the complex nature of these waves and why after decades of research a complete understanding of the initiation, development and maintenance of the waves is still somewhat elusive.

Traditionally, AEWs were thought to develop solely due to the barotropic-baroclinic instability of the mid-tropospheric African easterly jet (AEJ). Burpee (1972) was the first to point out that the AEJ is associated with a reversal of the meridional gradient in potential vorticity (PV) that allows the AEJ to satisfy the Charney-Stern necessary condition for instability (Charney and Stern 1962). Burpee suggested that the hydrodynamic instability of the AEJ was the cause of AEWs in the region. Early idealized modeling studies supported the hypothesis that AEWs developed due to the instabilities associated with the jet (Rennick, 1976; Simmons, 1977; Mass, 1979; Kwon, 1989, Thorncroft and Hoskins, 1994a,b; Thorncroft 1995; Grist et al. 2002). These studies showed that easterly waves comparable to observations could develop on various unstable zonal jets over West Africa and that these waves were driven by both barotropic and baroclinic energy conversions. These studies also indicated that the energetics of AEWs south of the AEJ are dominated by barotropic energy conversions, while baroclinic energy conversions are more important north of the jet.

Recently the idea that dry dynamics alone can generate AEWs has been called into question. Modeling studies have suggested that an energy source other than the instability of the AEJ is needed for AEW initiation and growth (Hall et al. 2006; Thorncroft et al., 2008 Heish and Cook, 2005; 2007; 2008). These studies suggest that diabatic heating associated with convection is a necessary component of the dynamics controlling AEWs.

Current hypotheses argue that convective heating is important for the initiation as well as the maintenance of AEWs. Idealized modeling studies (Thorncroft et al. 2008) as well as observational evidence (Berry and Thorncroft, 2005; Mekonnen et al., 2006; and Kiladis et al., 2006) suggests that convective heating in the vicinity of the Darfur mountains acts as a finite-amplitude perturbation to the atmosphere, which triggers AEWs. The waves then propagate westward feeding off of the barotropic/baroclinic instability of the AEJ. It has also been argued that AEWs may be initiated by the intense convection associated with the ITCZ (Hsieh and Cook, 2005). Furthermore, it has been found that the organized deep convection embedded within the AEWs themselves is critically important for the overall energetics of the waves and that without this convective heat source AEWs cannot persist over Africa for as long as is observed (Berry and Thorncroft, 2012).

In order for GCMs to accurately represent AEWs, they must be able to capture this complex relationship between the large-scale dynamics of the monsoon and convection. This is a tough challenge for GCMs that have coarse spatial and temporal resolutions and must parameterize convection. As suggested by Ruti and Dell'Aquila (2010), the ability of a GCM to simulate AEWs is therefore a good process-oriented evaluation tool for testing the skill of a climate model.

This chapter focuses on how the introduction of the super-parameterization influences the representation of AEWs in CCSM. As will be described in more detail in the methods section, a convective index of AEW activity is used in this study to emphasize the relationship between AEWs and rainfall over Africa. Only a few other studies have attempted to examine AEW activity in CGCMs (Fyfe, 1999; Ruti and Dell'Aquila, 2010) and these studies have focused on

the kinematic properties of AEWs neglecting the importance of convection. My emphasis on convection here makes this study unique.

The remainder of this chapter is organized as follows. Section 2 discusses the observational datasets and method used to evaluate the models. Section 3 investigates the organization of tropical convection during boreal summer. In section 4 the horizontal and vertical structure of the simulated waves is examined. Finally, the energetics of AEWs is explored in Section 5.

4.2 DATA AND METHODOLOGY

In this chapter, outgoing longwave radiation (OLR) is used as a measure of convective activity. The simulated OLR from each model is compared against the daily mean NOAA interpolated OLR dataset (Liebmann, 1996). The NOAA OLR dataset has a resolution of 2.5ºx2.5º and extends from 1979-2010. Other meteorological fields such as winds, streamfunction, vertical velocity, temperature and humidity are from European Centre for Medium-Range Weather Forecasts (ECMWF) Interim reanalysis product (ERA-I; Dee et al., 2011). The ERA-I data have been interpolated onto the 2.5ºx2.5º grid of the OLR dataset.

I am particularly interested in examining the relationship between convection and AEWs. Ultimately I would like to understand if the diabatic heating associated with convection is an important source of energy for the wave dynamics. Unfortunately, ERA-I does not provide the diabatic heating term from the reanalysis. Also, the necessary terms were not included in the CCSM simulation used for this study. While diabatic heating profiles have been estimated from TRMM, the short time scale of the TRMM product as well as the infrequent passage of the satellite radar swath make these products difficult to use for the analysis in this chapter.

For these reasons I have chosen to examine the diabatic heating associated with convection by estimating profiles of the apparent heat source (Q1) using the bulk formula from Lin and Johnson (1996). Where Q_1 is equal to:

$$(1) \qquad Q_1 = c_p \left[\frac{\partial \overline{T}}{\partial t} + \overline{\vec{V}} \cdot \nabla T + \left(\frac{p}{p_0} \right)^{\kappa} \overline{\omega} \frac{\partial \overline{\theta}}{\partial t} \right]$$

In this equation, T is temperature, θ potential temperature, $\kappa = R/c_p$, R is the gas constant for dry air, c_p is the specific heat at constant pressure, p_0 = 1000 hPa and ω is vertical velocity. The overbar here refers to a daily mean average. Q_1 is a measure of diabatic heating and includes the influence of both radiative heating and latent heating.

Although diabatic heating is an output variable from SP-CCSM I have chosen to use the Q1 calculation from above for this model. This way the biases in the calculation of diabatic heating are similar across all three products. I have compared the model derived heating profiles over West Africa and the differences between the two are small.

There are a number of ways to identify AEWs. The traditional synoptic approach focuses on the kinematic properties of AEWs and involves tracking trajectories of wind, pressure and vorticity perturbations to generate track statistics and composites based on the passage of individual waves (Hodges et al., 2003; Berry and Thorncroft, 2005). An alternative approach focuses on the convective signal associated with the waves and uses space-time filtering to build a statistical picture of a "typical" disturbance using regression analysis (Kiladis et al., 2006).

I have chosen to use the latter approach and present in this chapter a statistical representation of AEWs from observations and the two models that uses convection as an indicator for wave activity. This method allows us to focus on the coupling between convection

and AEWs, which is important since ultimately we are concerned about how well global models simulate precipitation over West Africa. The methods used in this chapter to identify AEWs and investigate the horizontal and vertical characteristics of the simulated waves are the same as those used in the Kiladis et al. (2006) (here after K06) observational study. Similar methods have also been used to identify observed characteristics of easterly waves in the West Atlantic and East Pacific ITCZ (Serra et al., 2008; Serra et al., 2010).

For a detailed analysis about the techniques used here please see Wheeler and Kiladis (1999), Wheeler et al. (2000), and K06.

To create an index of AEW activity, OLR is first filtered in both space and time. As shown in K06 the tropical depression or TD band on a Wheeler and Kiladis diagram corresponds to AEW activity and includes westward-propagating waves with wavelengths of 2000-7000km and periods of 2-6 days (See Figure 1, K06 or Figure 4.3 in this chapter). To obtain a statistical representation of the horizontal and vertical structure of AEWs, unfiltered anomalies of winds, streamfunction, temperature, humidity, omega and Q_1 (the apparent heat source) are regressed onto the TD-filtered OLR time series from a number of different basepoints. A one-standard-deviation value of the TD-filtered OLR anomaly time series from each basepoint is used to scale the regression analyses in this study. This allows us to capture the typical scale of the waves for the observations compared to the models. The progression of the waves as they pass the specified basepoint can then be examined by lagging the AEW index and the unfiltered anomalies. This method captures what a "typical" AEW looks like in the models compared to what is observed in the real world and provides a very smooth picture of the characteristics of AEWs. While individual waves will of course exhibit unique mesoscale structure, the methods

used here are a good diagnostic for understanding the relationship between convection and AEWs in CGCMs.

4.3 AEW VARIABILITY

This section examines ability of the models to capture organized tropical convection, in particular AEWs. As mentioned in the methods section, OLR is used as a proxy for precipitation in this chapter. Figure 4.1 shows the average June-September OLR signal for the global tropics and subtropics, where cool colors represent enhanced cloud cover. During boreal summer, enhanced convection occurs over the Indo-Pacific region, the East Pacific, Central America, as well as over Central and West Africa and the Atlantic. As expected from the discussion of the precipitation climatology in Chapter 3, over Africa convection is enhanced over the Ethiopian highlands, East of Cameroon, and along the west coast. Also, moist convection is weak over the Sahara desert, indicated by the large OLR fluxes. In SP-CCSM, the convective regions are broadly the same as seen in observations, although cloud top temperatures appear to be warmer than observed. While this appears to indicate that convection is weaker in SP-CCSM, comparisons with precipitation rates show that in general, SP-CCSM tends to have larger rainfall rates than are observed. This suggests that OLR in SP-CCSM is influenced not only by the strength of the convection, but also by the microphysical properties of the clouds. Over Africa however, there is a clear signature of enhanced convection that spreads out to the Atlantic ocean. In CCSM, cloud-top temperatures appear to be lower than observed, but rain rates in this version of CCSM are typically lower than is found in both the observations and SP-CCSM. Again, microphysical parameterizations potentially play a role in influencing the overall OLR in this model. As expected from Chapter 3, over West Africa during the monsoon season, enhanced

rainfall occurs over the waters of the Gulf of Guinea, something that does not happen in the observations.

Figure 4.2 examines the total daily mean variance of OLR during summer. Here anomalies are created by removing the first three harmonics of the seasonal cycle. As expected, the variability in OLR tends to be largest in regions where convection is strong, specifically in the Indo-Pacific region, in the East Pacific and over West Africa. In general the variability in convection is greater than observed in SP-CCSM and weaker than observed in CCSM. Over West Africa, in the observations, the variability in convection is greatest between 10-20ºN. In SP-CCSM, the variability is larger than observed across all of West Africa, particularly between 0-15ºN. Finally, in CCSM the overall variability tends to be low between the coast and 15ºN, however over the Gulf of Guinea and the Sahara desert, the variability in OLR is larger than is observed.

In order to determine if the variability in convection found in the tropics in the observations and models is due to organized zonally propagating disturbances, we can examine the space-time spectra of OLR. Figure 4.3 shows the average June-September signal-to-noise ratio power spectra from observations and both models for OLR averaged between 15ºS-15ºN for disturbances that are symmetric about the equator (top) and those that are anti-symmetric about the equator (bottom). In the observations significant peaks are found in the symmetric spectra (Figure 4.3a) for the MJO, Kelvin waves, Equatorial Rossby waves and what is commonly referred to as the tropical depression or TD range. As demonstrated in K06, the TD spectral range has been shown to correspond well with AEW activity and includes westward propagating waves with wavelengths of 2000-7000 km and periods of 2-6 days (Figure 4.3a,b).

As will be shown later in this section, easterly waves occur predominantly in the northern hemisphere, so during the boreal summer significant power is also found in the TD range of the antisymmetric space-time spectra (Figure 4.3b). Much like the MJO, easterly waves do not fall along the shallow water dispersion curves, which has led some people to argue that easterly waves may not in fact be waves at all (Kerry Emanuel, personal communication). However this is a discussion for a different study.

The standard CCSM exhibits little to no power in the spectral bands for the MJO or Equatorial Rossby waves. It does have significant power in the Kelvin wave region, although these waves are much faster than observed (Figure 4.3e). There is also no coherent easterly wave power in the CCSM in either the symmetric or antisymmetric spectra (Figure 4.3e,f). The addition of the super-parameterization alters the way that sub-gridscale cloud processes are represented and improves the relationships between the large-scale dynamics and clouds in such a way that tropical wave variability is better represented and closer to the observed spectra. Realistic power is found in both the MJO and Equatorial Rossby wave regions (Figure 4.3c). Kelvin wave activity, while more robust than observed, falls with in range of the dispersion curves (Figure 4.3c). TD activity is also present in the SP-CCSM in both the symmetric and antisymmetric spectra suggesting that AEW activity should be present in this model (Figure 4.3c,d).

I have filtered for easterly wave activity using the methods outlined in Wheeler and Kiladis (1999). This is done by setting everything outside the TD range to zero and converting back to physical space. It is useful to then plot the variance of TD filtered OLR to see where, geographically, easterly wave activity is prominent in observations and the models (Figure 4.4).

There are some distinct regional differences in where easterly wave activity occurs in the observed world compared to both models. Between June-September, in observations, easterly wave activity occurs broadly across most of the tropics, with enhanced easterly wave activity over West Africa and extending into the Atlantic and into the Intra-Americas seas (Figure 4.4a). Easterly wave activity is also found in the central and western Pacific.

In SP-CCSM, easterly wave activity is greatly overestimated over West Africa and the East Atlantic, with the variance in TD filtered OLR being greater than four times larger than observed (Figure 4.4b). There is also somewhat of a southward shift in TD filtered OLR over Africa in SP-CCSM compared to observations. This southward shift corresponds with the region of the precipitation maximum that is found in SP-CCSM (Chapter 3 Figure 3.5e). Interestingly, much like in the observations, easterly wave activity does occur broadly over the tropics in SP-CCSM, however over the central and western Pacific, easterly wave activity is weak compared to observations. It is possible that the amplified easterly wave activity over Africa compared to easterly waves over the tropical oceans is due to differences in convective processes over land compared to oceans.

As expected from the space-time spectra, easterly wave activity in the CCSM is weaker than observed (Figure 4.4c). Over Africa, the only signal in TD-filtered variance in CCSM is found over the Gulf of Guinea where precipitation is a maximum. This variance is less than half of what is observed.

If we compare the ratio of the TD filtered variance of OLR (Figure 4.4) to the total variance in OLR (Figure 4.2) we see that the TD filter captures approximately 20-30% of the total daily mean variance in OLR over West Africa in the observations (Figure 4.5a). In SP-

CCSM on the other hand, the TD filter captures up to 50% of the total variance in OLR (Figure 4.5b). This indicates that AEW activity describes much more of the atmospheric variability over African in the SP-CCSM than is observed. These waves also tend to be much larger in amplitude. In CCSM, easterly wave activity tends to explain less than 15% of the total variance in OLR over the Gulf of Guinea (Figure 4.5c).

4.4 AEW STRUCTURE

The next step is to examine how the horizontal and vertical structures of AEWs in the models compare with observations. The structure of the AEWs is evaluated at two different basepoints, 10ºN,10ºW and 15ºN,17.5ºW. These same basepoints were used in the K06 study and allow us to examine the distinct differences in AEWs that are found north and south of the AEJ. The first basepoint occurs in a region of high OLR variability and is south of the AEJ in a region known to correspond with barotropic energy conversion. The second basepoint is north of the AEJ outside of the observed region of maximum convective variance and is in a region known to be more strongly influenced by baroclinic energy conversions.

4.4.a Basepoint 10ºN,10ºW

4.4.a.i Horizontal Structure

Figure 4.6 shows the observed OLR, 850 hPa streamfunction and winds regressed on the TD-filtered time series from the basepoint 10ºN, 10ºW at various lags. At day 0, centered over the basepoint is a relatively large area of negative OLR anomalies indicating a region of enhanced convection. Both east and west of the convective signal are regions of suppressed convection. The convective signal is co-located with an anomalous cyclone, which indicates that convection occurs within the trough of the AEW at this time. The suppressed convection to the

east of the convective signal is associated with an anomalous anti-cyclone. If we follow the development of this wave at various lags we see that the region of enhanced convection appears 3-4 days before in central/eastern Africa. The K06 study found that a statistically significant convective signal initiated over the Sudan at day -4, however here we do not find a similar significant signal. By selecting basepoint at a different longitudes such as 0ºE or 10ºE, a clear convective signal does appear to initiate in East Africa near the Darfur mountains (not shown). At day -2, a clear convective signal is found at about 7.5ºE, 10ºN, a region typically associated with the amplification of AEWs. This convective signal is centered north and east from the anomalous anticyclone and is positioned within anomalous northerly flow ahead of trough axis. Consistent with K06, the phase relationship between the wave circulation and convection changes as the wave propagates from east to west at this latitude. As the wave propagates westward, the trough catches up to the main convective signal and at day 0 convection is centered within the trough axis. By day +2 the region of enhanced convection has propagated off shore and is behind the trough axis. The statistically significant circulation associated with convection has a broad influence, extending from 20ºS to 30ºN. The convective signal has also taken on a distinct southwest to northeast tilt. By day +4, the influence of this wave has reached 45ºW. The perturbation streamfunction plotted in these figures show the distinct "boat" like horizontal tilts, with a positive tilt to the north and negative tilt to the south of the convective center. This shape implies that barotropic energy conversions are important for waves at this latitude (K06, Hseih and Cook, 2005).

As mentioned previously the regression analysis is scaled by a one standard deviation of the TD-filtered OLR anomaly at the basepoint. At 10ºN, 10ºW in SP-CCSM one-standard-

deviation of the TD-filtered time series is approximately twice as large as observed. In CCSM, on the other hand, one-standard-deviation is only half as strong as observed. For this reason the corresponding Figures (Figure 4.7 and 4.8) are each scaled by sigma. This way our focus can be on the differences in the pattern correlations rather than differences in the magnitudes of the circulation anomalies.

Despite large differences in the magnitudes of the anomalies associated with AEWs, the horizontal structures of the waves that pass over 10ºN are similar in SP-CCSM to observations (Figure 4.7). As with the observations there is a region with large negative OLR anomalies (indicating enhanced convection) centered near the west coast that is flanked on each side by regions of subsidence. The convective anomalies also correspond strongly with anomalies in the 850 hPa circulation, with the region of enhanced convection corresponding with a perturbation cyclone, and each region of suppressed convection corresponding with anomalous anti-cyclones. When compared with observations, the OLR anomalies in SP-CCSM are shifted somewhat to the south of the center of each circulation pattern, which is different than observed. Following the development of these waves, this pattern appears to develop 3-4 days earlier over central/eastern Africa, and propagates westward. Unlike the observations, the wave circulation and convection propagate at the same speeds over land and convection remains within the trough axis until the wave transitions over the ocean. The AEWs found in SP-CCSM also appear to propagate slightly slower than observed, with the disturbances propagating off shore at later lags.

In CCSM (Figure 4.8), while there does appear to be a weak convective signal that is similar to observations, the corresponding circulation is different, and less coherent than observed. The results from the regression analysis are also noisier than observed, and there are

unusual anomalies over the Indian ocean and the Horn of Africa. Following the development of this pattern at different lags, there is no real clear corresponding pattern at lags longer than ± 2 day. The weak convective signal in CCSM is always found in the region of southerlies behind the trough axis. The circulation anomalies appear to travel at the same speed as the convective anomalies.

4.4.a.ii Vertical Structure

Figure 4.9 shows the vertical cross sections of observed meridional wind along 10ºN, regressed onto the TD-filtered OLR time series at lag ± 2 days. The vertical structure of the observed AEWs south of the AEJ exhibits the distinctive first baroclinic mode, with meridional winds changing with height at approximately 300hPa. At low levels there is very little tilt in the meridional winds with height, indicating that barotropic energy conversions are important for AEWs in this region. The thick black line on each panel of Figure 4.9 highlights the position of peak convection, which can also be found in the OLR lag-regression plot above each panel. Remember, peak convection roughly corresponds to a minimum in OLR. As pointed out above with the horizontal lag-regression plots, the region of peak convection shifts from ahead of the trough in northerlies on day -2, to the trough axis on day 0, and then behind the trough in anomalous southerlies when the wave propagates off shore on day +2.

As expected, the region of peak convection also corresponds with anomalous vertical motion (Figure 4.9, right). Within the vertical profiles of omega are two distinct maxima, one centered at about 700 hPa and a second at upper levels centered at 400 hPa. As pointed out in K06, it is thought that this structure is associated with two different cloud populations. Vertical profiles of Q1 (Figure 4.10c) show similar peaks in diabatic heating corresponding with both

peaks in omega. This structure indicates that two these regions of enhanced convection are separated by a stable layer centered at 600 hPa.

To further understand the characteristics of convectively-coupled AEWs, the vertical structures of temperature, humidity, and diabatic heating (Q_1) are also be examined (Figure 4.10). The goal here is to describe the vertical profiles of convection that are associated with the passage of AEWs. As I will show, the convective profiles of the AEWs are the same as the profiles found in other tropical convectively coupled waves. For more details about these similarities see Kiladis et al., (2009).

Ahead of the peak in convection, the lower troposphere is anomalously warm and moist, most likely due to the production of shallow cumulus ahead of the peak in deep convection (K06). Directly corresponding with the peak in convection, the atmospheric layer between 850-500hPa is cool and moist. These cool moist conditions also trail the peak in convection by about 10º latitude. The anomalously cool temperatures behind the peak in convection are likely due to adiabatic cooling associated with the peak in vertical ascent found in the same layer. A second cold pool is found near the surface. This cold layer is likely due to convective downdrafts and cold air advection. The secondary peak in vertical motion found in the upper troposphere between 200-400hPa closely corresponds with anomalously warm temperatures. This warming is thought to be due to diabatic heating associated with deep convection. This is supported by the vertical profiles of Q_1 which show enhanced warming at the same level. Behind the main convective signal, at upper levels, anomalously moist conditions persist, likely caused by trailing stratiform convection.

Much like the observations, vertical cross sections of meridional wind regressed on to the TD-filtered time series for SP-CCSM, also display the characteristic first baroclinic mode (Figure 4.11). Between 300-800 hPa meridional winds are also un-tilted, but below 800 hPa the meridional winds tilt slightly to the east. As will be shown in Section 5, baroclinic energy conversions are important at this latitude at low levels for SP-CCSM. This might seem confusing at first, because as we have all learned in the mid-latitudes baroclinic waves typically tilt to the west with height. But remember, in the mid-latitudes the meridional temperature gradient is oriented such a way that cooler temperatures are to the north. Over this part of Africa however, the meridional temperature gradient is reversed such that warmer temperatures are to the north. This explains why we can expect an eastward tilt with height in baroclinic waves over West Africa.

Much like in ERA-I, the region of maximum convection corresponds with enhanced vertical motion, although the anomalous vertical motion associated with AEWs in SP-CCSM are an order of magnitude larger than is observed. Also, there is only one maximum in the omega profile centered at about 400 hPa. The vertical profiles of convection associated with AEWs in this model do not exhibit the same stable layer at 750 hPa found in the observation. Both the vertical profiles of diabatic heating (Q1) and specific humidity also only display one vertical peak (Figure 4.12). This highlights one of the weaknesses of the super-parameterization, that the vertical resolution of the embedded in the CRM is too coarse to capture the fine scale details associated with deep convection in the tropics.

The vertical profiles of temperature are comparable to observations, with a warm signal ahead of the peak in convection, cool anomalies in the mid to lower troposphere trailing the peak

in convection and warming between 200-400 hPa associated with diabatic heating from convection. While there is a weak signature of warming and moistening ahead of the deep convection which may correspond with the development of shallow convection, there is no signature of the development of trailing stratiform behind the region of deep convection. This may be due in part to the intense vertical motion associated with the convection.

In CCSM, the vertical profiles of meridional wind, omega, temperature, humidity and Q_1 display distinct differences from observations (Figures 4.13 and 4.14). Convection in this model always occurs ahead of the trough axis in a region of anomalous northerlies. As expected from the horizontal maps of AEWs, the meridional wind anomalies associated with convection are much weaker than observed. At lag -2 days and lag day 0 there is noticeable eastward tilt with height in the meridional winds below 800 hPa (Figure 4.13) . The profiles of omega are very top-heavy, with the maximum uplift above 400 hPa. The vertical profiles of diabatic heating are also top-heavy, with positive values of Q_1 only occurring above 600 hPa. While the signature of shallow convection at low levels ahead of the peak in deep convection is strong in the humidity and temperature plots, the peak in convection corresponds with weak positive anomalies of moisture and temperature at upper levels, associated with the top-heavy convection found in the other vertical profiles.

We can now examine the structure of the waves that propagate north of the AEJ.

4.4.b Basepoint 15ºN,17.5ºW

4.4.b.i Horizontal Structure

Figure 4.15 shows the horizontal evolution of OLR and the 850 hPa circulation at the basepoint 15ºN, 17.5ºN for the day -2 to day +2 from observations. As with the previous

basepoint, the convective anomalies begin over central/eastern Africa 3-4 days earlier and propagate westward along 15ºN. The corresponding circulation anomalies are shifted north east of the peak in convection compared to the previous basepoint. At all lags, the convection and the circulation propagate at the same speed, and the convective signal is located in strong southerlies, behind the trough axis.

In SP-CCSM, the variance in TD-filtered OLR is half what was found at the previous basepoint. The waves that pass over the basepoint 15ºN, 17.5ºW appear to generate south of 15ºN at approximately 10ºN, 20ºE (Figure 4.16). The anomalous convection and the corresponding circulation curve northward from this point. Unlike the observations, the convective anomalies and the circulation are centered about the same point, and as with the previous basepoint, enhanced convection is found to occur within the trough axis. These waves move slower than the observed waves and do not propagate as far off shore. It appears that all of the AEWs in SP-CCSM generate in the region of maximum precipitation along the Gulf of Guinea.

In CCSM, the statistically significant convective signature does not correspond to a statistically significant circulation pattern (no wind vectors). At lags longer than ±2 days, the convective anomalies of the waves dies off.

4.4.b.ii Vertical Structure

The vertical structure of the observed AEWs for the basepoint 15ºN,17.5ºW is shown in Figure 4.18. The meridional winds differ from the winds further south with a distinct eastward tilt with height below 500 hPa and opposite tilt above (Figure 4.18). This tilting indicates baroclinic energy conversions maybe important for the waves north of the jet. The vertical

profiles of omega are much different than was found at 10ºN. Figure 4.18 shows near-surface subsidence with upward motion only found above 600 hPa. The vertical profile of diabatic heating shows a similar pattern, with cooling at low levels and warming above 600hPa. The temperature and humidity profiles that correspond with the peak in convection are similar to those found at 10ºN, however at there does not appear to be a signature of shallow convection ahead of the main convective signal (Figure 4.18).

The vertical profiles of the AEWs at 15ºN in SP-CCSM are very similar to those found in the observations, although the easterly tilt in the meridional at low levels is weaker than observed (Figure 4.19). Vertical profiles of omega and diabatic heating are similarly top heavy.

In CCSM, the vertical profiles of meridional wind exhibit large eastward tilt with height from the surface up to 400hPa, with a significant shift found above 300hPa (Figure 4.20). Vertical motion and diabatic heating only occur above 500 hPa, similar to the previous basepoint. A significant dry layer is found between 850 and 500 hPa, which overlays strong surface moisture below this level. The vertical structure of AEWs is distinctly different in CCSM when compared to observations.

4.5 ENERGETICS OF AEWs

Now that we have seen that the observed structure of AEWs is similar in SP-CCSM to observations, we can examine the energy sources that are important for the waves. AEWs can be considered as eddies propagating in a mean flow. One way to understand how these waves are generated and maintained is through an examination of the energy processes that influence these waves. Three main processes dominate the energy sources for these waves: barotropic conversion, baroclinic conversion, and convective diabatic heating that supports the generation

of temperature anomalies. Following the methods used in Lau and Lau (1992) I have derived equations for the rate of change of eddy kinetic energy (K_E, Equation 2) and eddy available potential energy (A_E, Equation 3). These equations below will help guide our understanding of the sources of energy that are important for AEWs.

$$(2)\quad \frac{\partial K_E}{\partial t} = -\overline{\vec{V}_H'(\vec{V}'\cdot\nabla)} - \overline{\vec{V}_H}\cdot\overline{\vec{V}}\cdot\nabla\overline{K_E} - \overline{\vec{V}'\cdot\nabla K_E} - \frac{R}{p}\overline{\omega' T'} - \nabla\cdot(\overline{\vec{V}'\Phi'}) + D$$

$$(3)\quad \frac{\partial A_E}{\partial t} = -\frac{c_p\gamma}{\overline{T}}\overline{\vec{V}_H' T'}\cdot\nabla_H\overline{T} + \frac{R}{p}\overline{\omega' T'} + \frac{\gamma\overline{Q_1' T'}}{\overline{T}}$$

In the above equations $K_E = (1/2)(u'^2 + v'^2)$, $A_E = c_p\gamma\overline{T'^2}/2\overline{T}$, $\gamma = \Gamma_d/(\Gamma_d - \Gamma)$, and Γ_d and Γ are the dry-adiabatic lapse rate and observed lapse rate, respectively. In both equations, primes are the deviation from a ten-day running average, and represent synoptic-scale anomalies. This method does not separate "wave" from "no-wave" disturbances and we will actually be focusing on the energy associated with all synoptic scale disturbances. Results found in this study using a temporal definition of anomalies are comparable to those found in Hsieh and Cook (2007) that looked at AEWs in terms of regional zonal anomalies.

In the K_E equation, the term $-\overline{\vec{V}_H'(\vec{V}'\cdot\nabla)} - \overline{\vec{V}_H}$ is the barotropic energy conversion term and represents the conversion of mean kinetic energy to eddy kinetic energy. This is the mathematical representation of how the eddies can extract energy from the horizontal (u and v) and vertical wind shears. $-\overline{\vec{V}}\cdot\nabla\overline{K_E}$ and $-\overline{\vec{V}'\cdot\nabla K_E}$ terms represent the advection of K_E by the

time mean flow and the perturbation flow, respectively. $-\frac{R}{p}\overline{\omega' T'}$ is the baroclinic energy conversion term and represents the conversion of A_E to K_E due to rising motion in warm anomalies and sinking motion in cold anomalies. Since this term is a source of K_E, but a sink for A_E, it can also be found in the A_E equation only with opposite sign. $-\nabla \cdot (\overline{\vec{V}' \Phi'})$ represents the transport of K_E due to the reorganization of geopotential height anomalies by the anomalous flow. D is the turbulent dissipation of K_E. The two primary terms of interest for AEWs are the barotropic and baroclinic conversions to K_E.

In the A_E equation, $-\frac{c_p \gamma}{\overline{T}}\overline{\vec{V}_H' T'} \cdot \nabla_H \overline{T}$ is the conversion of mean available potential energy to eddy available potential energy due to the eddy heat flux down the mean temperature gradient, i.e, from warm air towards cool air. This term will be positive when the eddy heat flux is directed down the mean temperature gradient. $+\frac{R}{p}\overline{\omega' T'}$ is again, the loss of A_E through baroclinic conversions. Finally $+\frac{\gamma \overline{Q_1' T'}}{\overline{T}}$ is the generation of A_E through diabatic heating and is positive when there is heating in warm regions and cooling in colder regions.

Figure 4.21 shows meridional cross sections of the barotropic and baroclinic conversion terms to eddy kinetic energy for ERA-I and the two models averaged between 20ºW and 10ºE. This longitude region was chosen because it corresponds well with the region of amplified AEW activity in both ERA-I and SP-CCSM. In these figures warm colors indicate regions where

AEWs gain eddy kinetic energy, where as cool colors show regions where eddy kinetic energy is lost.

In ERA-I as well as both models, there are three production regions of K_E due to barotropic conversions. The first is found at upper levels and is associated with the wind shear of the tropical easterly jet and is not thought to be important for AEWs. The second source region is found in the middle troposphere of all three figures. In both ERA-I and SP-CCSM, this production region is centered at ~10ºN and is south of the AEJ in the region that corresponds with the ITCZ. Given the strength of the AEWs in SP-CCSM it is not surprising that the barotropic energy conversion term is larger in the model compared to ERA-I. A source region is also found in the mid-troposphere in CCSM, however it is markedly weaker and positioned far to the south of the jet, over the Gulf of Guinea. The third production region is found at low levels in all three figures and corresponds with the location of the intertropical depression (ITD), where the southwesterly monsoon winds converge with the northeasterly Harmattan winds. In ERA-I, this source region is centered at 17.5ºN whereas in both SP-CCSM and CCSM it is centered farther south at 15ºN. As was discussed in Chapter 3, the monsoon winds do not penetrate as far northward as is observed in either model, so the confluence region of the ITD tends to be displaced southward. Hsieh and Cook (2007) found that the low-level production of K_E is partially offset by the loss of K_E due to frictional dissipation. Unfortunately, neither ERA-I or the models have the necessary terms to do a complete closed energy budget, so I cannot test that hypothesis here.

By breaking apart the barotropic conversion term into its six different components, where:

$$(4)\quad -\overline{\bar{V}_H'(\bar{V}'\cdot\nabla)\bar{V}_H} = \overline{-u'u'\frac{\partial\bar{u}}{\partial x} - u'v'\frac{\partial\bar{u}}{\partial y} - u'v'\frac{\partial\bar{v}}{\partial x} - v'v'\frac{\partial\bar{v}}{\partial y} - u'\omega'\frac{\partial\bar{u}}{\partial p} - v'\omega'\frac{\partial\bar{v}}{\partial p}}$$

we can gain useful insight into the processes that are most important for the production of eddy kinetic energy by the mean flow. Figures 4.22, 4.23, and 4.24 show the breakdown of the barotropic term for ERA-I, SP-CCSM and CCSM respectively. In both ERA-I and SP-CCSM, the production of K_E in the middle and lower troposphere is predominantly influenced by the three terms: the downgradient eddy momentum flux that converts mean kinetic energy to eddy kinetic energy ($u'v'\partial\bar{u}/\partial y$ and $v'v'\partial\bar{v}/\partial y$) and the downgradient transport of easterly momentum that interacts with the vertical wind shear ($u'\omega'\partial\bar{u}/\partial p$). This last term term is influenced by not only the vertical shear of the zonal wind associated with the transition from low level westerlies to midlevel easterlies in the jet (see Chapter 3, Figure 3.15), but also corresponds with perturbations in vertical velocity. Figure 4.25 shows meridional cross sections of the variance in vertical velocity, temperature, and Q1. This figure shows us that the variations in vertical velocity in both ERA-I and SP-CCSM correspond well with variations in convection. This combined with the previous figure supports the idea that the barotropic production of K_E in the mid-to-upper troposphere is influenced by perturbations in vertical velocity that are related to convection.

In CCSM only the downgradient eddy momentum flux that converts mean kinetic energy to eddy kinetic energy ($u'v'\partial\bar{u}/\partial y$) influences the barotropic conversion term. From Chapter 3

we know that the vertical wind shear associated with the AEJ is stronger in CCSM than in SP-CCSM, but Figure 4.25 indicates that the variance in omega is much weaker in CCSM which explains why the $u'\omega'\partial\bar{u}/\partial p$ term is small in CCSM. Convection is also weak in CCSM, which may help explain the weak perturbations in vertical velocity.

To understand how the barotropic term is organized spatially we can turn to maps of the barotropic term averaged over different layers of the atmosphere. Figure 4.26 shows the vertically averaged barotropic term for three layers: the whole depth of the troposphere (975-200 hPa), the lower-troposphere (975-850 hPa), and the middle troposphere (850-450 hPa).

From ERA-I we see that when averaged over the entire depth of the troposphere, the barotropic term supplies energy for eddies over much of West Africa. The largest values occur over the Gulf of Guinea, along the west coast and into the Atlantic, and along the southern coast of West Africa. By examining how this term changes with depth throughout the atmosphere we see that at low-levels the barotropic term is large and positive along the ITD. At midlevels the barotropic term is large south of the AEJ in region corresponding with the ITCZ and off the coast north of 20ºN. This is consistent with the arguments made above.

In both SP-CCSM and CCSM however, the picture is somewhat different. In the models there is a clear delineation between a source of K_E south of 15ºN and a sink of K_E north of 15ºN. In both models the barotropic term gets larger as you move up through the atmosphere. At mid-levels the greatest source of K_E is found in the regions where the maximum rainfall occurs during the summer monsoon, along the coast extending out into the Atlantic in SP-CCSM and over the Gulf of Guinea in CCSM.

Baroclinic overturning is also important for AEWs. In ERA-I as well as both models positive conversions of K_E due to baroclinic processes are found in the lower and upper troposphere, with a region corresponding with the destruction of K_E in between (Figure 4.21). For ERA-I, the region of positive baroclinic energy conversions at low levels extends from 12ºN-25ºN and from the surface to 600 hPa. This is mostly likely due to the relatively warm, dry ascending air found over the Sahara (Figure 4.25). The basepoint 15ºN, 17.5ºW falls within this region, and this supports the idea that waves north of the AEJ are more heavily influenced by baroclinic energy conversions than south of the jet. In both SP-CCSM and CCSM, the baroclinic term at low levels is larger than what is found in ERA-I and extends farther to the south. Based on the variance cross sections of w and T (Figure 4.25) this term is dominated in both models by perturbations in temperature which are larger than observed. Given that the baroclinic conversion to eddy kinetic energy extend farther south in SP-CCSM, this may support the claim stated previously that baroclinic conversions play an important role in dynamics of AEWs at low levels along 10ºN.

In both ERA-I and SP-CCSM large baroclinic overturning is also found between 500-200 hPa centered over 10ºN (Figure 4.21). This is most likely due to the ascent of warm air associated with the latent heat released due to the convection embedded within the AEWs. Below 500 hPa the baroclinic term is negative ($-\omega' T' < 0$) which could be caused by the adiabatic cooling of rising air. The variance in both w and T in CCSM is much weaker that in is found in either ERA-I or SP-CCSM. At upper levels, positive regions of the baroclinic term are confined above 350 hPa and are shifted south centered over 0ºN. The upper level production of K_E corresponds to the region of maximum precipitation in CCSM and from Figure 4.25 it

appears that the variance found in ω at upper levels may be due to the latent heat release due to convection found in the same area (Figure 4.25i).

Spatial maps of the baroclinic term averaged over different layers of the atmosphere tell qualitatively similar stories to what was described above (Figure 4.27). When averaged throughout the depth of the troposphere, the main baroclinic region in ERA-I is found north of 10ºN. North of 10ºN, the baroclinic term is largest in the lower-to-mid troposphere and is negative at upper levels. South of 10ºN between 850-550 hPa, the baroclinic term is typically negative, implying a sink of K_E but a source of A_E (discussed below), however at upper levels this same region becomes a source of K_E. A similar story can be told for SP-CCSM, although the baroclinic term is much larger in northern Africa and extends farther south to the Gulf of Guinea. When vertically averaged throughout the entire depth of the troposphere we see that the baroclinic term is an important source for the eddies along the coast of West Africa in SP-CCSM, which is not true in ERA-I. In CCSM, as expected from the meridional cross section in Figure 4.21, the magnitude of the mid-tropospheric sink of K_E and the upper-tropospheric source of K_E are much smaller than found in both ERA-I and SP-CCSM. These features are thought to be due to temperature anomalies created by convection that then influence vertical motion. Since convection is weak in CCSM, it is not surprising that the baroclinic source and sink of K_E at 10ºN are also weak.

Remember that the baroclinic energy conversion term represents the conversion of eddy available potential energy to eddy kinetic energy. We can now look to the eddy available potential energy equation to investigate potential sources of A_E. Figure 4.28 shows the meridional cross sections of the two other terms associated with the eddy available potential

energy equation. The first term corresponds with the conversion of mean potential energy to eddy available potential energy due to the eddy heat flux along the horizontal mean temperature gradient. Given that the meridional temperature gradient in ERA-I and both models is largest over north Africa it is not surprising that this term is positive north of 10ºN at low-levels. In this region, A_E is generated from mean available potential energy and is then converted to eddy kinetic energy via baroclinic processes. Spatial maps of this term show a similar story (not shown).

The second term corresponds with the generation or destruction of A_E due to diabatic processes. From this point forward I will refer to this term as the "generation term" or G. With this term we can examine how temperature and diabatic heating vary with each other which will help determine if convection is important for the generation and maintenance of AEWs. In ERA-I we see that north of 15ºN, diabatic processes generate A_E at low levels. Farther south, centered at 10ºN G is negative a low levels (750 hPa), but is positive at upper levels (350 hPa). What this tells us is that at low levels, cold temperature anomalies (T'<0) that are created due to adiabatic cooling of rising air will be destroyed by convective heating (Q1>0). At upper levels, warm ascending air due to the large amount of condensational heating from below help to generate eddy available potential energy. Spatial maps of the diabatic term averaged over different layers of the atmosphere (Figure 4.29) show that between 975-600 hPa G is less than zero south of 15ºN whereas between 600-200 hPa G is generally positive. At upper levels, the region where $Q_1'T' > 0$ extends all the way east to the Darfur Mountains and Ethiopian highlands, both regions where it has been hypothesized that AEWs are triggered by convective heating (e.g. Thorncroft et al., 2008). When integrated over the entire depth of the atmosphere, it appears that

G weakly provided a source of A_E between 15ºN and 25ºN, with the largest values occurring off the coast.

In SP-CCSM convection plays a more important role in the energetics of AEWs. When averaged between 20ºW and 10ºE, a conceptually similar picture to the observations is found, although the overall magnitudes of the sources and sinks of A_E are larger in SP-CCSM. At low levels centered at 7ºN, 750 hPa, we see a large region where G is less than zero. Above this, centered at 400 hPa, is a region where G is greater than zero. To fully understand what is going on we also need to examine the vertical averages of this term. Again we see that at low levels, G is negative across much West Africa and extending out into the Atlantic ocean. At upper levels, G is positive in the same region, although the maximum in the positive region is shifted to the south. The source of A_E at upper levels also extends out to the Ethiopian Highlands, as was seen in ERA-I. When averaged throughout the entire depth of troposphere we see that overall, diabatic heating associated with synoptic scale disturbances and AEWs acts as a source of eddy available potential energy. This is one indication that convection drives AEWs in SP-CCSM. One interpretation of this result is that in SP-CCSM diabatic heating associated with convection results in temperature perturbations and these temperature perturbations drive changes in the vertical velocity which ultimately drives the dynamics of the waves.

When we examine the diabatic heating term in CCSM, it is not surprising that the only noticeable values of G are at upper levels. Remember from Section 4 a ii that convection in this model is fairly top-heavy and so we would expect diabatic heating to be larger at upper levels.
to summarize these results, I have shown that in ERA-I and SP-CCSM diabatic heating is a potential source of energy that helps to feed AEWs. Overall, the diabatic heating term plays a

larger role in the energetics of AEWs in SP-CCSM. Convection does not appear to be important for the limited wave activity found in CCSM.

4.6 DISCUSSION

The coupled relationship between AEWs and convection still remains to be an open question in our field. In order for our forecasts of weather and climate to be improved the complex relationships between convection and wave dynamics must be simulated by our models. Observational and modeling studies alike are attempting to tease out the role that convection plays for the initiation, growth and maintenance of AEWs. The goal of all of these studies, including this one, is to improve our overall understand of how these waves work. Hopefully as our theoretical picture and physical understanding of AEWs improves, we can being to modify the physics of our models in ways that will help improve the fidelity of simulations of rainfall over West Africa.

In this study I have shown that the addition of the super-parameterization into the CCSM greatly modifies how tropical convection is organized. I would also argue that the super-parameterization ultimately improves the representation of AEWs. I say this fully acknowledging that the SP-CCSM is not without its own biases, but we have gone from a model where convection is generally unorganized and essentially no wave activity is found over West Africa to a model where AEWs are a robust feature of the variability over West Africa and have similar horizontal and vertical structures to observed waves.

I would further argue that because the SP-CCSM actually simulates AEWs, and these waves have clearly been linked to convection that we might be able to learn more about the important role that convection plays in AEW development.

As was shown in this chapter, AEWs only account for about 20-30% of the total variability in convection over West Africa. As will be discussed further in the next chapter, the remaining variability is in part due to intraseasonal and interannual variations in rainfall, but a large portion of the variability is due to non-wave synoptic and mesoscale convective events. What this means is that convection over West Africa is highly variable, so it is difficult to isolate the specific influence that convection has on the wave dynamics and vice versa.

With the SP-CCSM, we have a situation where AEWs account for more than 50% of the total variability in convection. With this system I have been able to show that it is likely deep convection causes temperature anomalies which ultimately drive the wave dynamics. Given how closely the structure of the simulated waves matches the observed waves, it is possible that the picture we have in SP-CCSM is an extreme view of what occurs in the observed world.

Unfortunately, this is as far as this part of the study could go, but I have a number of ideas about how to really get at how convection influences the waves. The first thing I want to do is perform a new simulation with SP-CCSM that will include many terms that were left out of the first run. These terms would would help close the energy budgets described in Section 5 and would allow me to to determine which terms are currently missing and what role they play.

A second idea is to try to determine if convection is only important for the initiation of AEWs (unlikely) or if the deep convection within the waves is critically important for the wave itself. To do this I would do a series of "forecast" runs where I initiate the standard CCSM with the atmosphere, ocean and land surface conditions of the SP-CCSM and look at how easterly waves develop without the super-parameterization compared to the SP-CCSM. If the waves in the forecast run can maintain their strength and structure it seems likely that convection would be

predominantly important for triggering the waves but that other factors allow the wave to continue propagating.

Finally this was not touched upon here, but I would like to examine the role that surface fluxes of sensible and latent heat have on the wave dynamics. For instance, does the rainfall that is associated with the passage of an AEW influence where subsequent AEWs will occur?

4.7 FIGURES

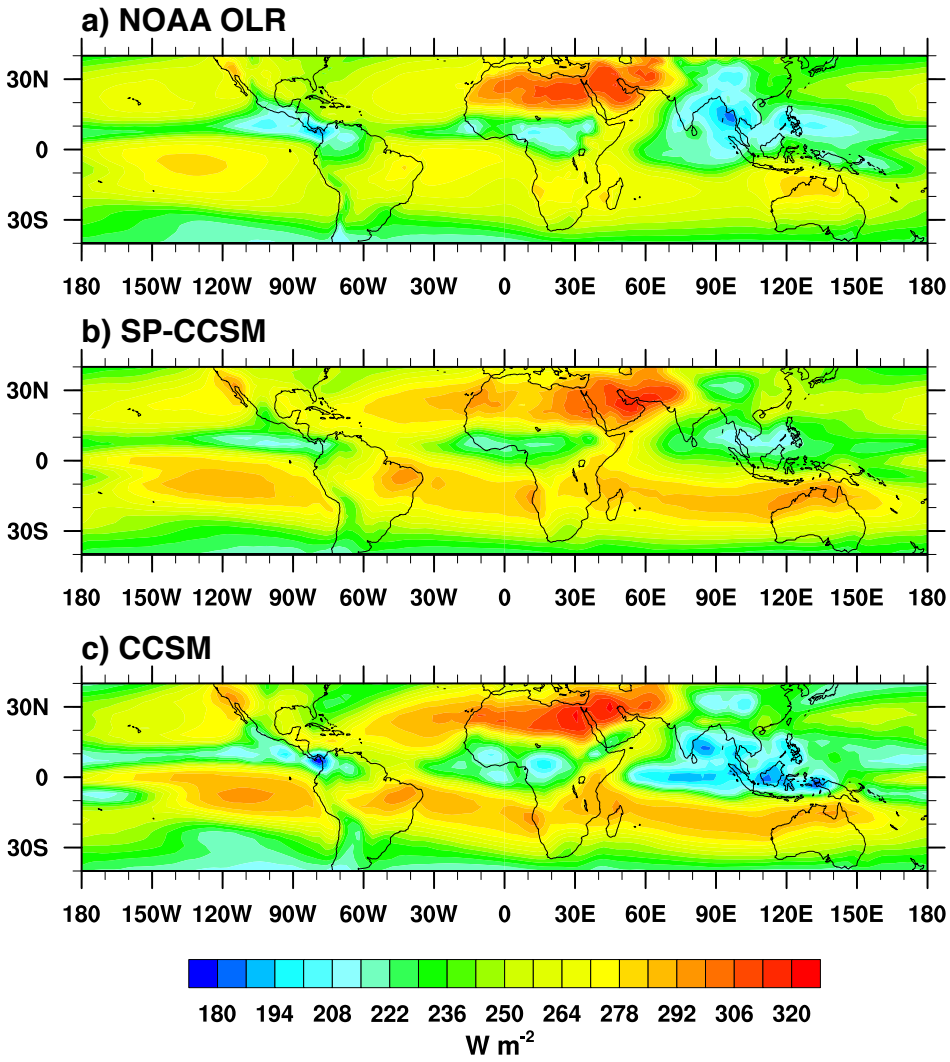


Figure 4.1. June-September mean OLR from a) observations, b) SP-CCSM and c) CCSM. Units are in Wm^{-2}.

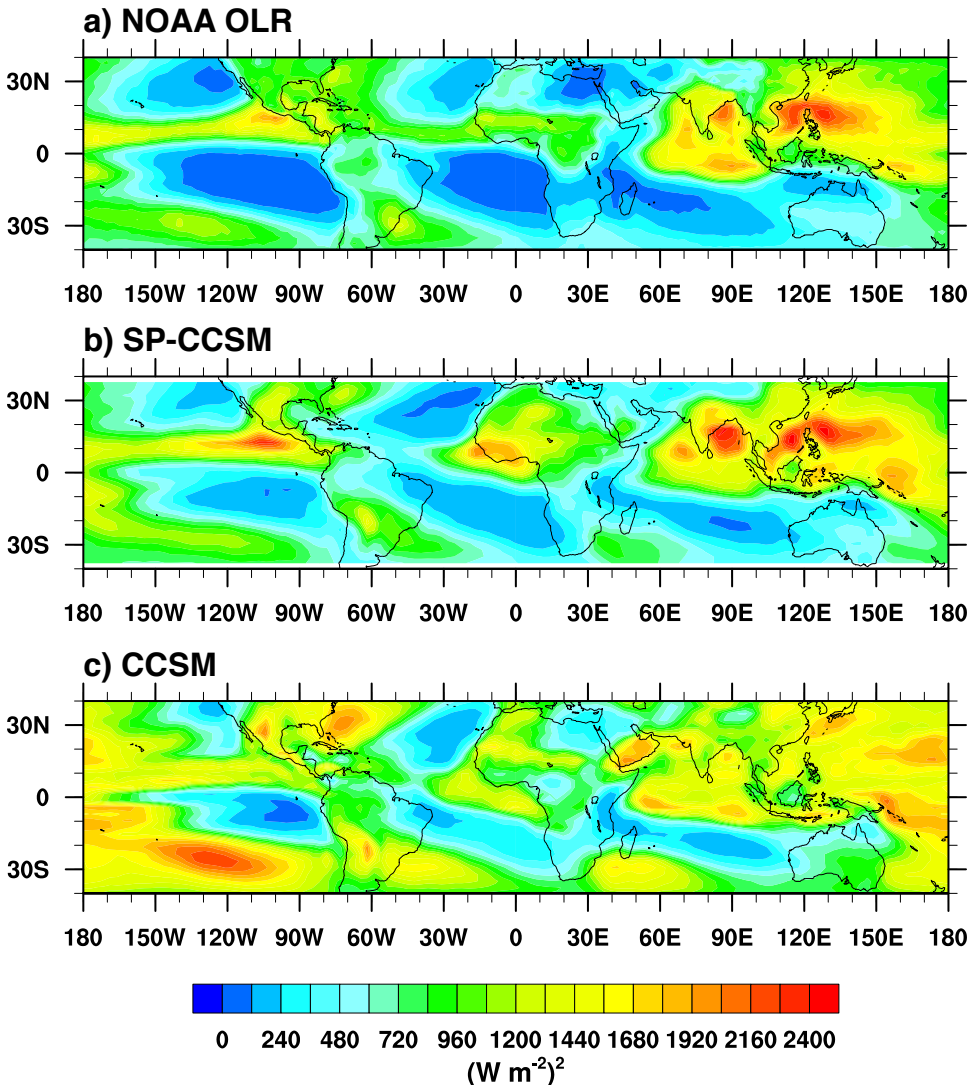


Figure 4.2. The variance June-September OLR from a) observations, b) SP-CCSM and c) CCSM. Anomalies are created by removing first three harmonics of the seasonal cycle. Units are in $(Wm^{-2})^2$.

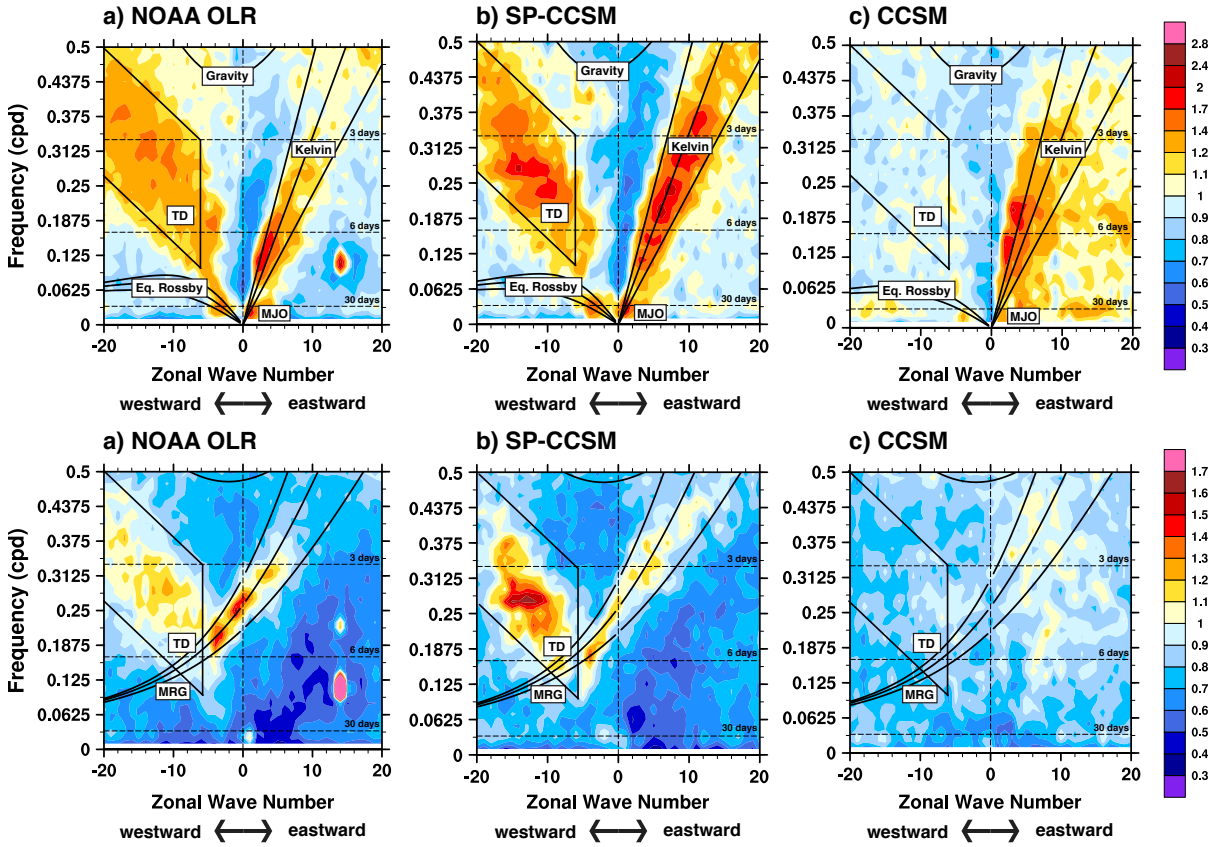


Figure 4.3. Average June-September signal-to-noise space-time spectra averaged between 15ºS-15ºN at all longitudes for disturbances that are symmetric about the equator (top) and antisymmetric about the equator (bottom) from observations (left), SP-CCSM (middle) and CCSM (right).

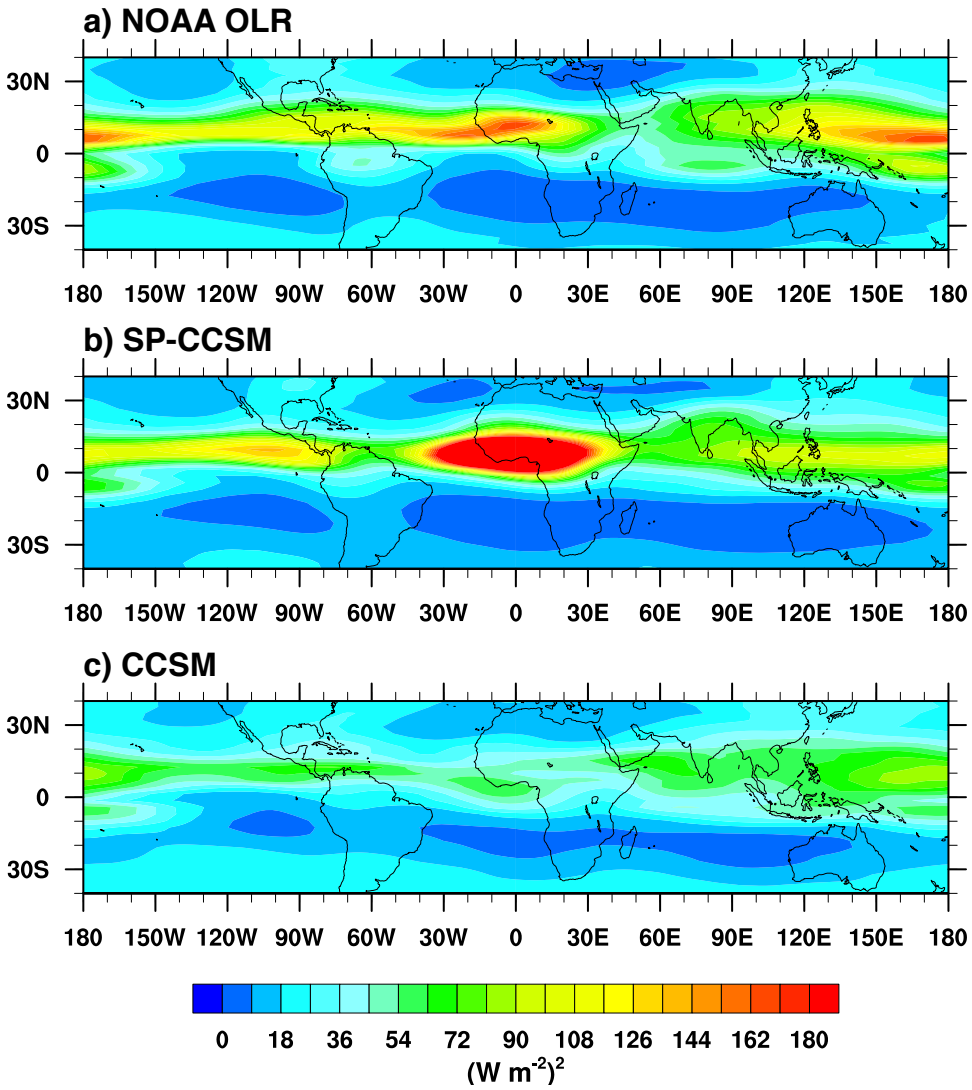


Figure 4.4. Variance of TD-filtered OLR from a) observations, b) SP-CCSM and c) CCSM. Units are in $(Wm^{-2})^2$.

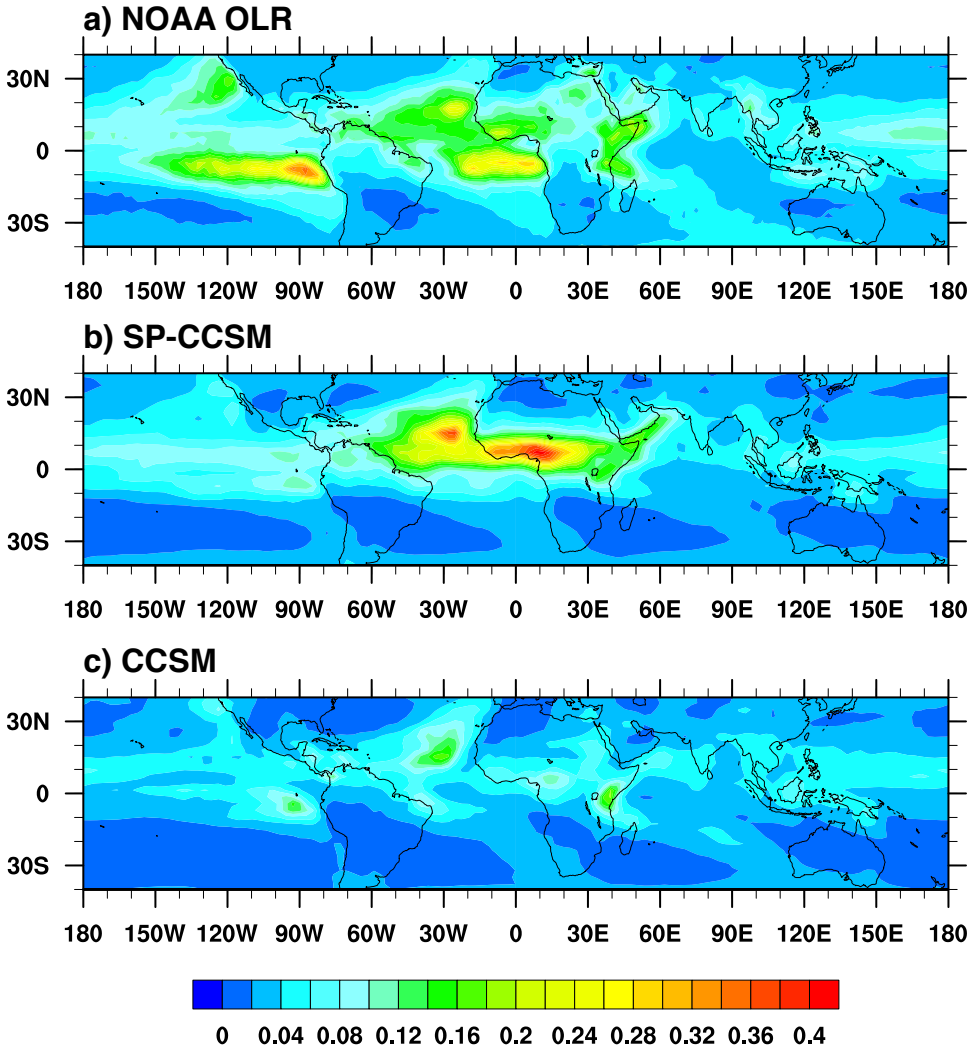


Figure 4.5. Ratio of the variance in TD-filtered OLR (Figure 4) to the total variance in OLR (Figure 2) from a) observations, b)SP-CCSM and c) CCSM.

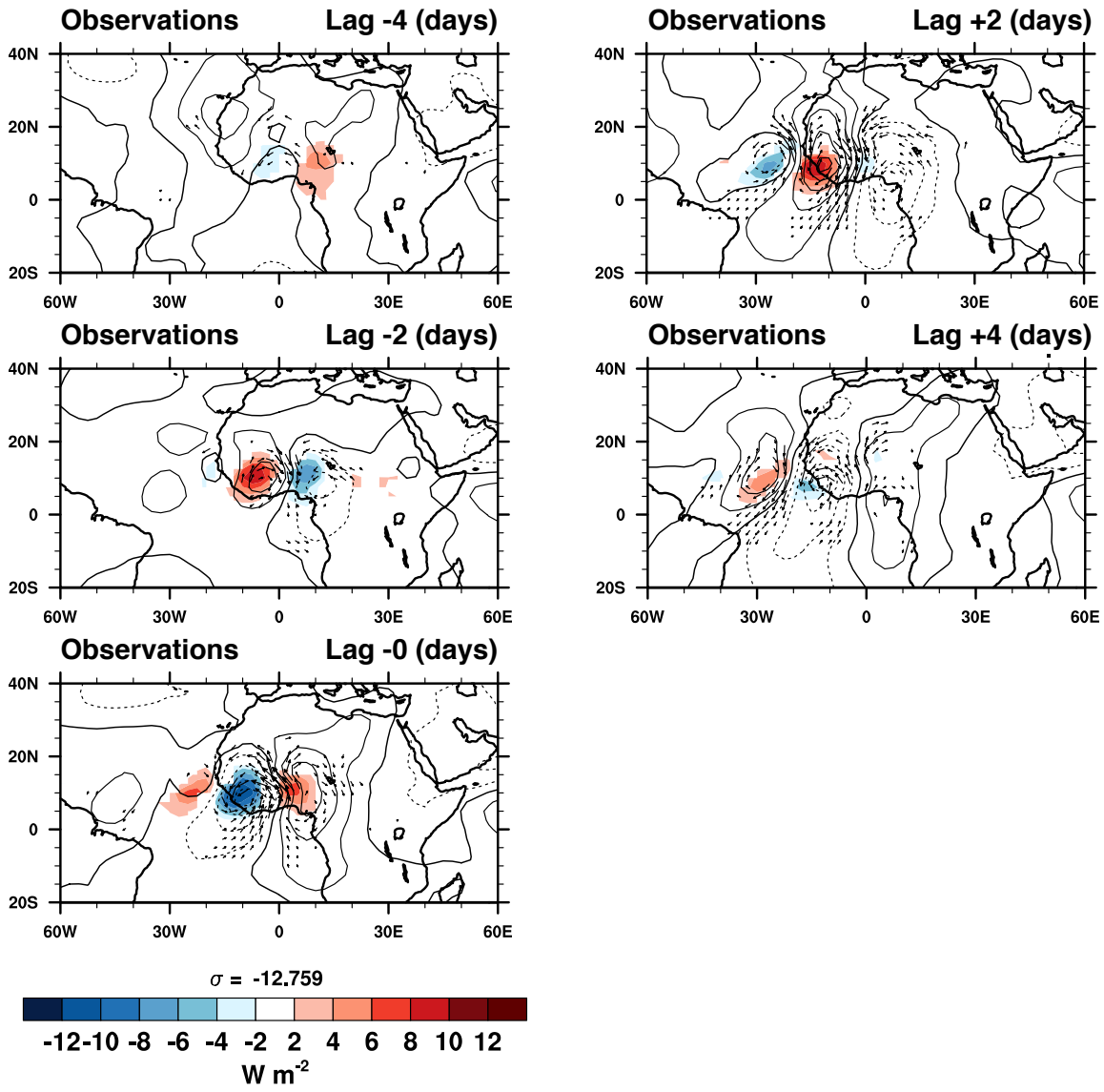


Figure 4.6. Horizontal structure of AEWs at the basepoint 10ºN,10ºW from observations at lag ±4 days. Anomalous OLR and 850 hPa circulation associated with a one standard deviation (-12.759) deviation of the TD-filtered OLR time series at 10ºN,10ºW. Filled contours are anomalies OLR in units of Wm^{-2}. Line contours are the 850 hPa stream function in contoured from $1x10^5$ m^2s^{-1}. Vectors are the 850 hPa winds. Only statistically significant OLR and wind vectors at the 95% confidence level are shown.

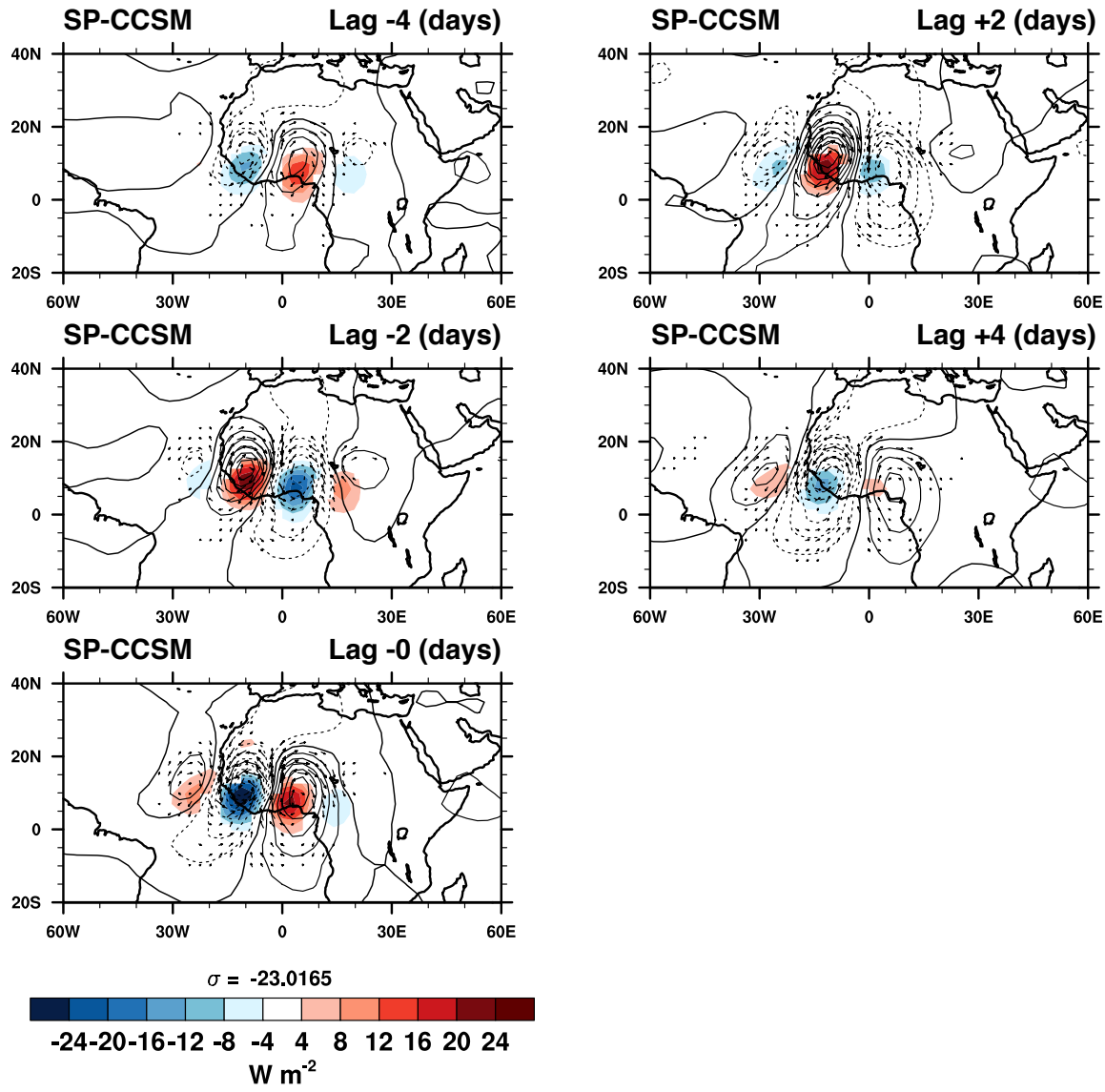


Figure 4.7. Same as Figure 6, except for SP-CCSM. Here the one standard deviation of the TD-filtered OLR time series is -23.0165.

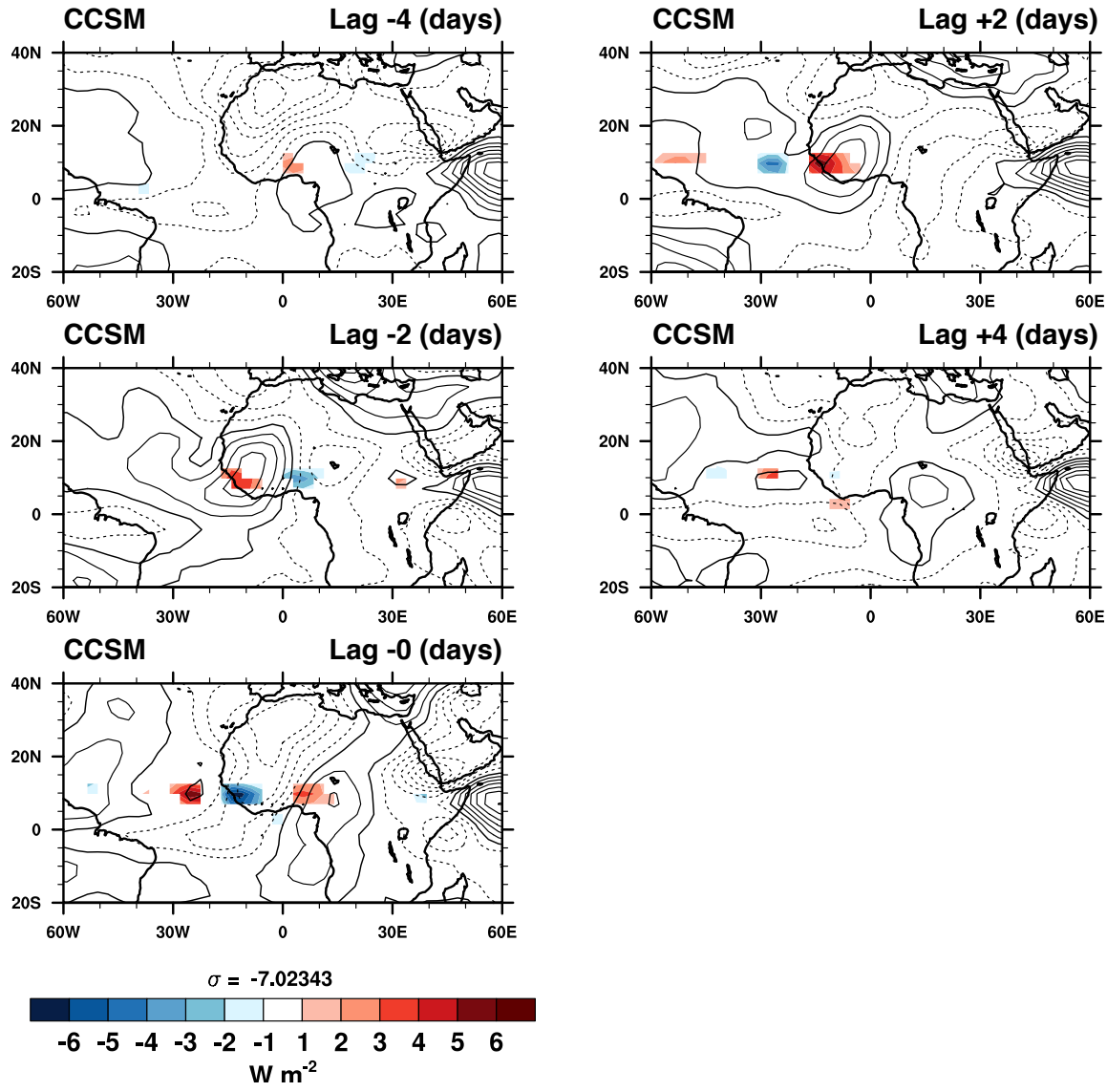
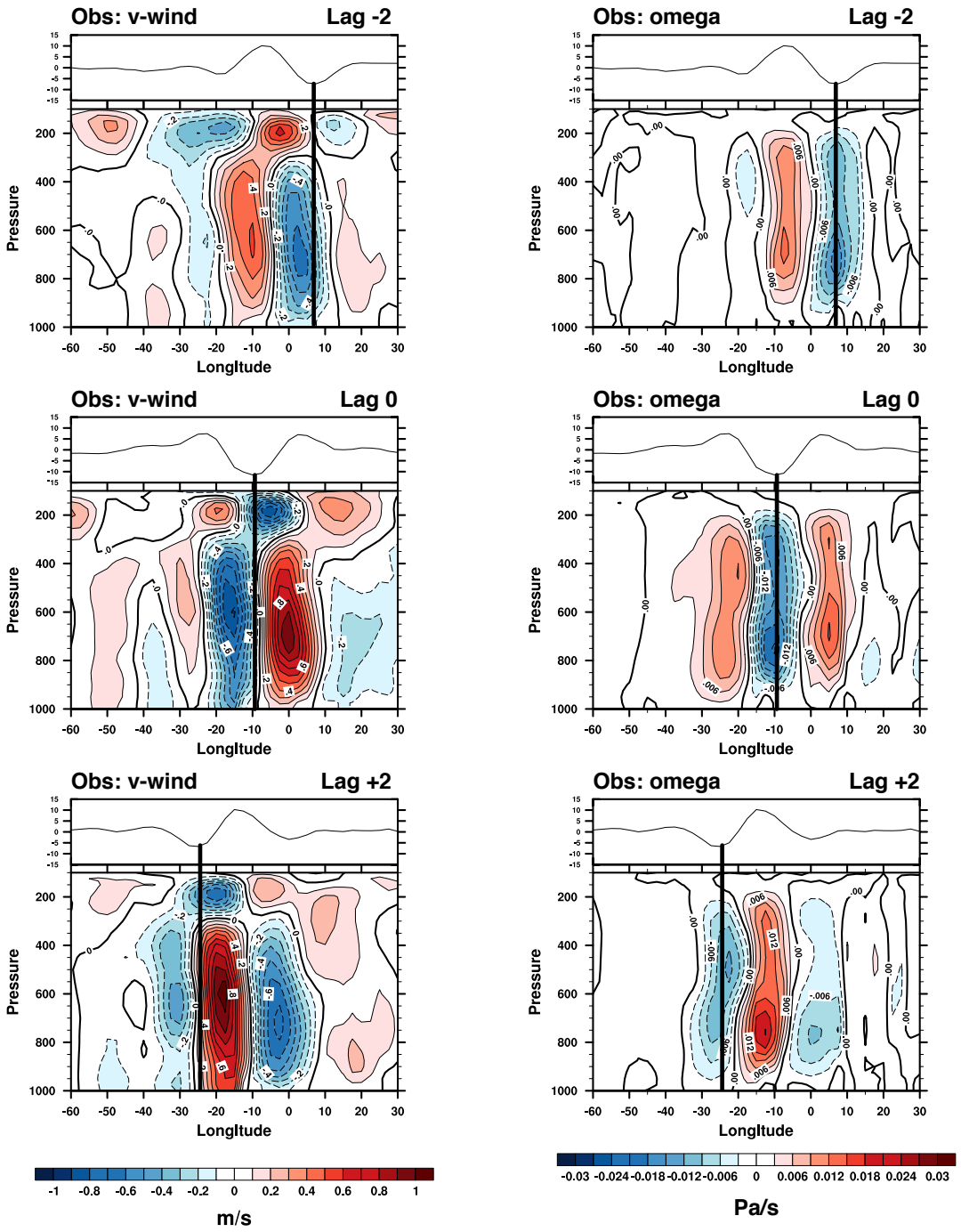


Figure 4.8. Same as Figure 6, except for CCSM. Here the one standard deviation of the TD-filtered OLR time series is -7.02343.



\

Figure 4.9. Zonal-height cross section of anomalous meridional wind (left) and omega (right) along 10ºN associated with the pattern in Figure 6 for lags ±2 days. Units are in m s^{-1} for winds and Pa s^{-1} for omega. The associated OLR anomaly along 10ºN at each lag is shown above each panel. The position of peak convection is highlighted with the thick black line.

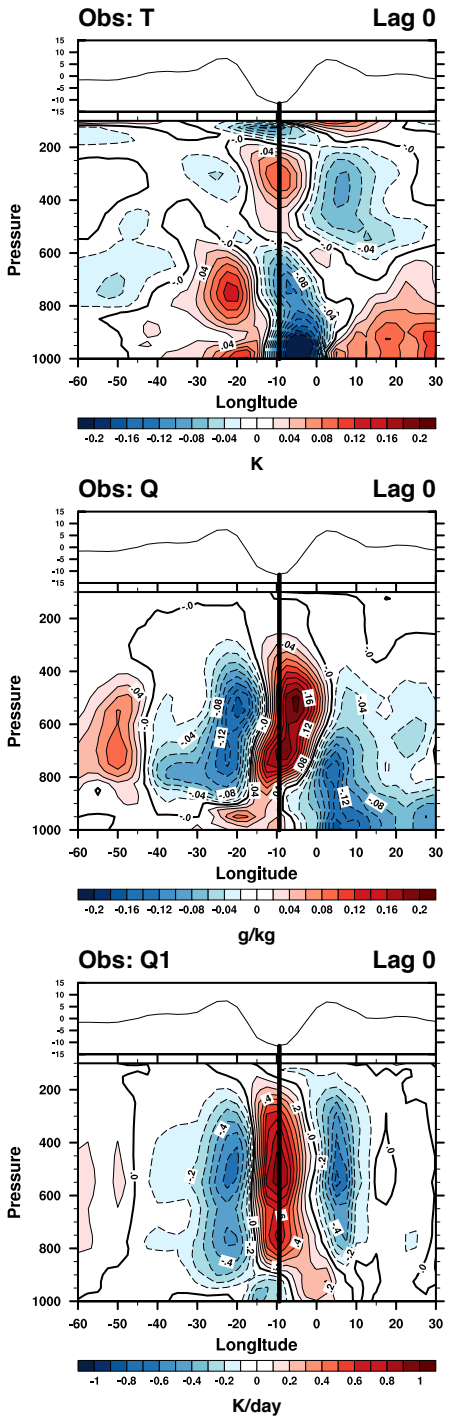


Figure 4.10. Zonal-height cross section of anomalous observed temperature (top) and specific humidity (middle) and the apparent heat source (Q1, bottom) along 10ºN associated with the pattern in Figure 6 at lag 0. Units of temperature are in K, specific humidity is in g kg^{-1}. and Q1 is in K day^{-1}. The associated OLR anomaly along 10ºN at each lag is shown above each panel. The position of peak convection is highlighted with the thick black line.

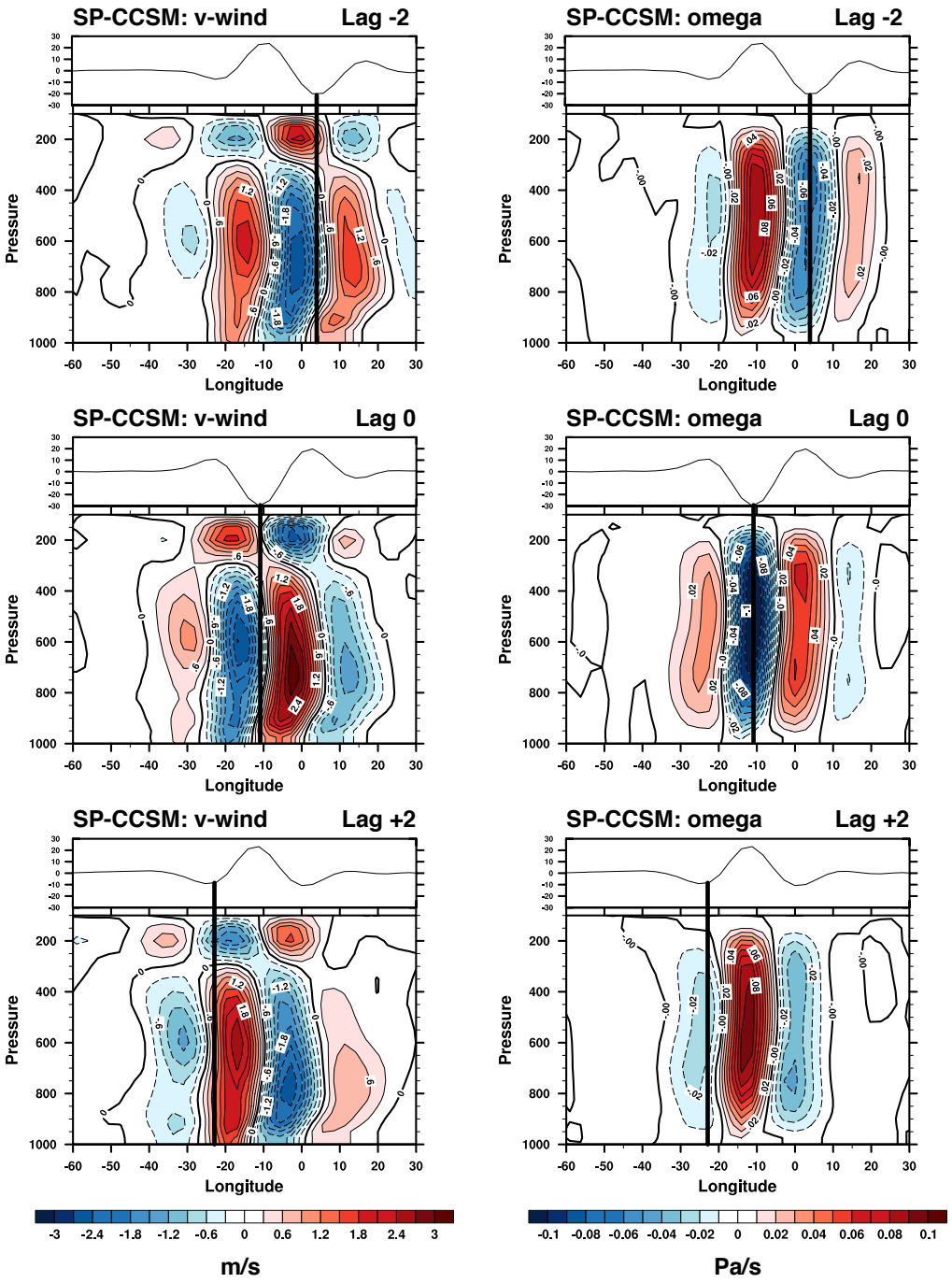


Figure 4.11. Same as Figure 9, except for SP-CCSM

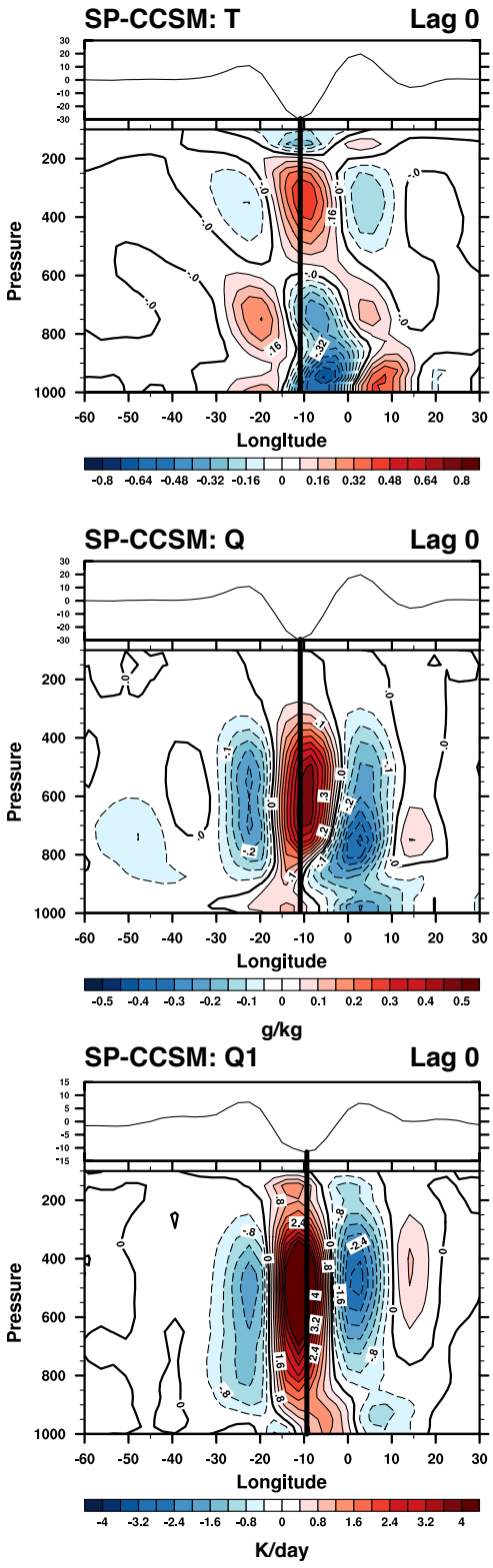


Figure 4.12. Same as Figure 10, except for SP-CCSM

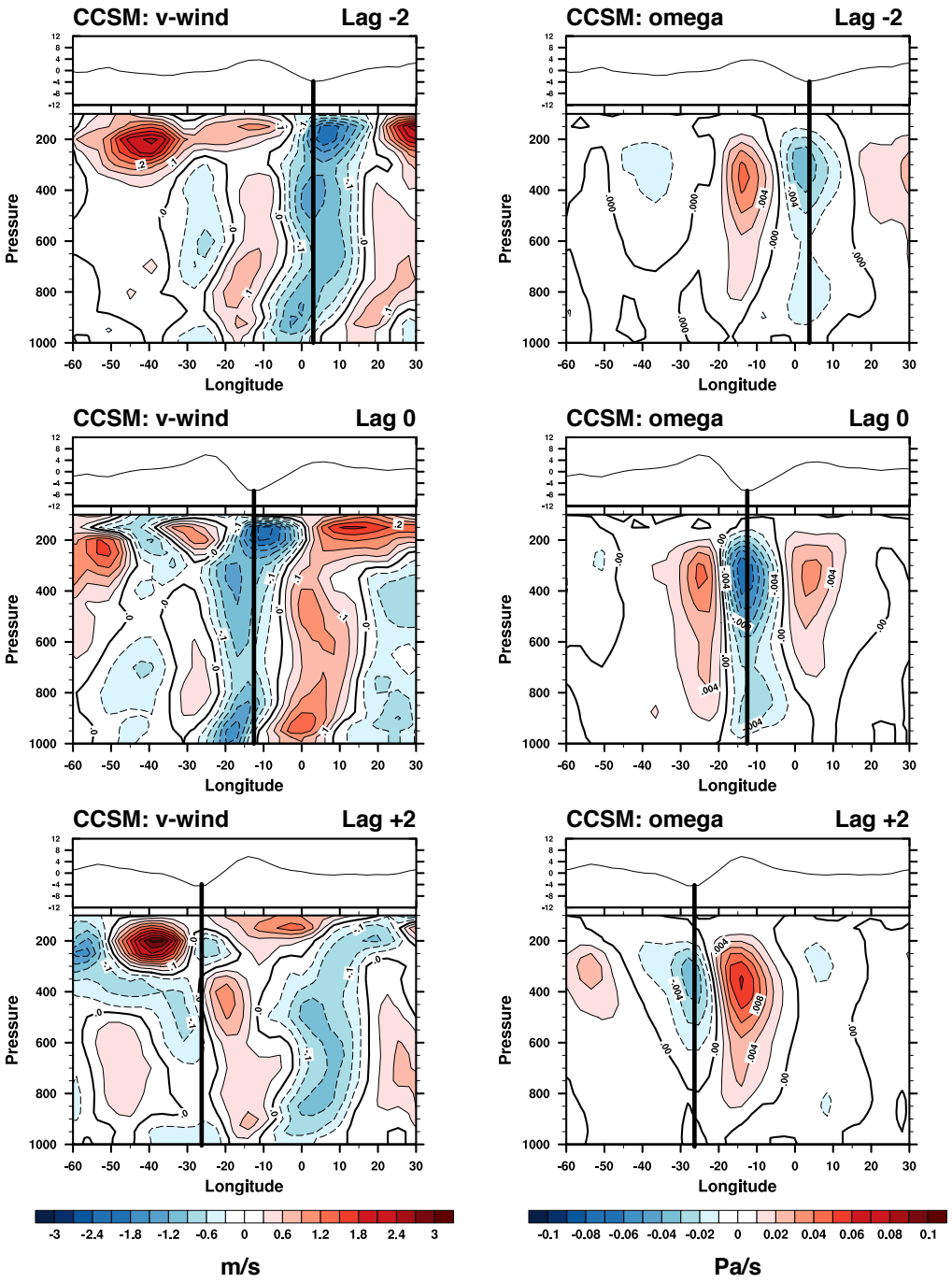


Figure 4.13. Same as Figure 9, except for CCSM.

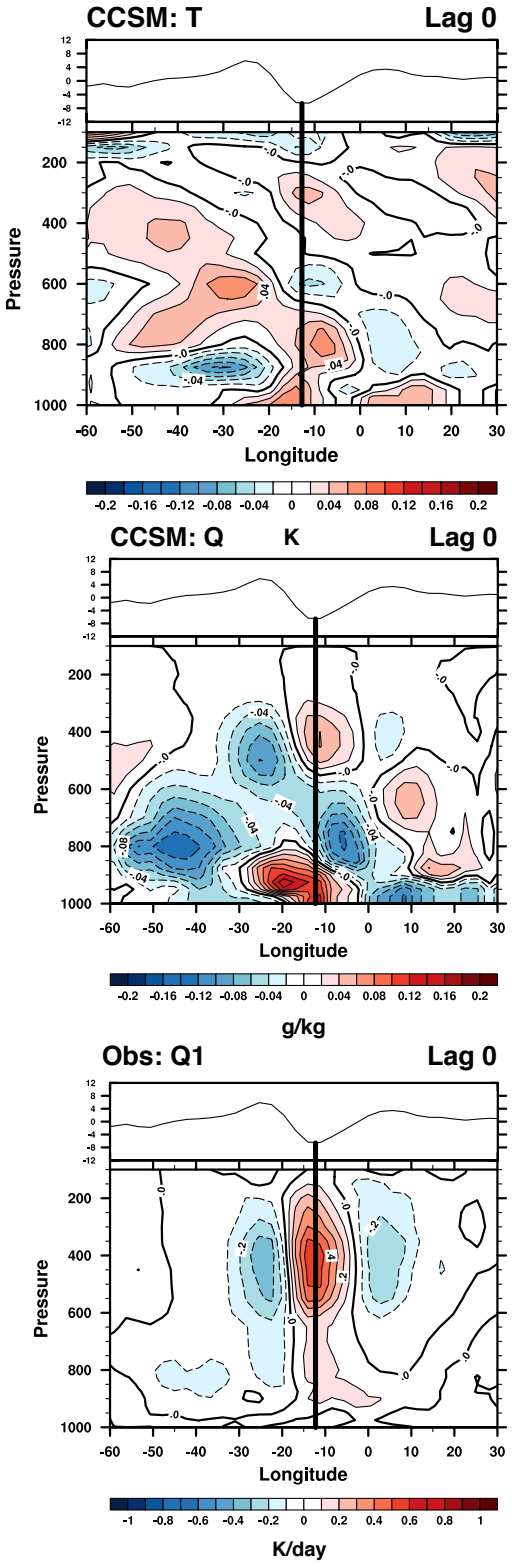


Figure 4.14. Same as Figure 10, except for CCSM.

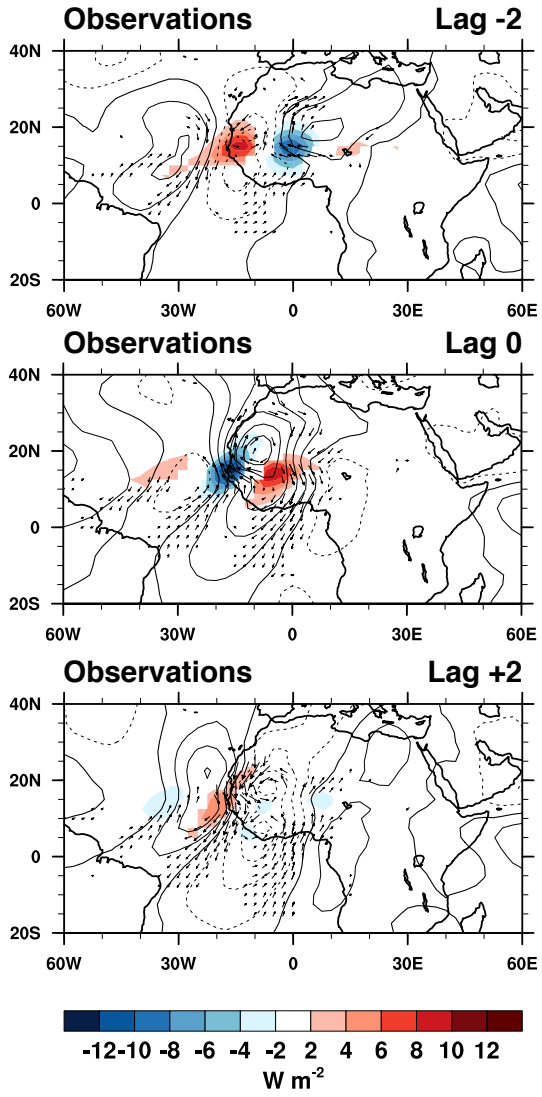


Figure 4.15. Horizontal structure of AEWs at the basepoint 15ºN,17.5ºW from observations at lag ±2 days. Anomalous OLR and 850 hPa circulation associated with a one standard deviation (-10.559) deviation of the TD-filtered OLR time series at 10ºN,10ºW. Filled contours are anomalies OLR in units of Wm^{-2}. Line contours are the 850 hPa stream function in contoured from $1x10^5$ m^2s^{-1}. Vectors are the 850 hPa winds. Only statistically significant OLR and wind vectors at the 95% confidence level are shown.

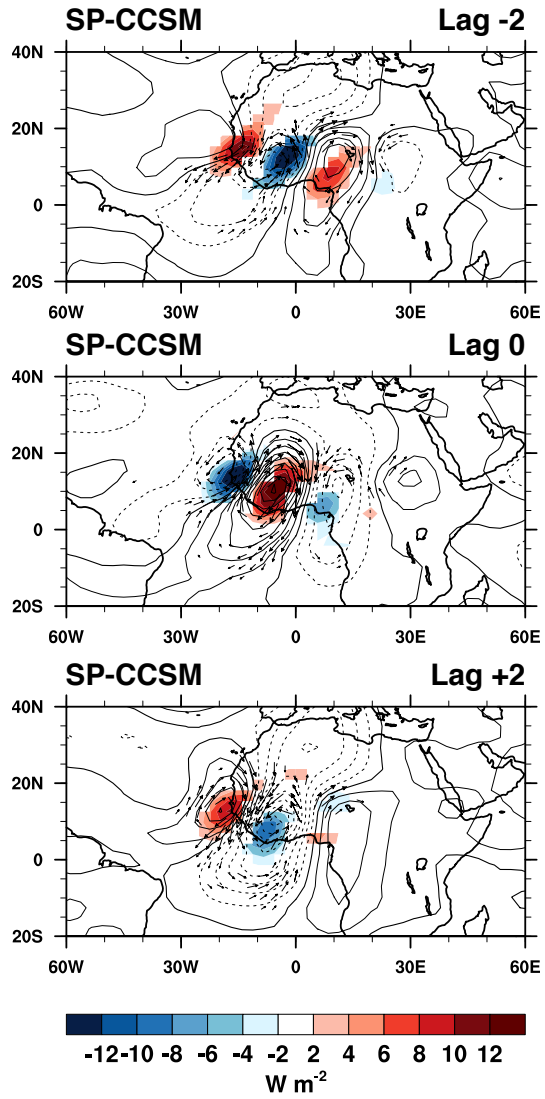


Figure 4.16. Same as Figure 15, except for SP-CCSM. Here the one standard deviation of the TD-filtered OLR time series is -10.927.

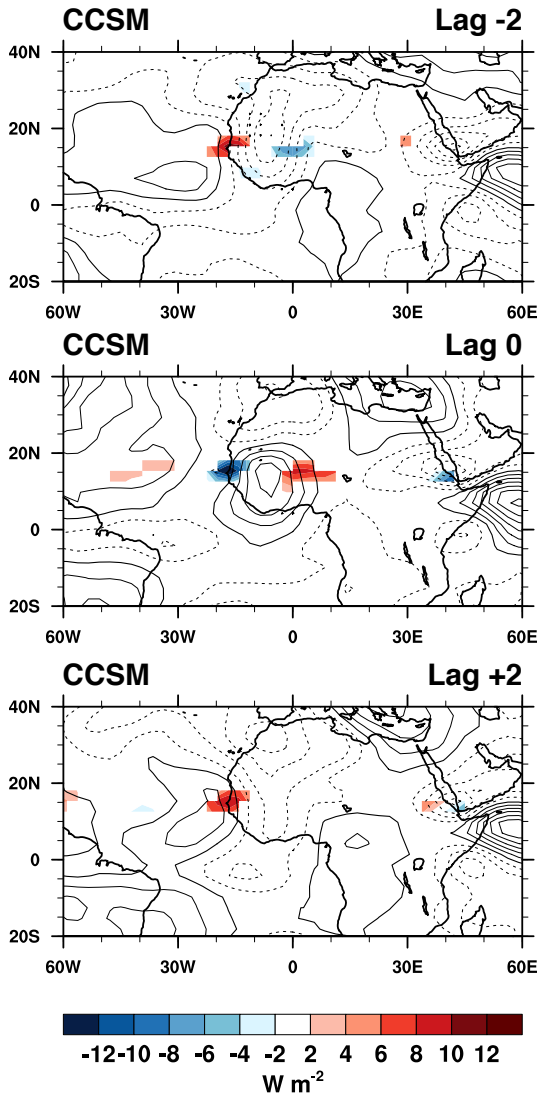


Figure 4.17 Same as Figure 15, except for CCSM. Here the one standard deviation of the TD-filtered OLR time series is -6.272.

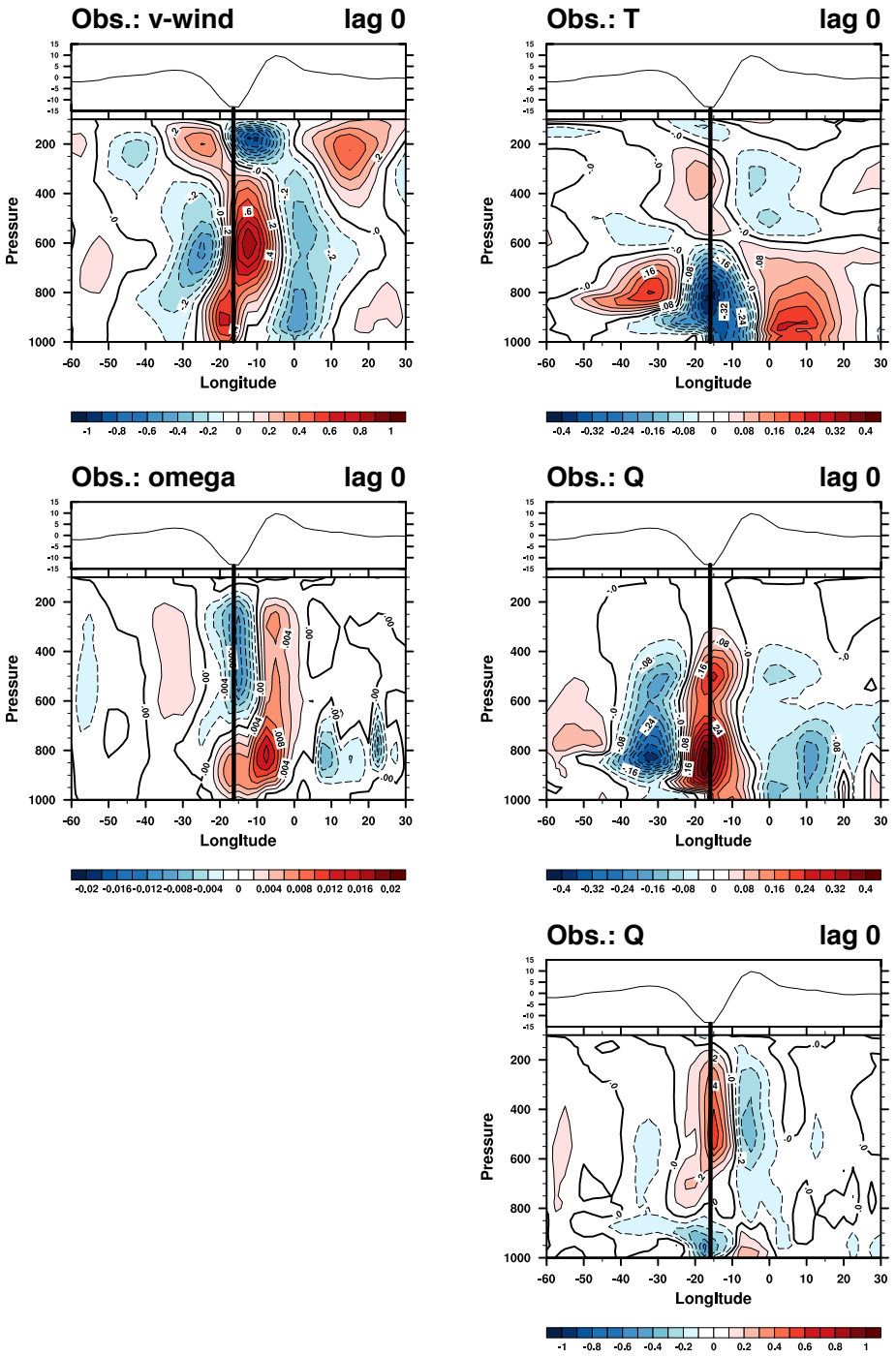


Figure 4.18. Zonal-height cross section of anomalous observed meridional wind, omega, temperature (top) and specific humidity (middle) and the apparent heat source (Q1, bottom) along 15ºN associated with the pattern in Figure 16 at lag 0. Units of wind are in m s^{-1}, omega is in Pa s^{-1} temperature are in K, specific humidity is in g kg^{-1}. and Q1 is in K day^{-1}. The associated OLR anomaly along 10ºN at each lag is shown above each panel. The position of peak convection is highlighted with the thick black line.

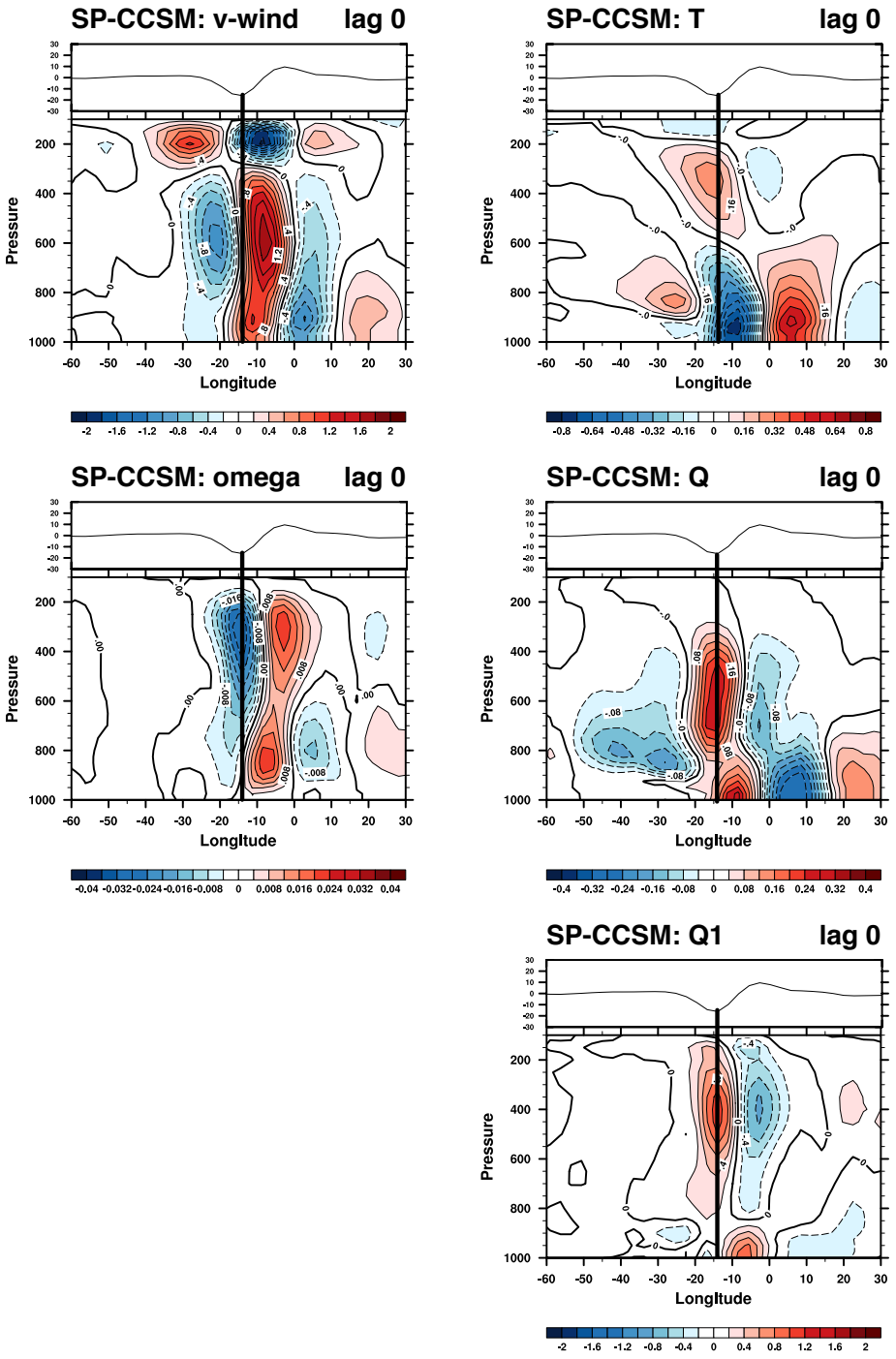


Figure 4.19. Same as Figure 18, except for SP-CCSM

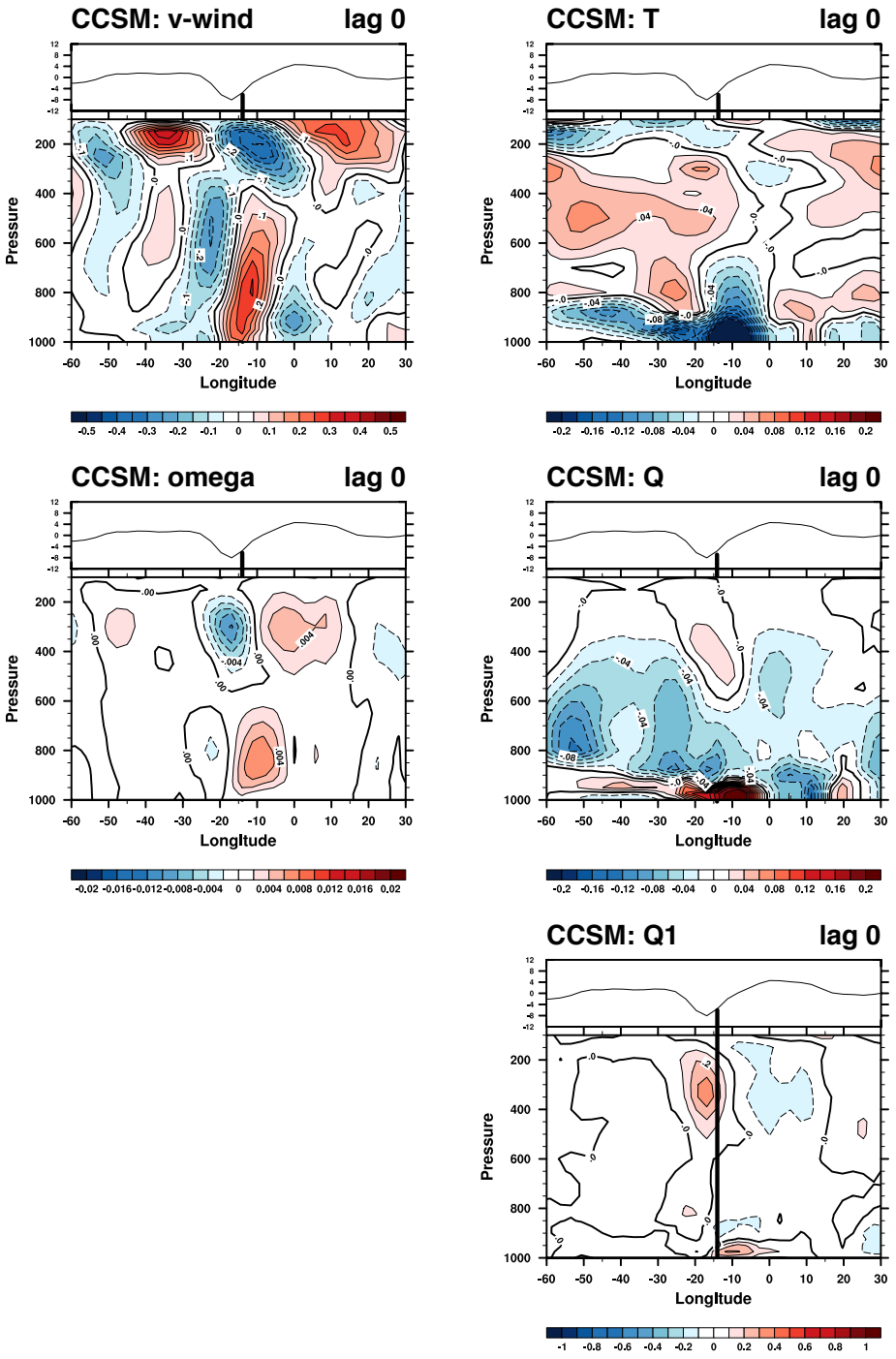


Figure 4.20. Same as Figure 18, except for CCSM.

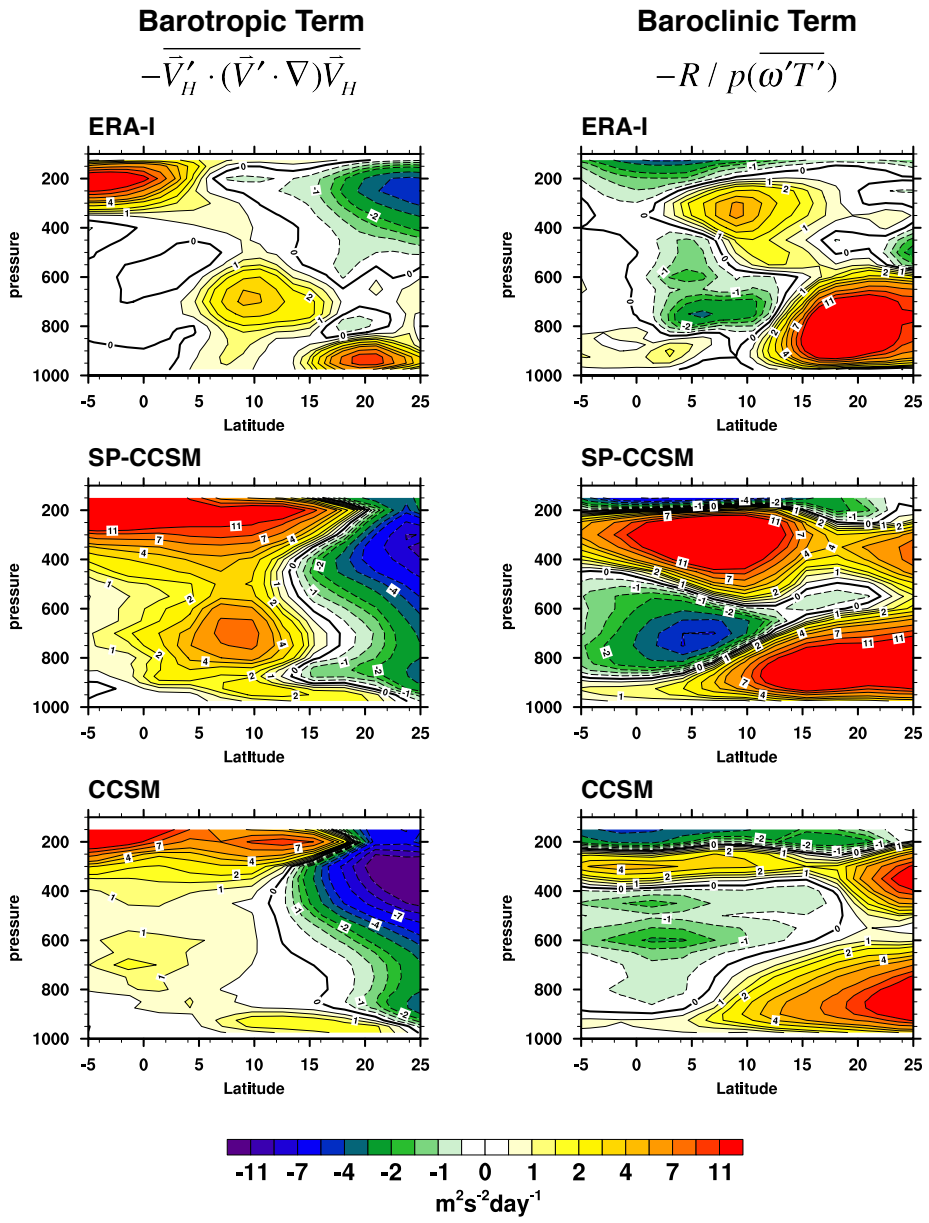


Figure 4.21. Meridional-height cross sections of the barotropic (right) and baroclinic (left) conversions to eddy kinetic energy averaged between 20ºW and 20ºE from a) ERA-I, b) SP-CCSM and c) CCSM. Units are in $m^2s^{-2}day^{-1}$.

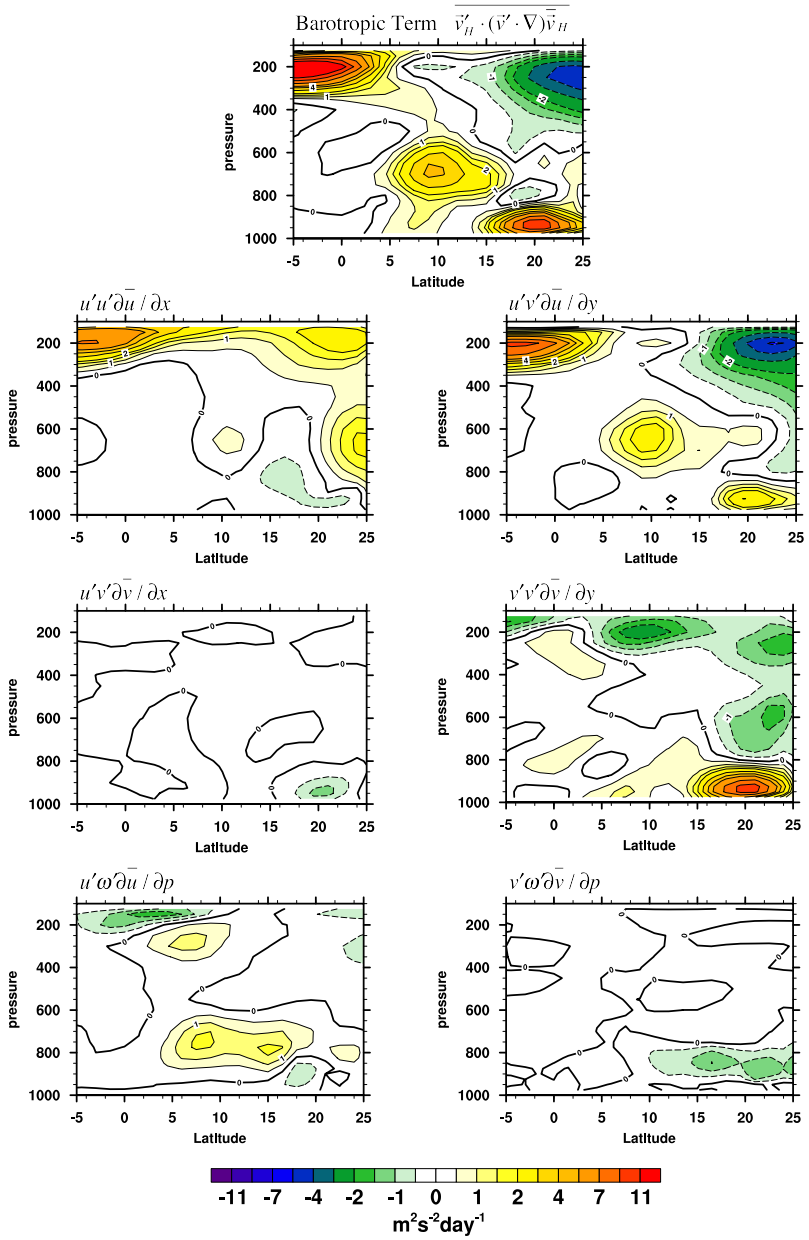


Figure 4.22. Meridional-height cross sections of the six components of the barotropic term from ERA-I. Units are in $m^2s^{-2}day^{-1}$.

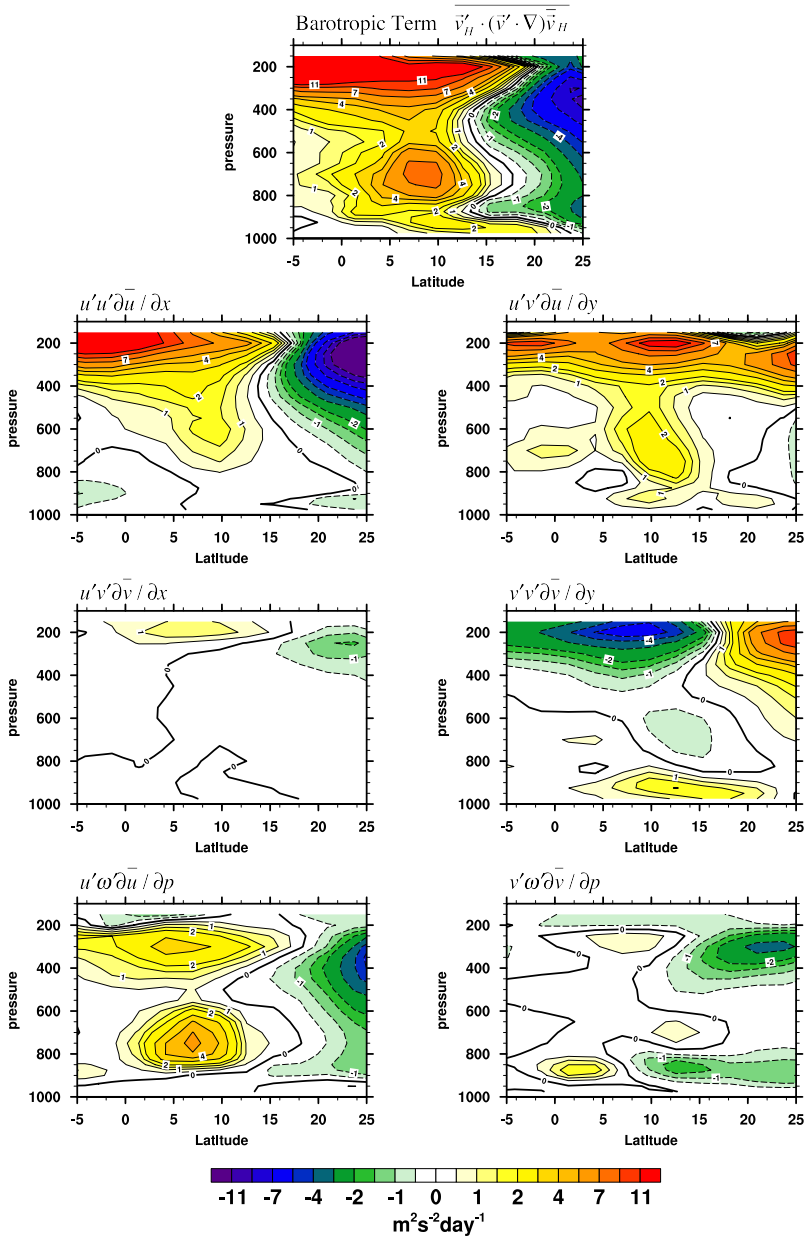


Figure 4.23. Meridional-height cross sections of the six components of the barotropic term from SP-CCSM. Units are in $m^2s^{-2}day^{-1}$.

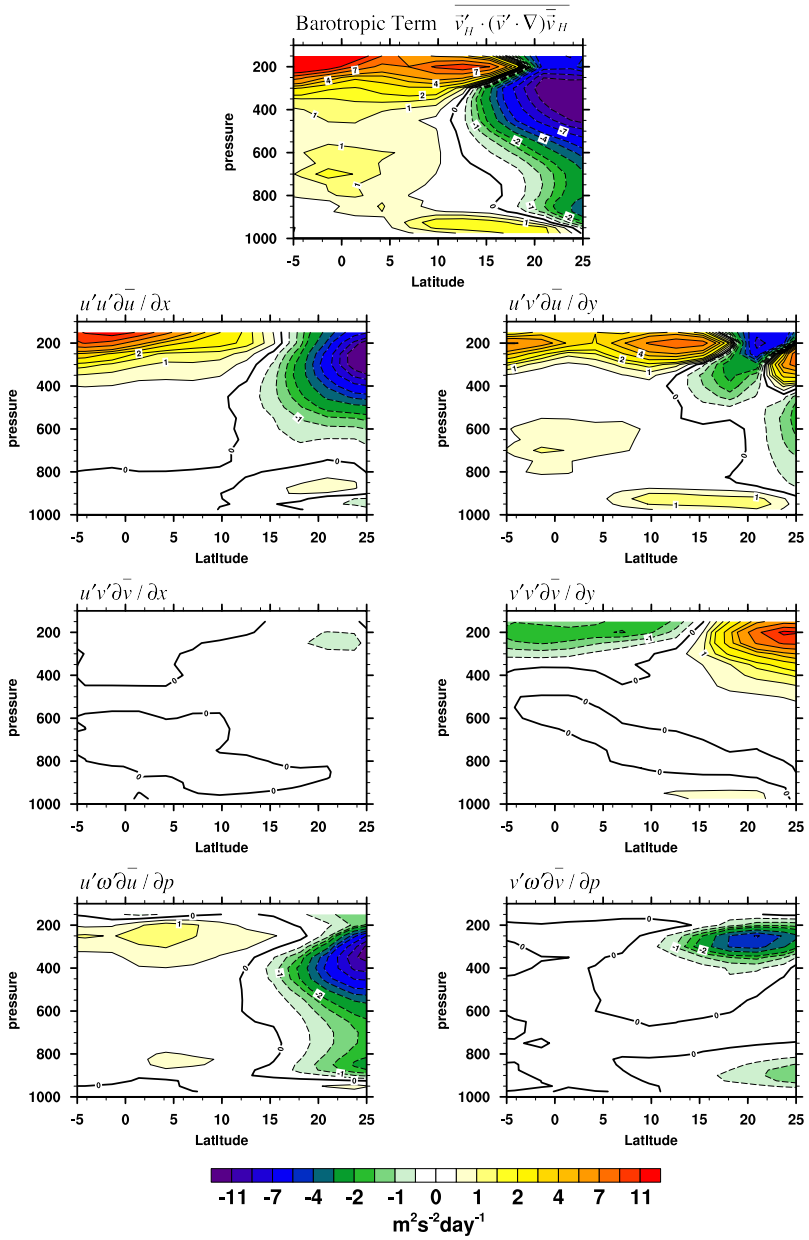


Figure 4.24. Meridional-height cross sections of the six components of the barotropic term from CCSM. Units are in $m^2s^{-2}day^{-1}$.

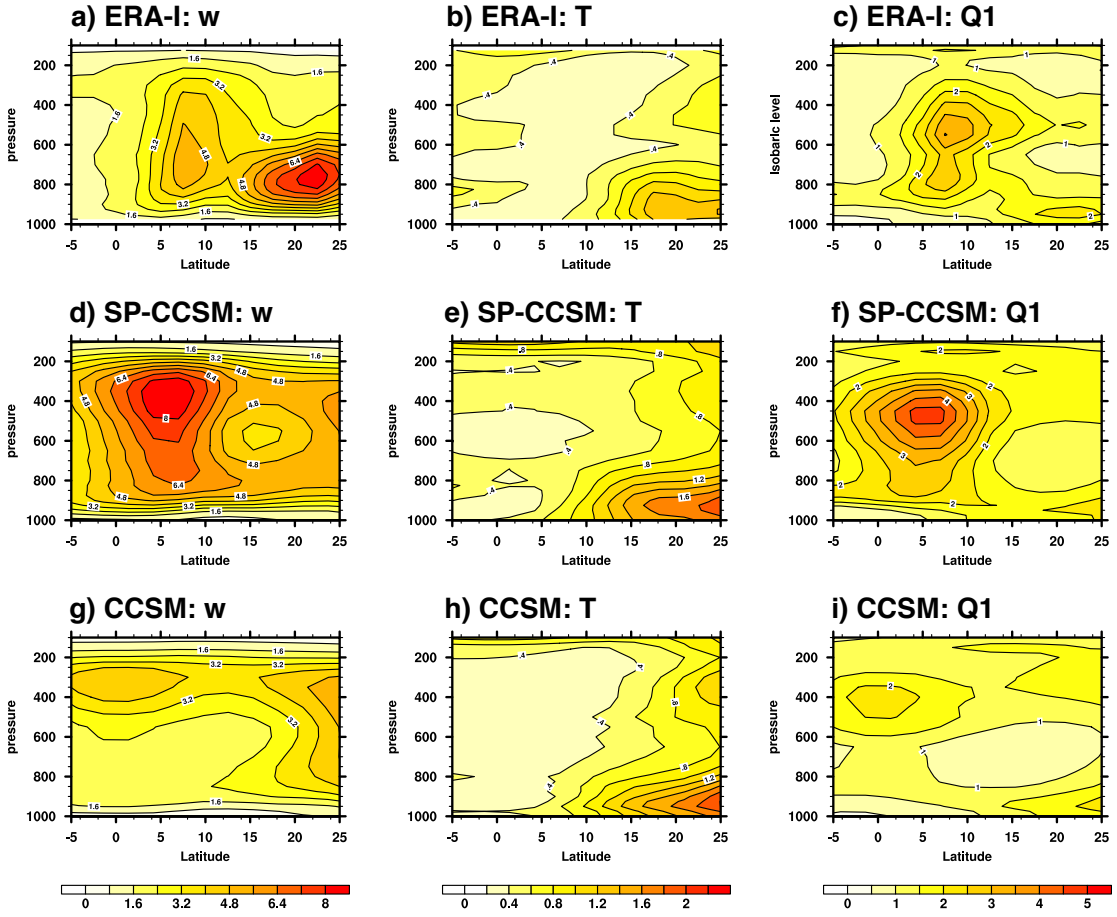


Figure 4.25. Meridional cross sections of the square root of the variance of vertical velocity (left), temperature (middle) and Q1 (right).

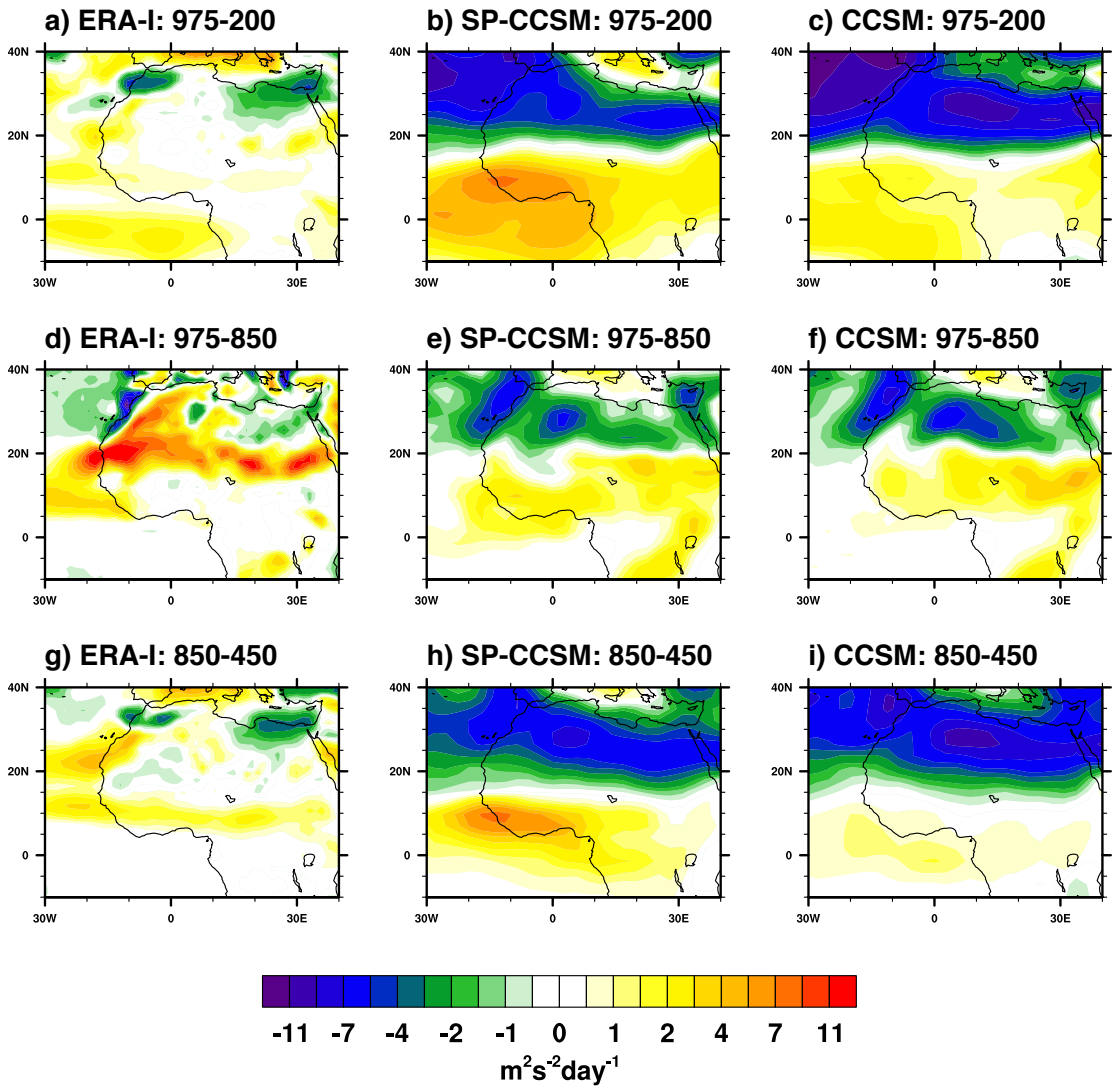


Figure 4.26. Vertical averages of the barotropic term from ERA-I, SP-CCSM and CCSM over different layers of the atmosphere. (Top) 975-200 hPa, (middle) 975-850 hPa, (bottom) 850-450 hPa.

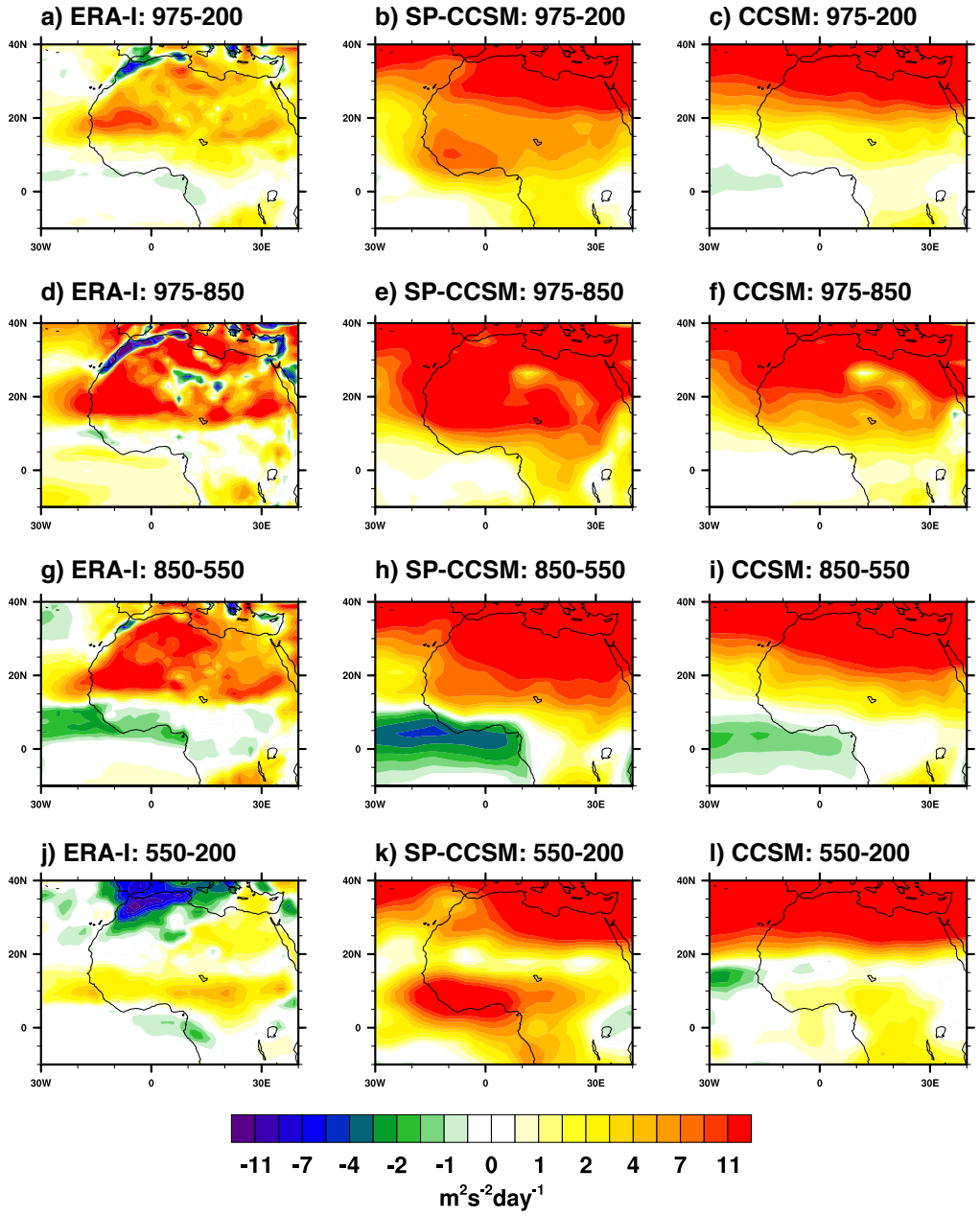


Figure 4.27. Vertical averages of the baroclinic term from ERA-I, SP-CCSM and CCSM over different layers of the atmosphere. (Top) 975-200 hPa, (2nd row) 975-850 hPa, (3rd row) 850-550 hPa, (4th row) 550-200 hPa.

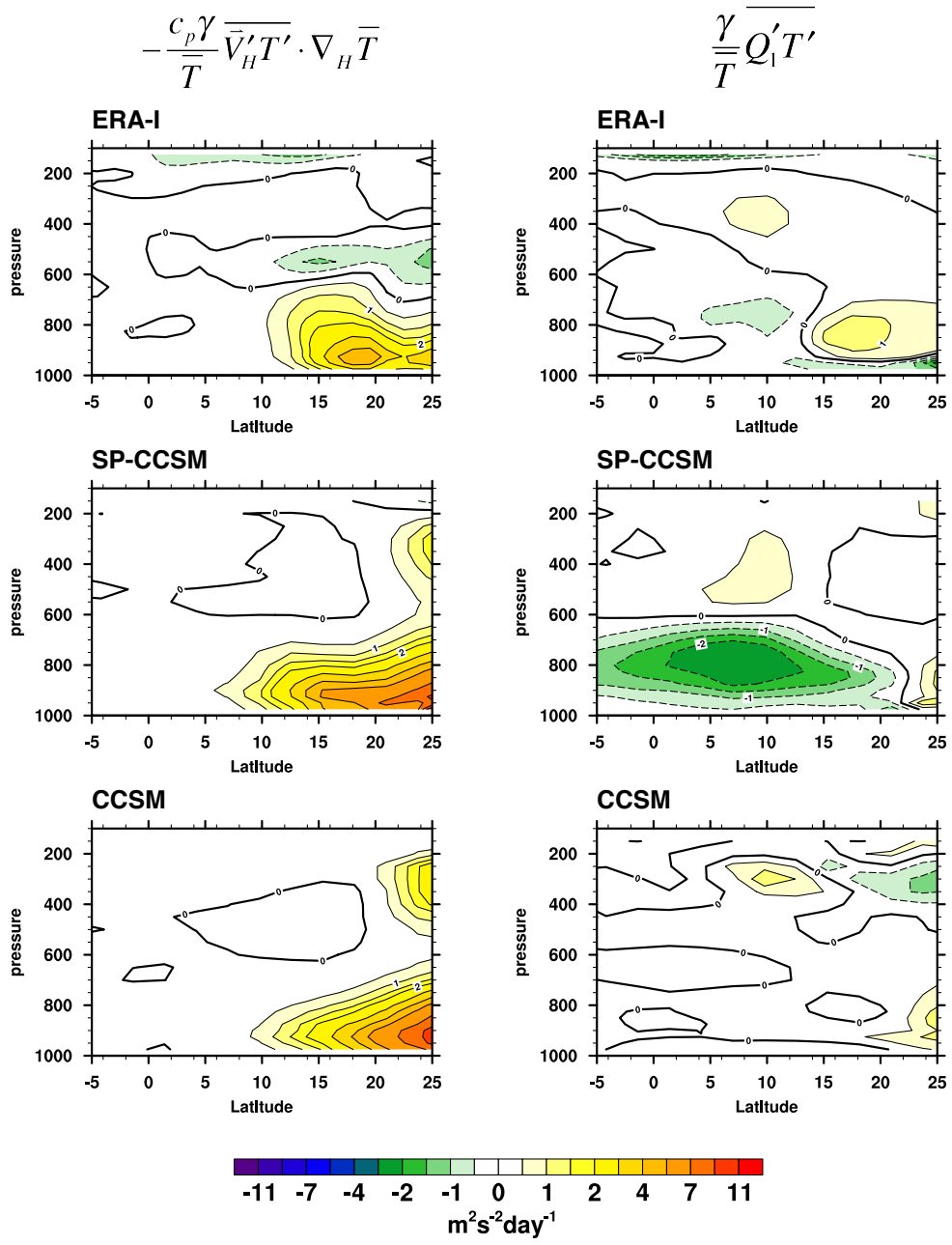


Figure 4.28. Meridional cross sections of the $-\frac{c_p\gamma}{\overline{T}}\overline{\bar{V}_H'T'}\cdot\nabla_H\overline{T}$ (left) and $+\frac{\gamma\overline{Q_1'T'}}{\overline{T}}$ (right) terms from the eddy avaialbe potential energy tendency equation.

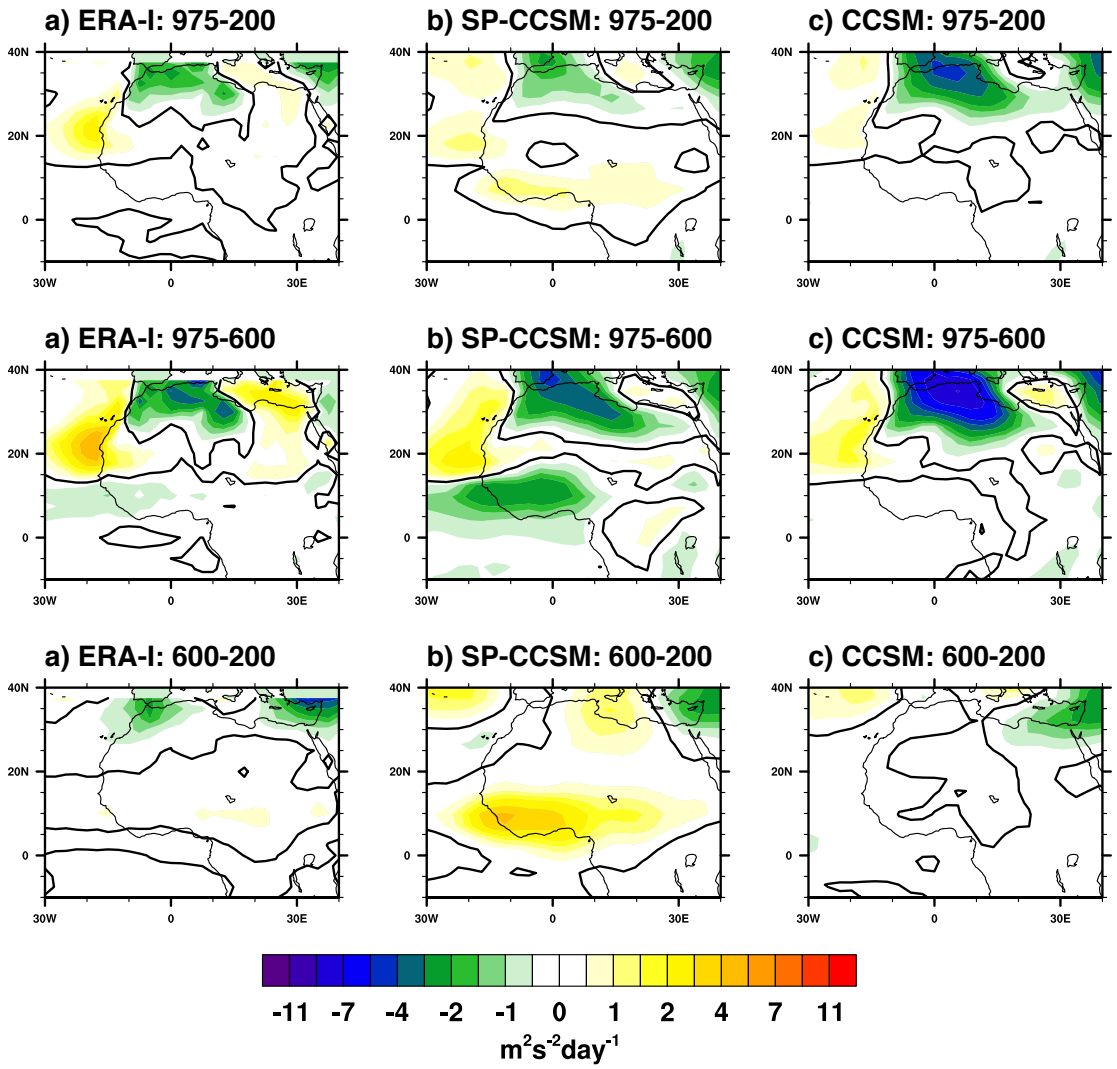


Figure 4.29. Vertical averages of the diabatic heating term in the eddy available potential energy equation from from ERA-I, SP-CCSM and CCSM over different layers of the atmosphere. (Top) 975-200 hPa, (middle) 975-600 hPa, (bottom) 600-200 hPa.

CHAPTER 5

INTRASEASONAL VARIABILITY

5.1 INTRODUCTION

The previous chapters of this dissertation have examined the ability of the models to capture the mean seasonal cycle of the monsoon as well as the characteristics of synoptic scale variability. Both of these features are important for testing the overall fidelity of the climate models. What the people of West Africa really want to know is - when will it rain and how much will it rain? As discussed in the introduction to this dissertation, monsoon rainfall is critically important for the overall agricultural health of West Africa. Knowing when seasonal rains will begin determines what crops will be planted and when. The onset of the rainy season also determines where geographically meningitis vaccines need to be distributed.

Throughout each individual monsoon season, West Africa experiences periods of prolonged wet and dry events (Janicot and Sultan, 2001). These events are devastating for water resources and crop yields and significant effort has been made in the past ten years to try to understand the mechanisms that cause these intraseasonal variations in precipitation. The hope is to identify the processes that influence precipitation variability in order to better improve seasonal rainfall predictions (Janicot et al., 2011).

Previous observational studies have found that on intraseasonal time scales the variability in precipitation over West Africa falls within two frequency bands, one that has a period of 10-25 days and a second that falls within the 25-90 day band. The shorter of these two periods has

been found to be associated two modes of variability - the quasi-biweekly zonal dipole mode (Mounier et al. 2008) and the Sahel mode (Sultan et al. 2003; Janicot et al. 2010). The mechanisms that produce these two modes are still unclear, however they have been linked to changes in moisture advection into the Sahel (Mounier et al., 2008), land-atmosphere-radiation feedbacks (Taylor et al., 2011) as well as westward moving convectively coupled Rossby waves (Janicot et al. 2010). The longer (25-90 day) intraseasonal timescale variability is thought to be forced by the MJO (Matthews, 2004; Maloney and Shaman, 2008; Alaka and Maloney, 2012) and its associated influence on the intraseasonal variability of the Asian summer monsoon (Janicot et al. 2009, 2011).

The exact mechanisms by which the MJO may force precipitation variability over West Africa are still being investigated, but current theories suggest that suppressed convection associated with the MJO over the Indian sector initiates dry westward moving Kelvin waves and eastward moving Rossby waves that converge approximately 20 days later over Africa, enhancing convection (Matthews, 2004). Given the importance of westward moving convection over West Africa, it is likely that the westward moving Rossby wave signal is dominant (Lavender and Matthews, 2009). There is also some evidence to suggest that MJO teleconnections may influence West African precipitation by modulating convection in the Darfur Mountains and the Ethiopian Highlands which results in enhanced or suppressed AEW activity (Alaka and Maloney, 2012).

Given that the super-parameterization has been shown to improve the representation of the MJO (Stan et al., 2009), the Asian summer monsoon (DeMott et al., 2011) and the West African monsoon (Chapter 3), It is of interest to see if intraseasonal variability in the West

African Monsoon in the SP-CCSM is linked to the global-scale variability of the MJO. It is important to keep in mind that traditional general circulation models that are used for seasonal precipitation forecasts have difficulty representing both the West African monsoon as well as the MJO. If the SP-CCSM does capture the teleconnections between the MJO and the West African monsoon, it might help provide insights needed to improve seasonal forecasts in models. The overall variability in the CCSM is very low, and will not be examined in this chapter.

Section 2 of this chapter describes the datasets used in this analysis. Section 3 identifies the spatial patterns associated with intraseasonal precipitation variability of the monsoon as well the spectral characteristics of West African precipitation. Section 4 describes the spatial structure of how monsoon precipitation, the African easterly jet (AEJ) and African Easterly Waves (AEW) anomalies vary on MJO timescales (30-90 days). Section 5 investigates evidence that teleconnections associated with the MJO or the Asian summer monsoon might influence intraseasonal variability over West Africa.

5.2 VARIABILITY OF WEST AFRICAN MONSOON PRECIPITATION

In this section the spatial characteristics associated with intraseasonal precipitation variability are identified. Also, spectral peaks in rainfall are investigated.

5.2.a Mean and Variance Fields

The spatial patterns of mean May-October precipitation from TRMM and SP-CCSM are shown in Figure 5.1. While the seasonal cycle of precipitation was investigated more thoroughly in Chapter 3, here we revisit the mean precipitation in order to better highlight the patterns of variability that are the main points of this chapter. During the observed monsoon the ITCZ transitions onto the continent, with the main band of precipitation extending up to ~18ºN.

Maxima in precipitation are found over the Ethiopian highlands, near Cameroon, and just off the west coast extending into the Atlantic intertropical convergence zone (ITCZ). These regions of enhanced rainfall correspond with local topography, and the drying between the two maxima along the coast is thought to be associated SSTs and the Atlantic cold tongue. In SP-CCSM, the ITCZ also extends onto the continent although in the case of the model there is only one zonally elongated maximum in precipitation. This maximum extends from the Bight of Bonny out into the Atlantic. There is no drying between Cameroon and the Guinea highlands and the Atlantic ITCZ does not extend as far westward as is observed.

Figure 5.2 shows the total variance in precipitation over West Africa between May-October. The total variance is calculated by removing the smoothed seasonal cycle. The smoothed seasonal cycle is constructed in a manner similar to Maloney and Shaman (2008), where data is averaged for each calendar day for the entire time record, then smoothed using six passes of a 1-2-1 running filter. The smoothed seasonal cycle is then removed from the raw precipitation fields. The greatest variability in both the observations and SP-CCSM corresponds with the regions where the largest seasonal rainfall totals occurs. In the observations the greatest variability is found near Cameroon and over the Bight of Bonny, and along the west coast extending into the Atlantic ITCZ. In SP-CCSM, the largest variance occurs along the coast of the Gulf of Guinea extending into the Atlantic.

To determine the time-scales associated with the variability found in precipitation during the monsoon, I apply two different filters. A less than 10 day high-pass filter is used to broadly identify synoptic scale variability in precipitation (Figure 5.3 left). This variability will be predominately due to AEWs, however this filter does not separate between “wave” and “no-

wave" conditions. Intraseasonal variability is then identified using a 10-120 day band-pass filter (Figure 5.4 left). The relative contribution of each of these time scales of variability to the total precipitation variability is highlighted by showing maps of the ratio of synoptic to total variance (Figure 5.3 right) and intraseasonal to total variance (Figure 5.4 right).

In both the observations and SP-CCSM, more than 80% of the total variability in precipitation over West Africa occurs on synoptic time scales. A much smaller percentage of the variability is due to longer intraseasonal variations in precipitation (<15%). Along the Guinea coast and in the Atlantic ITCZ, intraseasonal timescales are of greater importance. Outside of the ITCZ and the primary rain bands, intraseasonal variations account for a greater percentage of the total variability, but rainfall amounts in these regions are low to begin with. While the percentage of total variance in precipitation that can be explained by intraseasonal variability is much less than synoptic variability, it is likely that the mechanisms that induce modes of intraseasonal variability will subsequently modulate synoptic scale precipitation.

For example, in the observations, both synoptic and intraseasonal variations in precipitation are also found over the Darfur Mountains and the Ethiopian Highlands. This region east of Lake Chad is thought to be important for triggering AEWs. As discussed in chapter 4, AEWs are important for organizing precipitation over West Africa and influence total rainfall amounts during the monsoon season. AEWs have been observed to exhibit significant intraseasonal variability during the monsoon season (Leroux et al., 2010), and it is possible that the intraseasonal variability in rainfall over this region is important for AEW variability. This is the case of intraseasonal variability modulating synoptic scale precipitation.

Now that the spatial characteristics of intraseasonal variability have been identified, it is important to determine which frequency bands, if any, exhibit statistically significant power that is distinguishable from noise.

5.2.b Power Spectra

As mentioned in the introduction, previous studies have found that on intraseasonal timescales precipitation over West Africa during boreal summer is dominated by variability on both 10-25 day timescales and 30-90 day timescales. To determine the spectral characteristics of monsoon precipitation in the SP-CCSM and identify significant periods we calculate the May-October power-spectra over two areas: the region 0º-15ºN, 30ºW-20ºE, which encompasses the area with the largest intraseasonal precipitation variability (Figure 5.5 top), and the region 0º-15ºN and 30º-40ºE, which covers the area east of Lake Chad (Figure 5.5 bottom).

To calculate the spectra, first the smoothed seasonal cycle was removed from each time series. The data was then subdivided into the individual May-October time periods from each year. The first and last 5% of each May-October time series was tapered using a cosine bell function to reduce spurious results in the frequency response function. The spectra were calculated for each individual year, and then averaged across all of the years (13 for TRMM, 26 for SP-CCSM). To maximize the degrees of freedom a 3-point Daniell smoother (Daniell, 1946) was applied to the individual spectra. Red noise and 95% confidence limits were determined using the theoretical Markov spectrum methods. Spectral peaks that are statistically significant at the 95% confidence level will stand above the upper limit of these curves.

In the observations, the spectra from both regions show significant peaks at approximately 50 days. As has been pointed out in previous studies (Maloney and Shaman,

2008; Janicot (2001, 2003, 2011) this peak has been shown to correspond with the MJO and active-breaking phases of the Asian monsoon. In the spectra shown here a second, but not statistically significant peak is also found at approximately 15 days. Other studies have emphasized the importance of 10-25-day variability in monsoon precipitation, however for the time period of the dataset used here and the area we are examining, this peak does not seem to be significant and we will not focus on it in this chapter. In both spectral curves from the observations, significant spectral power also stands out at periods of 3-5 days, this is presumably due to AEWs and synoptic variability.

The spectra for SP-CCSM show that significant power occurs at +50 days and 3-5 days, but is not the seasonal cycle. Unlike the observations, where a clear peak at 50 days is found, in SP-CCSM significant power continues beyond the 50 day marker. This may be an indication that lower-frequency variability is important for modulating the monsoon in SP-CCSM.

Given the work done in other observational and modeling studies that points to MJO as an important modulator of intraseasonal variability over West Africa (Matthews, 2004; Maloney and Shaman, 2008), for the remainder of this chapter we will concentrate on the variability in West African monsoon precipitation that corresponds with the 50 day spectral peak. In particular we will emphasize the variations in the monsoon that occur on 30-90 day timescales, the same time period as the MJO.

5.2.c Relationship with the Global MJO Signature

Following Maloney and Shaman (2008) I derive an index for the 30-90 day variations in West African monsoon precipitation. This index is calculated by applying a 30-90-day bandpass

filter to precipitation and then averaging over the area 0º-15ºN, 30ºW-20ºE. I then compare this regional time series to a index that characterizes the global evolution of the MJO.

To calculate the MJO timeseries, the first two EOFs of 30-90-day band-pass filtered zonal wind at 850hPa along the equator (5ºS-5ºN) are computed. As shown in Maloney and Hartmann (1998) and Maloney and Esbensen (2007) the first two EOFs are a quadrature pair, with the principal component corresponding to the second EOF (PC2) lagging behind PC1 by 12 days (10 days in SP-CCSM). The global MJO timeseries is then computed by adding PC1 to the value of PC2 12 days later.

Next the regional 30-90-day precipitation time series from Africa is correlated with the derived global MJO index as a function of lag day. From Figure 5.6 we see that in observations the maximum correlation between the MJO index and precipitation over Africa is 0.58 and occurs when the the MJO leads the precipitation time series by about 10 days. Although correlations are weaker between the MJO and precipitation over Africa in SP-CCSM, the maximum correlation between the two occurs when the MJO leads the precipitation time series by about 20-days. This may be one indication the teleconnections between the MJO and Africa propagate more slowly in the model compared to observations. As mentioned by Maloney and Shaman (2008), the MJO index calculated here corresponds with oscillations in the low-level wind field. Positive correlations indicate that the dynamical response to convection in Indian sector is correlated with precipitation changes over West Africa 10-20 days later.

5.3 SPATIAL-STRUCTURE OF 30-90 DAY VARIABILITY

The next step is to characterize the spatial patterns associated with positive and negative phases of the 30-90-day variations in precipitation over West Africa. I would like to note that

similar results can be found using EOF analysis techniques (e.g., Matthews, 2004) but I feel the methods used here are simpler, more straight forward, and more robust. Extreme positive (wet) and negative (dry) phases of the monsoon can be identified using the 30-90-day regional precipitation index. In this index, extreme events are those that exceed one standard deviation of the 30-90 day precipitation time series. Composite maps of precipitation, 925hPa winds, 600hPa zonal wind, and 700hPa EKE, based on these extreme events then created.

Figure 5.7 shows the anomalous precipitation and 925hPa wind patterns associated with the positive and negative events. Positive (negative) events are characterized by enhancement (suppression) of convection within the 5º-10ºN latitudinal band extending from 35ºE to 35ºW. The largest precipitation anomalies occur in the Gulf of Guinea and just off the coast in the Atlantic. Precipitation anomalies of opposite sign occur in the west Atlantic near South America. An examination of the first and second EOFs of 30-90 day precipitation variability show similar patterns with the first EOF representing a pulsing of enhanced (suppressed) rainfall within the ITCZ and the second EOF representing an east-west precipitation dipole (not shown). Precipitation over the Darfur mountains and the Ethiopian Highlands is also enhanced (suppressed). Low-level winds show a decrease (increase) in the trade winds associated with enhanced (suppressed) convection over the Atlantic. In the Gulf of Guinea precipitation anomalies are associated with weak anomalous convergence (divergence).

Figure 5.8 shows the anomalies in the 600hPa winds (the AEJ location) associated with the positive (negative) 30-90 day precipitation events. During positive (negative) events the AEJ shifts northward (southward). Cook et al. (1999) highlighted the importance of the AEJ for advecting moisture out of the West African region, which may help explain why a northward

shift of the AEJ during wet events might allow for increased moisture near the Guinean coast and increased precipitation. The northward shift of the AEJ may also influence the horizontal wind-shear associated with the jet, Lavender and Matthews (2009) hypothesize that this may be important for AEW activity over the area. The pattern of intraseasonal variability in the AEJ found here using composite analysis is similar to that found by Leroux et al. (2010) which used lag-regression EOF techniques to identify the north-south displacement of AEJ being important on intraseasonal timescales.

From Figure 5.9 we also see that 700 hPa eddy kinetic energy (EKE), which is a good measure of AEWs and synoptic scale activity, is increased (decreased) during positive (negative) precipitation events. Here the eddy components of the wind u' and v' are defined as the deviation from a 5-day running average and EKE is the 5-day average of $(1/2)(u'^2 + v'^2)$. As described in Chapter 4, AEW activity is important for organizing precipitation over West Africa, and it appears from this figure that AEW are modulated on 30-90 day timescales timescales (Alaka and Maloney, 2012).

The composite analysis for extreme positive and negative events in SP-CCSM displays similar characteristics to observations. As expected, positive (negative) phases of the 30-90 day precipitation index correspond with enhanced (suppressed) precipitation. Although precipitation in this case experiences a north-south dipole in the Atlantic, rather than the east west dipole found in observations. The low level winds show a similar decrease (increase) in the trade winds, corresponding with enhanced (decreased) onshore flow. The positive (negative) phases of rainfall are also associated with a northward (southward) shift of the AEJ, although in the case of the model this shift displays a unique northwest to southeast tilt. EKE and its assumed

connection to AEW activity is also enhanced (suppressed) over West Africa. While in observations, EKE also varies in North Africa as well as over the Atlantic, in the case of the model this EKE is isolated to regions where precipitation is maximized.

5.4 RELATIONSHIP WITH CONVECTION OVER THE INDO-PACIFIC

The previous section identified the spatial characteristics associated with positive and negative 30-90-day variations in West African monsoon precipitation. Here I generate composite fields over the global tropics (from 5S-30N) as a function of time lag to determine if variability in precipitation at other locations throughout the tropics might influence precipitation over west Africa. Figure 5.10 shows the time evolution of tropical precipitation from 20 days prior to the maximum in precipitation over Africa to 20 days after the maximum has passed. At lag day 0 the picture over Africa is the same as that found in Figure 5.7. In the observations we see that approximately 20 days prior to the extreme positive phase in precipitation over West Africa, convection is suppressed over the Indian ocean and the West Pacific. These negative precipitation anomalies increase in magnitude until lag day 0, when convection re-initiates over India and the West Pacific. This pattern is comparable to that found by Matthews (2004) and suggests that the suppression of convection over the Indo-Pacific region, that is associated with the MJO, is lag-correlated with enhanced precipitation over West Africa. Composite time lag maps of 850 hPa zonal wind show that ten days prior to enhanced convective activity over West Africa, anomalous easterly winds generate over the Indian ocean and across the West Pacific (Figure 5.11). These easterlies increase in amplitude and propagate northward reaching a maximum at lag +5 days where they are replaced by anomalous westerlies. This too is comparable to Matthews (2004), who suggests that dry Kelvin and Rossby waves that are

generated over the Indo-Pacific region prior to enhanced precipitation over Africa may provide the dynamical link between the weather over the West Pacific to the weather over Africa. This figure points to a dynamical link between convection in the Indo-Pacific and West Africa.

Surprisingly similar lag-time spatial structures in precipitation and 805hPa zonal winds are found in SP-CCSM. Much like the observations, enhanced precipitation over West Africa is preceded by suppressed convection (Figure 5.12) and anomalous easterlies (Figure 5.13) over the Indo-Pacific region. Curiously, while the lag-correlations shown in Section 3 suggest that the time between the MJO and the African monsoon is on the order of 20 days, Figure 5.13 suggests that the lag time may be on the scale of 10 days. It is also possible that the enhanced precipitation and anomalies westerlies found at lag -20 days are more important for precipitation over Africa in the SP-CCSM.

5.5 CONCLUSIONS

The goal of this chapter was to identify the primary modes of intraseasonal variability in precipitation for the simulated West African Monsoon in SP-CCSM. I have demonstrated that the simulated precipitation over west Africa exhibits statistically significant power at periods longer than 50 days, which is comparable to observations. The intraseasonal variations in precipitation act to amplify or suppress convection within the ITCZ along the coast of West Africa and in the Atlantic ITCZ. Unlike the observations, the SP-CCSM does not represent the maximum in convection that occurs near Cameroon so intraseasonal variability in that region is low in the model. I created an index that identifies 30-90 day variability in West African monsoon precipitation and correlated this timeseries with a global index of MJO activity based on 850hPa winds. In observations the MJO was found to lead precipitation variability over West

Africa by 10 days, while in the model this number was more like 20 days. In both the observations and the SP-CCSM, enhanced precipitation on 30-90 day timescales was found to be associated with a decrease in the trade winds resulting in enhanced onshore flow, a northward shift of the AEJ and increased EKE and AEW activity. On the global scale, in agreement with previous studies, enhanced precipitation over West Africa on intraseasonal timescales was found to be preceded by suppressed convection and anomalous easterlies over the Indo-Pacific region associated with MJO activity.

Given that the SP-CCSM is capable of representing intraseasonal variability in the West African Monsoon, the MJO as well as the Asian summer monsoon, further modeling studies that use prescribed heating anomalies in the Indo-Pacific region that are consistent with MJO forcing might be able to provide important insights into the response of MJO forcing over Africa. Perhaps a toy model similar to the one used in Hoskins et al. (1999) might be useful for examining the teleconnections between convection in the Indo-Pacific and West Africa.

5.6 FIGURES

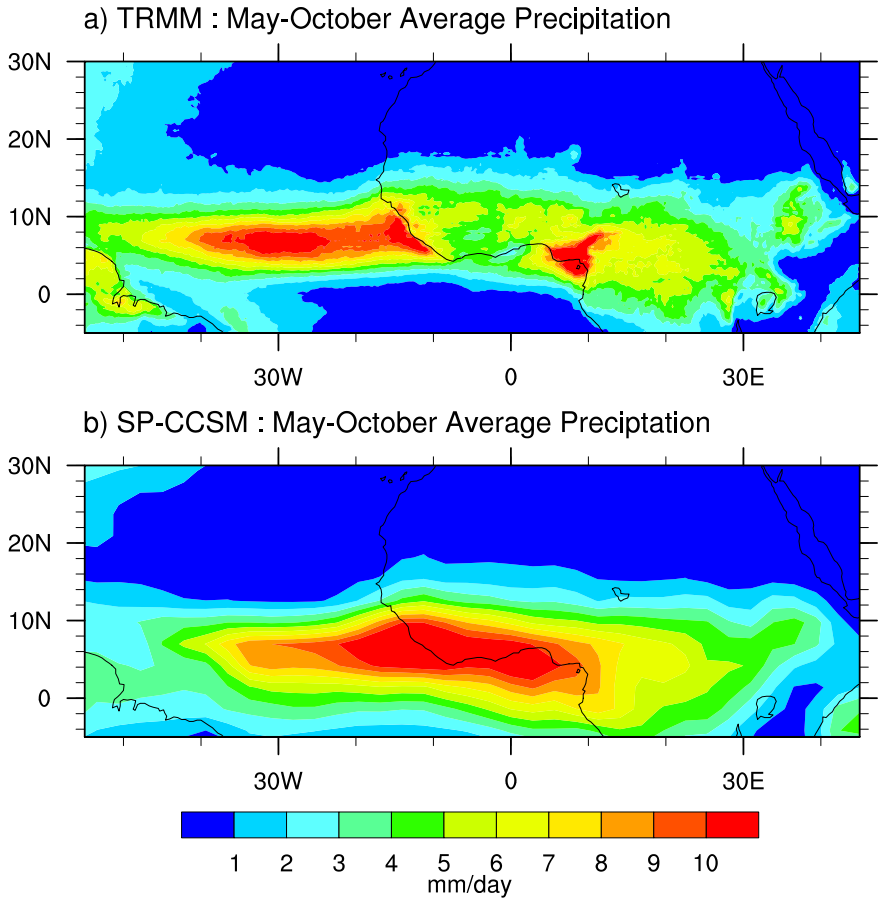


Figure 5.1. Mean May-October precipitation rate from (a) TRMM and (b) SP-CCSM. Precipitation rate is in units of mm day $^{-1}$.

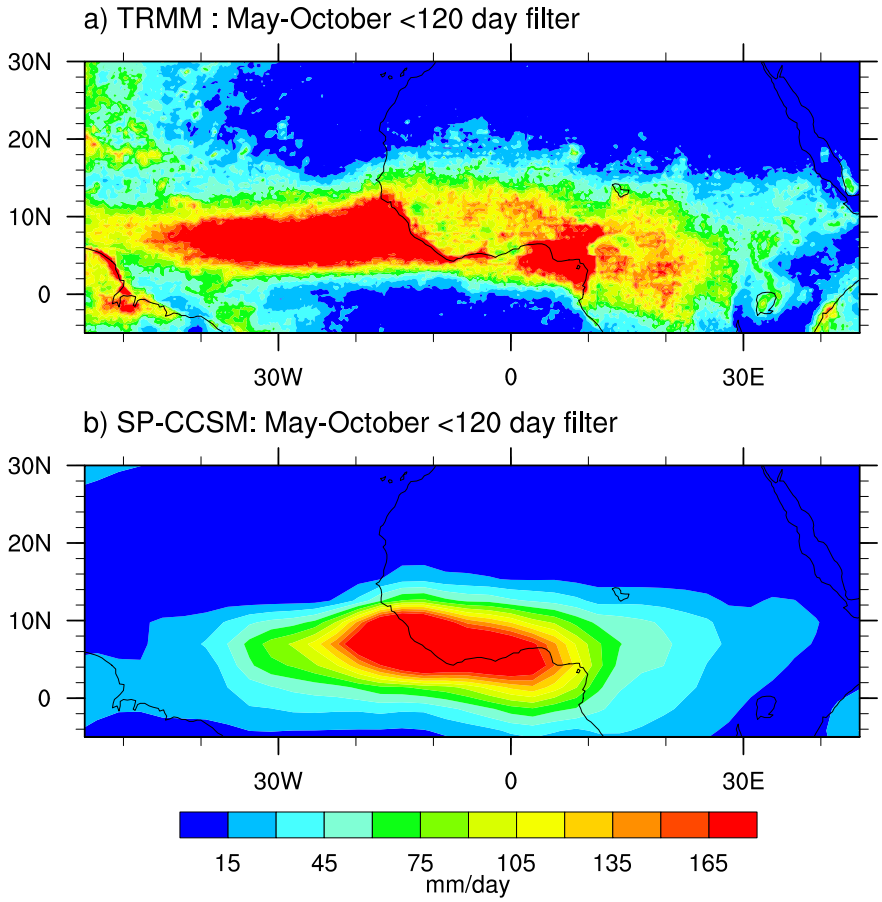


Figure 5.2. Total variance of May-October precipitation from (a) TRMM and (b) SP-CCSM. This is the square of the anomalies calculated by removing the smoothed seasonal cycle. Units are in mm $^{-2}$ day $^{-2}$.

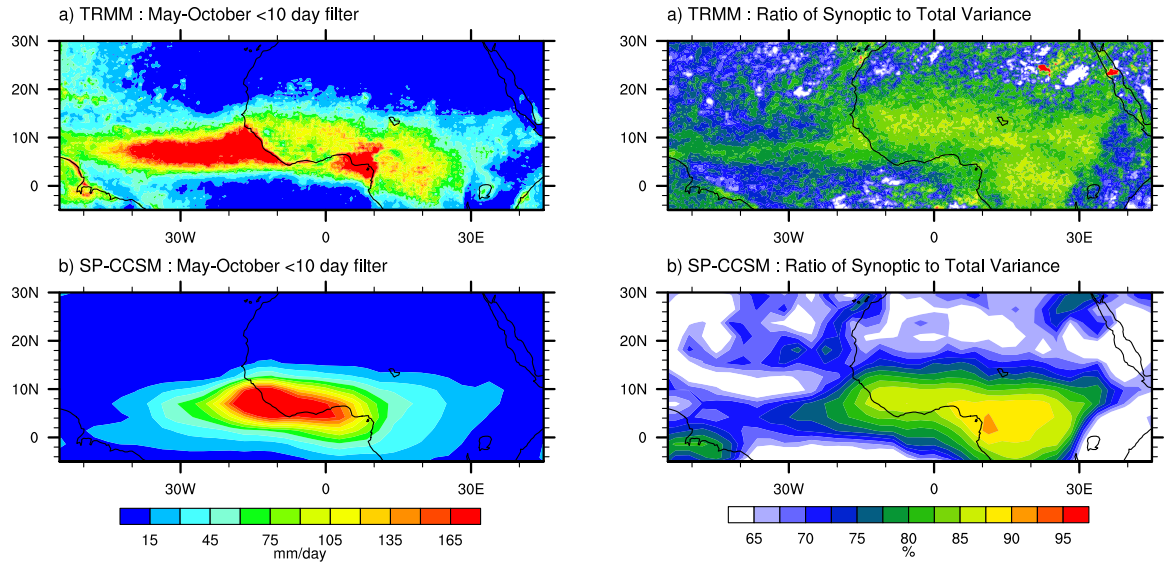


Figure 5.3. The variance of synoptic scale variability in precipitation from (a) TRMM and (b) SP-CCSM. The ratio of synoptic scale variance to total variance from (c) TRMM and (d) SP-CCSM. Synoptic scale variability is calculated by applying a high-pass filter that retains variability on timescales of less than 10 days. Variance is in mm $^{-2}$ day $^{-2}$. The ratio of the variances is shown as a percent of the total variance explained and is contoured from 60-100% by increments of 5%.

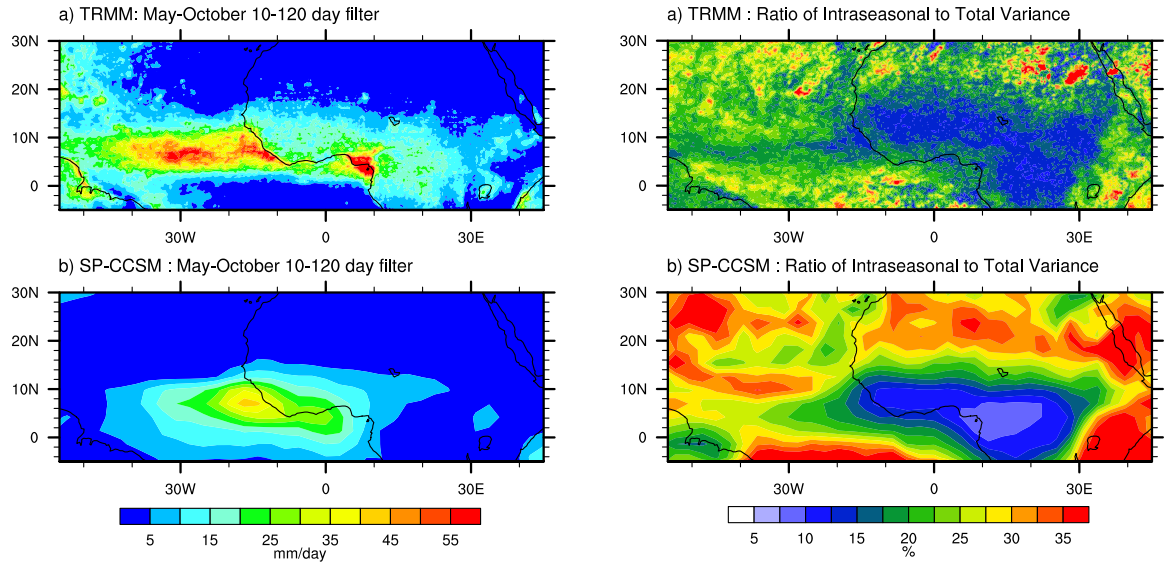


Figure 5.4. The variance of intraseasonal variability in precipitation from (a) TRMM and (b) SP-CCSM. The ratio of intraseasonal scale variance to total variance from (c) TRMM and (d) SP-CCSM. Intraseasonal variability is calculated by a 10-120 day bandpass filter. Variance is in mm $^{-2}$ day $^{-2}$. The ratio of the variances is shown as a percent of the total variance explained and is contoured from 0-40% by increments of 5%.

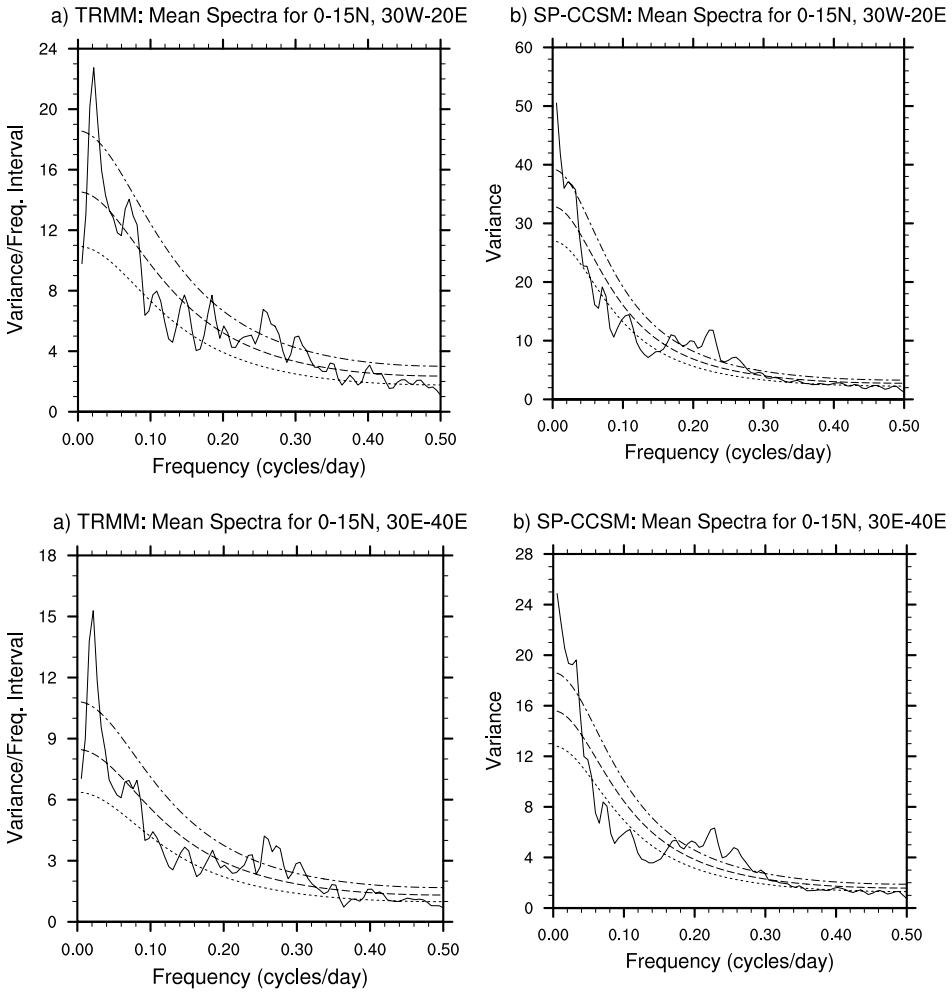


Figure 5.5. Power spectra of May-October TRMM (left) and SP-CCSM (right) averaged over the domain 0º-15ºN 30ºW-20ºE (left) and the domain 0º-15ºN 30ºE-40ºE (right). The smoothed seasonal cycle was removed before calculating the spectra. Also shown are the red noise background spectra and the 95% confidence limits.

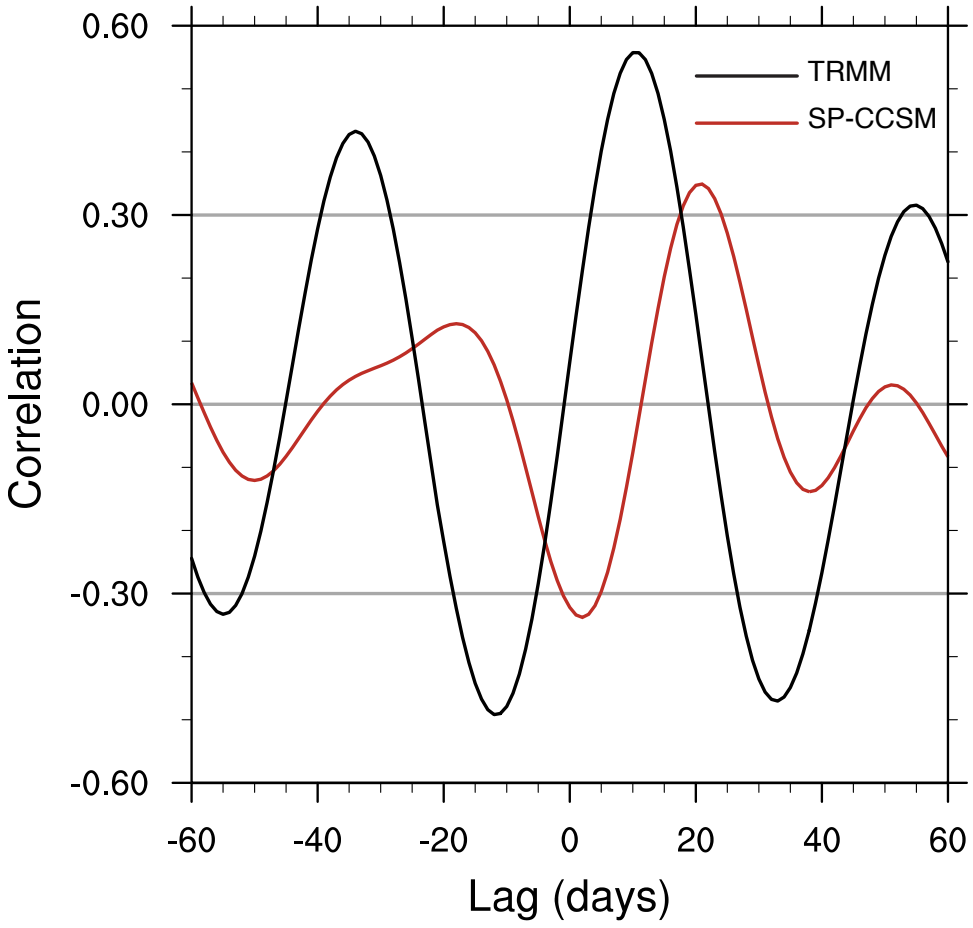


Figure 5.6. Power spectra of May-October TRMM (left) and SP-CCSM (right) averaged over the domain 0º-15ºN 30ºW-20ºE (left) and the domain 0º-15ºN 30ºE-40ºE (right). The smoothed seasonal cycle was removed before calculating the spectra. Also shown are the red noise background spectra and the 95% confidence limits.

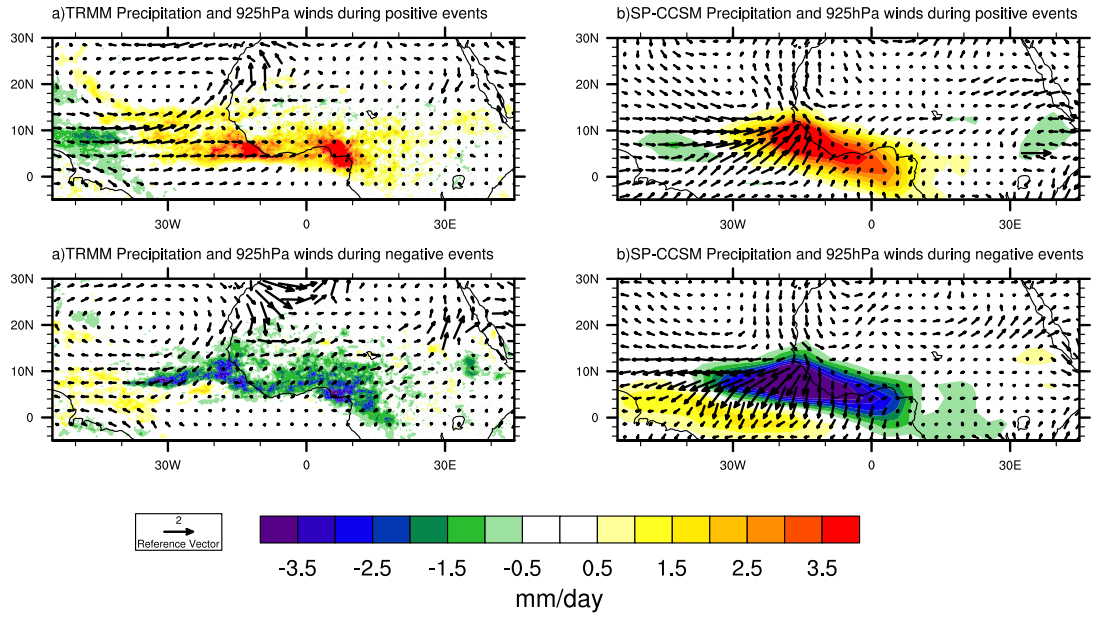


Figure 5.7. Composite precipitation (filled contours) and 925hPa winds (vectors) from TRMM/ ERA-Interim (left) and SP-CCSM (right) for positive (top) and negative (left) 30-90-day precipitation events that exceed one standard deviation. Precipitation anomalies are in units of mm day $^{-1}$. The reference vector is in m s $^{-1}$. and is shown in the bottom left.

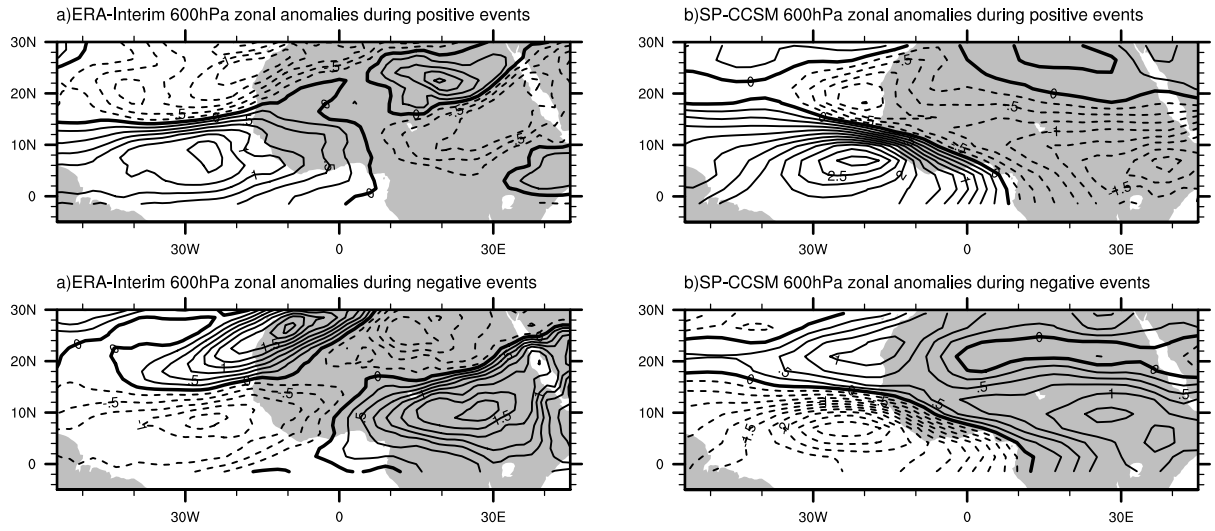


Figure 5.8. Composite 600 hPa zonal wind anomalies (AEJ level) from ERA-Interim (left) and SP-CCSM (right) for positive (top) and negative (left) 30-90-day precipitation events that exceed one standard deviation. Units are in m s $^{-1}$. Contours extend from by . Negative anomalies are dashed.

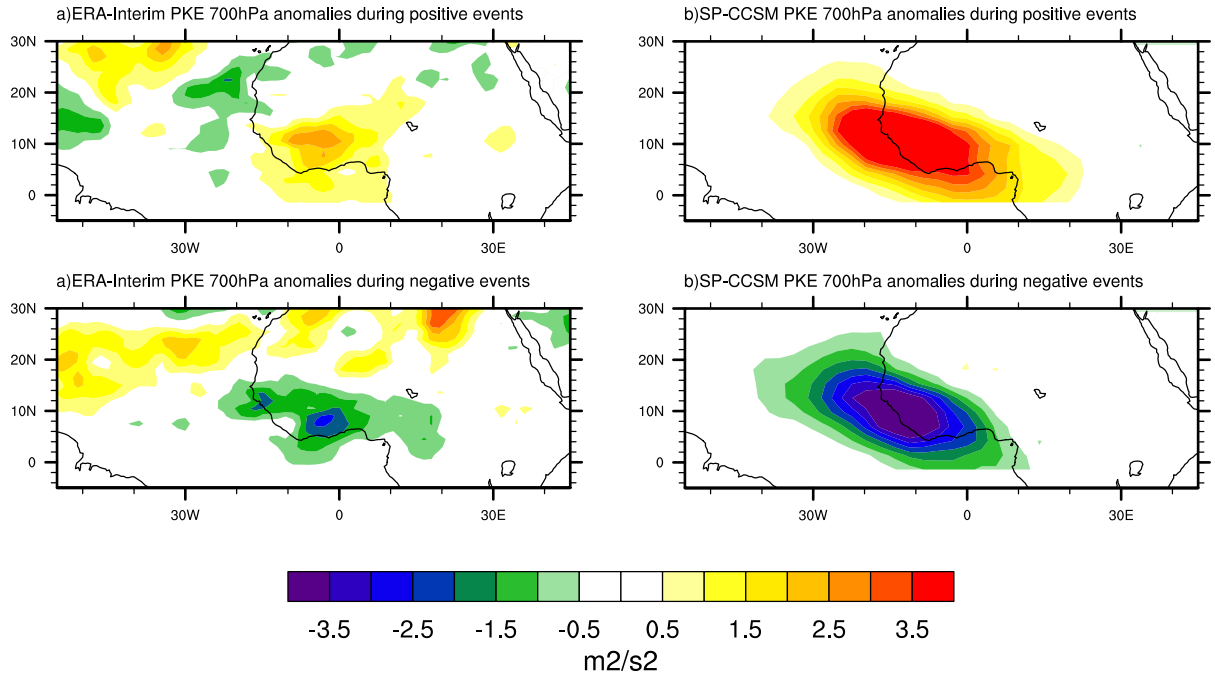


Figure 5.9. Composite 700 hPa EKE anomalies from ERA-Interim (left) and SP-CCSM (right) for positive (top) and negative (left) 30-90-day precipitation events that exceed one standard deviation. Units are in $m^2 s^{-2}$.

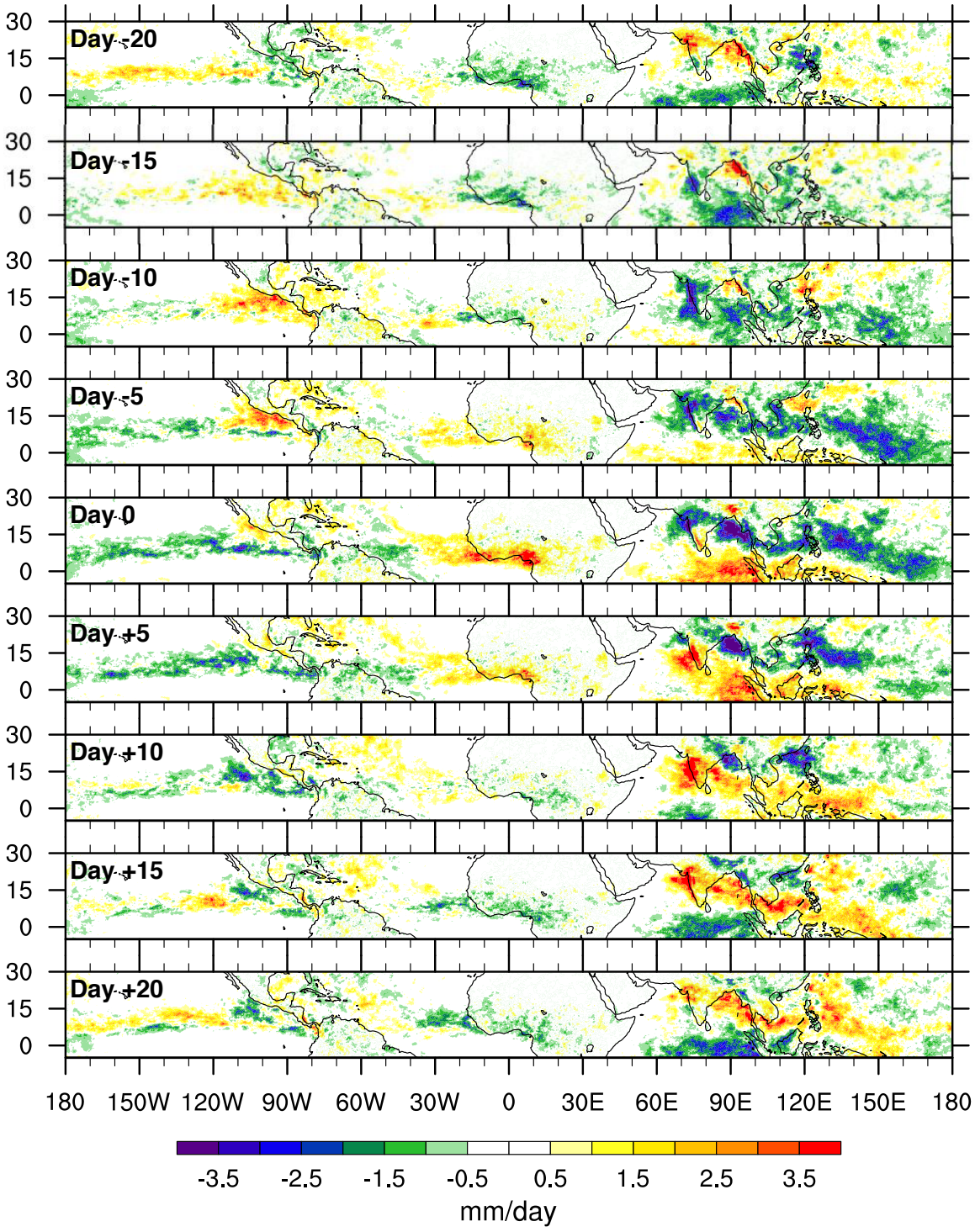


Figure 5.10. Lag composite maps of May-October TRMM precipitation based on positive events from the 30-90 day time series for -20 to 20 days every 5 days. Units are in mm day $^{-1}$.

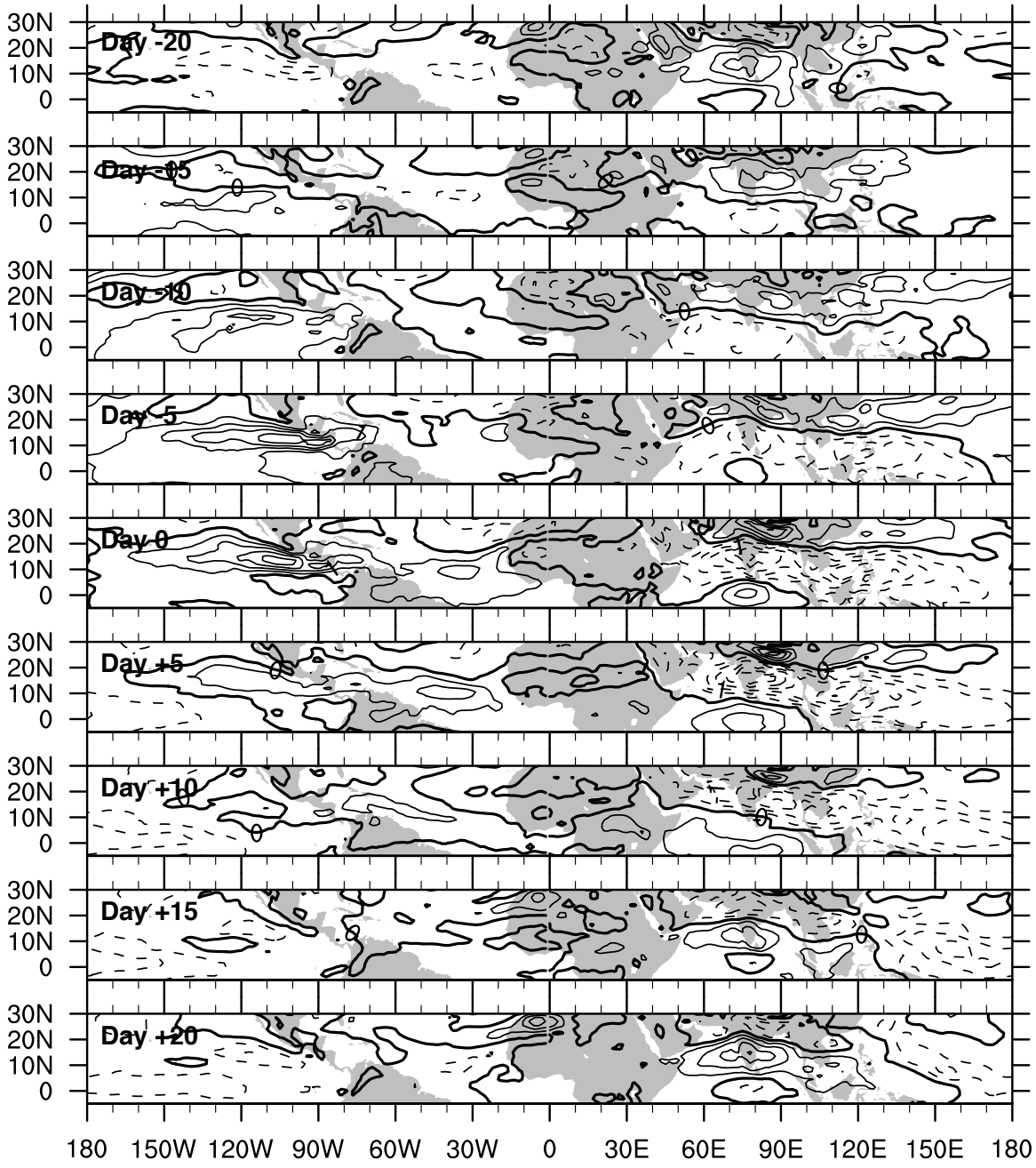


Figure 5.11. Lag composite maps of May-October ERA-Interim anomalous zonal 850-hPa winds based on positive events from the 30-90 day time series for -20 to 20 days every 5 days. Units are in m s $^{-1}$.

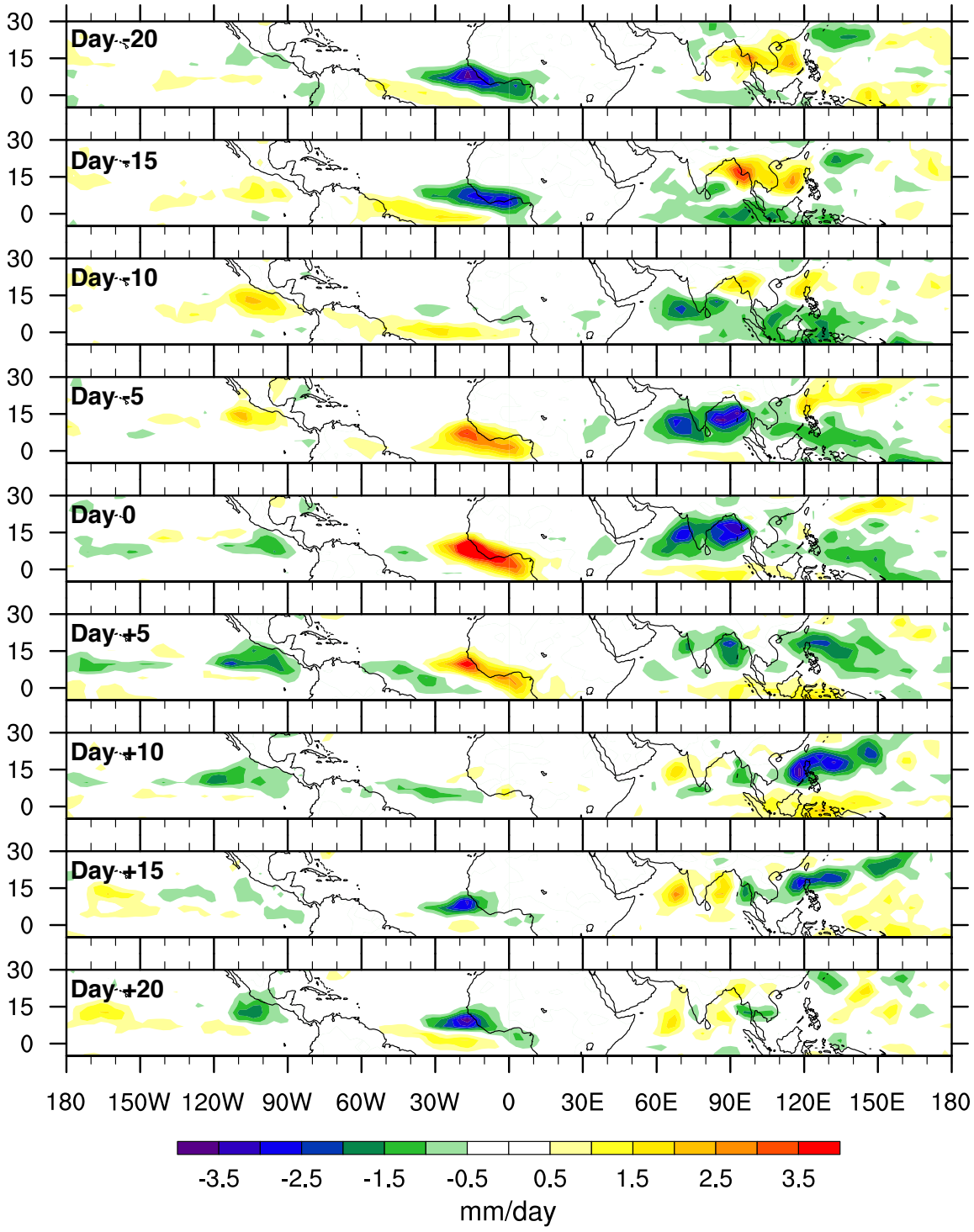


Figure 5.12. Lag composite maps of May-October SP-CCSM precipitation based on positive events from the 30-90 day time series for -20 to 20 days every 5 days. Units are in mm day $^{-1}$.

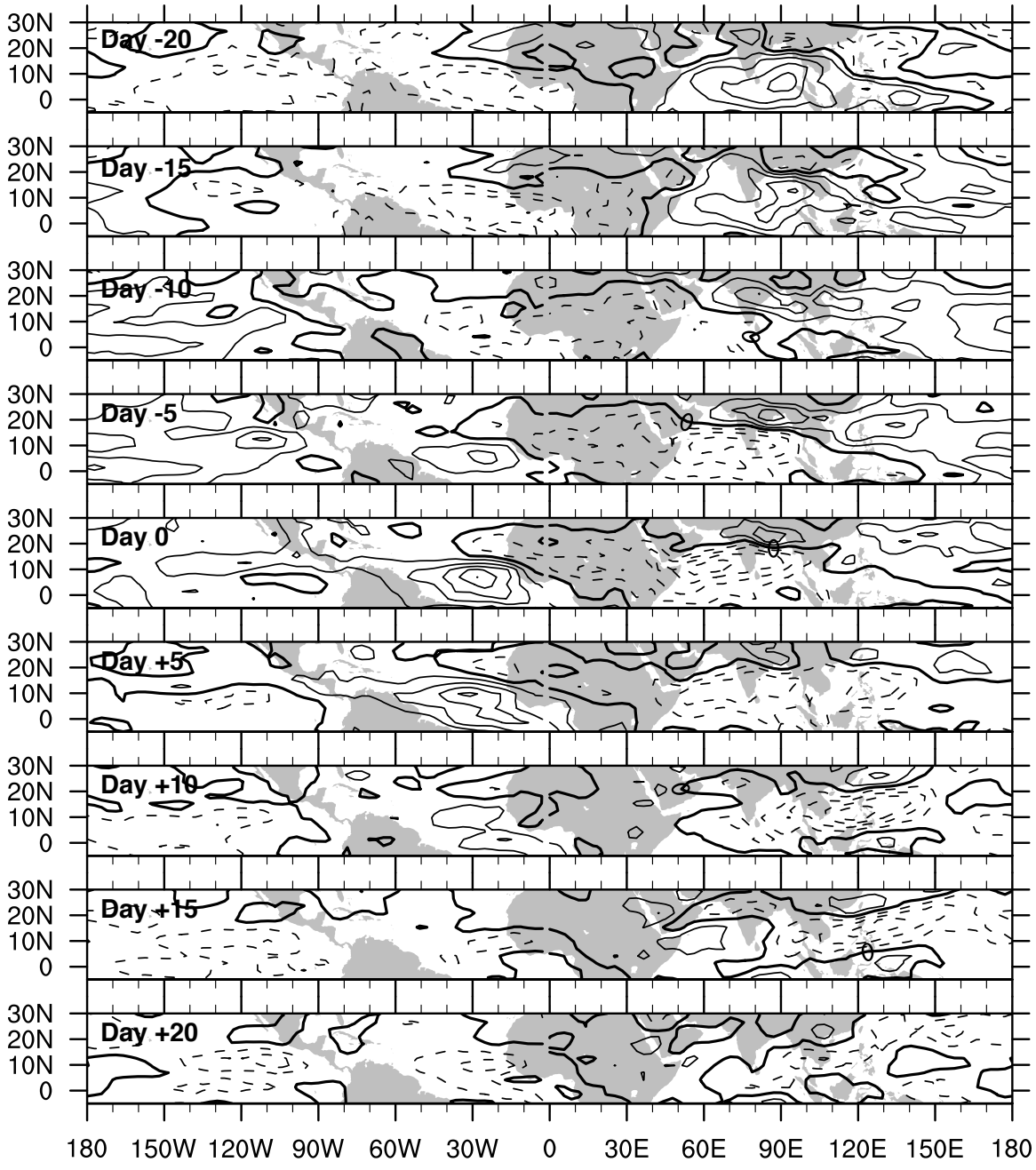


Figure 5.13. Lag composite maps of May-October SP-CCSM anomalous zonal 850-hPa winds based on positive events from the 30-90 day time series for -20 to 20 days every 5 days. Units are in m s^{-1}.

CHAPTER 6

CONCLUSIONS AND DISCUSSION

There is a need in the scientific community for improved simulations of the West African monsoon system. As the climate warms due to increasing greenhouse gas concentrations we can expect changes in rainfall variability and extremes over West Africa. Unfortunately there is currently no consensus about how precipitation can be expected to change over the next century. Arguably the large uncertainties associated with rainfall changes over West Africa are due to the poor skill of climate models in simulating the mean annual cycle and variability in monsoon precipitation.

This study has attempted to address the need for better model simulations by examining how embedding a 2D cloud resolving model in each gridbox changes the overall representation of the West African monsoon. Given the complex multiscale interactions known to be associated with the monsoon, the West African monsoon serves as a unique testbed for the superparameterization.

In this dissertation I have shown that adding the superparameterization to the CCSM shifts the seasonal mean position of peak rainfall from over the ocean in CCSM to over the continent in SP-CCSM. This shift implies that the northward propagation of monsoon rains is improved in the SP-CCSM. The biases in mean rainfall found in both models were shown to correspond with warm SST biases in the Gulf of Guinea and along the equatorial Atlantic. Anomalously warm SSTs in the Gulf of Guinea influence precipitation over West African in two

ways 1) increasing surface sensible and latent heat fluxes which provide energy for convection and 2) modifying the low-level meridional and zonal wind fields in such a way that the region of convergence is misrepresented. The SST biases are weaker in SP-CCSM compared to the CCSM which may help explain the northward shift of the monsoon in the SP-CCSM.

I also showed that the CMIP5 models exhibit marked variability in the mean position and magnitude of monsoon rainfall. Preliminary results suggest that the improved representation of the Atlantic cold tongue may increase the overall fidelity of the simulation of precipitation over West Africa. Further research will need to be done to test this hypothesis.

As previous studies have demonstrated, the addition of the superparameterization improves the representation of tropical variability and convectively coupled waves. This was the first study to examine the influence of the superparameterization on easterly wave activity. In the standard CCSM, little-to-no easterly wave activity was found to occur over West Africa. The SP-CCSM on the other hand was shown to produce overly active African easterly waves that are significantly larger in magnitude than observations. I have hypothesized that the overly active wave activity in SP-CCSM decreases the meridional gradients of temperature and moisture, thereby resulting in a weaker than observed African easterly jet.

Despite differences in the scale of the simulated waves, the horizontal and vertical structures of the waves in SP-CCSM are strikingly similar to observations. Two deficiencies I found in SP-CCSM were a limited development of shallow cumulus head of the region of deep convection and no signature of trailing stratiform precipitation behind the passage of the wave. Analysis of the eddy kinetic energy and eddy available potential energy tendencies indicates that AEWs in both ERA-I and SP-CCSM gain energy from the mean flow through barotropic energy

conversions and from baroclinic overturning. I also showed evidence to suggest that convection drives the generation, growth, and development of AEWs in SP-CSSM. Diabatic heating associated with the strong deep convection in SP-CCSM likely produces vertical temperature anomalies which are offset by changes in vertical velocity. These changes in vertical motion help provide energy to AEWs.

One question that remains unanswered is why easterly wave activity is significantly amplified over West Africa but is comparable in scale to observations over the west Pacific and Intra-America seas. It is possible that differences in the characteristics of convection over land compared to ocean may help explain the amplification of easterly waves over Africa. To test this idea the diagnostic methods used in Chapter 4 could be translated to AEWs over other tropical regions.

In the final results chapter of this dissertation (Chapter 5) I examined the intraseasonal variability of monsoon precipitation in the SP-CCSM. The variability in precipitation in CCSM is much weaker than observed, and intraseasonal variability in convection is practically non-existent so this model was not examined here. Consistent with observations, precipitation over West Africa in SP-CCSM was found to vary on 30-90 day timescales. Intraseasonal variations in precipitation act to amplify or suppress convection within the ITCZ along the coast of West African and in the Atlantic. Enhanced precipitation was found to be associated with a decrease in the trade winds resulting in enhanced onshore flow, a northward shift of the AEJ, and increased AEW activity.

I also showed that on intraseasonal timescales there is a potential link between suppressed convection in the Indo-Pacific region and enhanced precipitation over West Africa.

The SP-CCSM places us in a unique position to further examine the dynamical links between other modes of tropical variability and West African precipitation. Not only has this model been shown to do a reasonable job simulating the West African monsoon but, the MJO and the Asian summer monsoon are also well represented in SP-CCSM. Many models have difficulty simulating any of these features of tropical variability, here we have a model that is able to capture all three.

Based on the overall findings of the work presented here, we see that vastly different climate regimes are simulated for West African in the CCSM compared to the SP-CCSM. An fun way to think about the differences between the modeled realizations of the climate over West Africa and the actual climate over West Africa is to consider what it would be like to live in the model simulated climate. For example lets pretend we are living in Bamako, Mali and ask the question what would the rainy season be like if we lived in the world of CCSM or SP-CCSM?

As I have shown in this dissertation, average rain rates over West Africa are typically low in CCSM. This model also exhibits little-to-no synoptic or intraseasonal variability. What this indicates is that during the rainy season we would expect it to drizzle almost every day with very little variability in the total amount of rainfall falling on day-to-day time scales. We would also expect limited modulations of precipitation throughout the season - in other words the monsoon in CCSM does not experience oscillating active and break periods. My picture of the climate of West Africa in CCSM similar to what I might expect in Portland, Oregon or Scotland, although temperatures are much higher.

If we were living Bamako in the SP-CCSM realization of the world, we would expect the rainy season to be characterized by dramatic changes in the weather every 3-6 days. AEWs are a

robust feature of the climate over West Africa in SP-CCSM and we could expect to experience torrential down pours associated with the passage of these waves every 3-6 days throughout the rainy season. Rainfall rates during the passage of these storms would be significantly larger than what is seen in observations. We would also experience changes in the frequency of the passage of AEWs throughout the rainy season. Rainfall and AEW activity would be greater during active phases of the monsoon and weaker during suppressed monsoon phases.

The climates simulated by both models are very different from one another. Based on the findings from other modeling studies (e.g. Cook and Vizy, 2006) and the results from the CMIP5 model archive shown in Chapter 3, the climate models we use to understand and predict potential future climate change also show a wide variety of climate states over Africa. Given the broad range of realizations for representing the rainy season, it is not surprising that our estimations of future climate are highly uncertain.

The addition of the superparameterization improves the overall representation of the West African monsoon, particularly the variability in convection. It would be interesting to see how the superparameterization modifies the climate over West Africa in a large-scale model with higher resolution in both ocean and atmosphere models. This will soon be possible, as the superparameterization has been embedded in to CCSM4, a more up-to-date version of the community atmosphere model.

In closing, much of the work in this dissertation has honestly left me with nothing more than a million other questions I would like to answer. I hope to continue my work on the monsoon by further examining the relationship between Atlantic SSTs and precipitation over West Africa. I also plan to continue studying the relationship between convection and AEWs in

SP-CCSM. I am particularly interested in trying to determine if convection generates AEWs or if convection is a result of AEW activity and helps to amplify the waves.

REFERENCES

Alaka, G. J., Jr., and E. D. Maloney, 2012: The Influence of the MJO on Upstream Precursors to African Easterly Waves. *J. Climate*, **25**, 3219–3236. doi:10.1175/JCLI-D-11-00232.1

Avila, L. A., and R. J. Pasch, 1992: Atlantic tropical systems of 1991. *Mon. Wea. Rev.*, **120**, 2688–2696.

Baron, C., B. Sultan, M. balme, B. Sarr, T. Lebel, S. Janicot, and M. Dingkuhn, 2005: From GCM grid cell to agricultural plot: Scale issues affecting modeling of climate impact. *Philos. Trans. Roy. Soc. London*, **360B** (1463), 2095-2108.

Benedict, James J., David A. Randall, 2009: Structure of the Madden–Julian Oscillation in the Superparameterized CAM. *J. Atmos. Sci.*, **66**, 3277–3296. doi: http://dx.doi.org/10.1175/2009JAS3030.1

Berry, G., and C. D. Thorncroft, 2005: Case study of an intense African easterly wave. *Mon. Wea. Rev.,* **133**, 752–766.

Berry, G. J., and C. D. Thorncroft, 2012: African Easterly Wave Dynamics in a Mesoscale Numerical Model: The Upscale Role of Convection. *J. Atmos. Sci.*, **69**, 1267–1283. doi: http://dx.doi.org/10.1175/JAS-D-11-099.1

Boko, M., I. Niang, A. Nyong, C. Vogel, A. Githeko, M. Medany, B. Osman-Elasha, R. Tabo and P. Yanda, 2007: Africa. *Climate Change 2007: Impacts, Adaptation and Vulnerability. Contribution of Working Group II to the Fourth Assessment Report of the Intergovernmental Panel on Climate Change,* M.L. Parry, O.F. Canziani, J.P. Palutikof, P.J. van der Linden and C.E. Hanson, Eds., Cambridge University Press, Cambridge UK, 433-467.

Bonan, G. B., K. W. Oleson, M. Vertenstein, and S. Levis, 2002: The Land Surface Climatology of the Community Land Model Coupled to the NCAR Community Climate Model. *J. Climate,* **15**, 3123-3149.

Burpee, R. W., 1972: The origin and structure of easterly waves in the lower troposphere of North Africa. *J. Atmos. Sci.,* **29**, 77–90.

Burpee, R.W., 1974: Characteristics of North African easterly waves during the summers of 1968 and 1969. *J. Atmos. Sci.,* **31**, 1556–1570.

Caniaux, G., H. Giordani, J-L. Redelsperger, F. Guichard, E. Key, M. Wade, 2011: Coupling between the Atlantic cold tongue and the West African monsoon in boreal spring and summer. *J. Geophys. Res*., **116**, 1-17.

Carlson, T. N., 1969: Synoptic histories of three African disturbances that developed into Atlantic hurricanes. *Mon. Wea. Rev.,* **97**, 256–276.

Charney J. G., M. E. Stern, 1962: On the stability of internal baroclinic jets in a rotating atmosphere. *J. Atmos. Sci.,***19**, 159–172.

Collins, William D., and Coauthors, 2006: The Community Climate System Model Version 3 (CCSM3). *J. Climate*, **19**, 2122–2143. doi: http://dx.doi.org/10.1175/JCLI3761.1

Cook, K. H., 1999: Generation of the African easterly jet and its role in determining West African precipitation. *J. Climate*, **12(5)**, 1165–1184.

Cook, K. H., E. K. Vizy, 2006: Coupled Model Simulations of the West African Monsoon System: Twentieth- and Twenty-First-Century Simulations. *J. Climate*, **19**, 3681–3703. doi: http://dx.doi.org/10.1175/JCLI3814.1

Cook, K. H., 2008: Climate science: The mysteries of Sahel droughts. *Nature Geoscience*, **1**, 647-648. doi:10.1038/ngeo320

Daniell, P.J., 1946, Discussion on the symposium on autocorrelation in time series: J. Roy. Statist. Soc. (Suppl.), **8**, 88-90.

Dee, D. P. and coauthors, 2011: The ERA-Interim reanalysis: configuration and performance of the data assimilation system. *Quart. J. Royal. Met. Soc*., **137**, 553-597.

DeMott, C. A., C. Stan, D. A. Randall, J. L. Kinter III, and M. Khairoutdinov, 2011: The Asian Monsoon in the Superparameterized CCSM and Its Relationship to Tropical Wave Activity. *J. Climate*, **24**, 5134–5156. doi:10.1175/2011JCLI4202.1

Duvel, J. P., 1990: Convection over tropical Africa and the Atlantic Ocean during northern summer. Part II: Modulation by easterly waves. *Mon. Wea. Rev.,* **118**, 1855–1868.

Eltahir, E. A. B., and C. Gong, 1996: Dynamics of wet and dry years in West Africa. *J. Climate,* **9,** 1030–1042.

Food and Agriculture Organization of the United Nations (FAO), 2006: FAOSTAT Online Statistical Service. (Available online at http://faostat. fao.org.)

Fink, A. H., and A. Reiner, 2003: Spatiotemporal variability of the relation between African Easterly Jets and and West African Squall lines in 1998 and 1999. *J. Geophys. Res*., **108**, 4332, doi:10.1029/2002JD002816.

Fyfe, J. C., 1999: Climate simulations of African easterly waves. *J. Climate,* **12**, 1747–1769.

Gates, W. L., and Coauthors, 1999: An overview of the results of the Atmospheric Model Intercomparison Project (AMIP I). *Bull.*Amer. Meteor. Soc., **80**, 29–55.

Grist, J. P., 2002: Easterly waves over Africa. Part I: The seasonal cycle and contrasts between wet and dry years. *Mon. Wea. Rev.,* **130**, 197–211.

Gu, G., and R. F. Adler, 2004: Seasonal evolution and variability associated with the West African Monsoon System. *J. Climate,* **17,** 3364–3377.

Hack, J. J., 1994: Parameterization of moist convection in the National Center for Atmospheric Research community climate model (CCM2), *J. Geophys. Res.*, **99**, 5551–5568, doi:10.1029/93JD03478.

Hagos, S. M., and Cook, K. H. 2007: Dynamics of the West African Monsoon Jump. *J. Climate,* **20**, 5264–5284. doi:10.1175/2007JCLI1533.1

Hall, N.M.J and P. Peyrille, 2006: Dynamics of the West African monsoon. *J. Physique,* **139**, 81-99.

Hall N. M. J., G. N. Kiladis, C. D. Thorncroft, 2006: Three-dimensional structure and dynamics of African easterly waves. Part II: Dynamical modes. *J. Atmos. Sci.,* **63**, 2231–2245.

Hodges, B. J. Hoskins, J. Boyle, and C. D. Thorncroft, 2003: A comparison of recent reanalysis datasets using objective feature tracking: Storm tracks and tropical easterly waves. *Mon. Wea. Rev.,* **131**, 2012–2037.

Hopsch, S. B., C. D. Thorncroft, and K. R. Tyle, 2010: Analysis of African Easterly Wave Structures and Their Role in Influencing Tropical Cyclogenesis. *Mon. Wea. Rev.*, **138**, 1399–1419. doi: http://dx.doi.org/10.1175/2009MWR2760.1

Hoskins, B., R. Neale, M. Rodwell, and G.-Y. Yang, 1999: Aspects of the large-scale tropical atmospheric circulation. Tellus A, **51**, 33–44.

Hsieh, J-S., and K. H. Cook, 2005: Generation of African easterly wave disturbances: Relationship to the African easterly jet. *Mon. Wea. Rev.*, **113**, 1311-1327.

Hsieh, J-S., and K. H. Cook, 2007: A study of the energetics of African easterly waves using a regional climate model. *J. Atmos. Sci.*, **64**, 421-440.

Hsieh J-S, and K. H. Cook, 2008: On the instability of the African easterly jet and the generation of African waves: reversals of the potential vorticity gradient. *J. Atmos. Sci.* **65**, 2130–2151.

Huffman, G. J., R. F. Adler, D. T. Bolvin, G. Gu, E. J. Nelkin, K. P. Bowman, Y. Hong, E. F. Stocker, D.B. Wolff, 2007: The TRMM Multi-satellite Precipitation Analysis: Quasi- Global, Multi-Year, Combined-Sensor Precipitation Estimates at Fine Scale. *J. Hydrometeor.*, **8**, 38-55.

IPCC, 2007: Summary for Policymakers. In: *Climate Change 2007: The Physical Science Basis. Contribution of Working Group I to the Fourth Assessment Report of the Intergovernmental Panel on Climate Change* [Solomon, S., D. Qin, M. Manning, Z. Chen, M. Marquis, K. B. Averyt, M. Tignor and H. L. Miller (eds.)]. Cambridge University Press, Cambridge, United Kingdom and New York, NY, USA.

Janicot, S., and Sultan, B., 2001: Intra-seasonal modulation of convection in the West African monsoon. *J. Geophys. Res*, **28**, 523-526.

Janicot, S., F. Mounier, N. M. Hall, S. Leroux, B. Sultan, and G. N. Kiladis, 2009: Dynamics of the West African Monsoon. Part IV: Analysis of 25-90-Day Variability of Convection and the Role of the Indian Monsoon. *J. Climate*, **22**, 1541-1565.

Janicot, S., G. Caniaux, F. Chauvin, G. de Coëtlogon, B. Fontaine, N. Hall, G. Kiladis, 2011a: Intraseasonal variability of the West African monsoon. (J. Polcher, D. J. Parker, & A. T. Gaye, Eds.) *Atmospheric Science Letters*, ***12***, 58–66. doi:10.1002/asl.280

Joiner, E., D Kennedo, and J. Sampson: 2012. Vulerability to Climate Change in West Africa: Adaptive Capacity in the Regional Context. Climate Change and African Political Stability Student Working Paper No. 4. (J. W. Busby, K. L. White, T. G. Smith Eds.).

Khairoutdinov, M. F., and D.A. Randall, 2001: A cloud resolving model as a cloud parameterization in the NCAR Community Climate System Model: Preliminary Results. *Geophys. Res. Lett*., **28**, 3617-3620.

Khairoutdinov, M. F., and D. A. Randall, 2003: Cloud Resolving Modeling of the ARM Summer 1997 IOP: Model Formulation, Results, Uncertainties, and Sensitivities. *J. Atmos. Sci*., **60**, 607-625.

Khairoutdinov, M., D. Randall, and C. DeMott, 2005: Simulations of the Atmospheric General Circulation using a Cloud-Resolving Model as a Superparameterization of Physical Processes. *J. Atmos. Sci.*, **62**, 2136-2154.

Khairoutdinov, M., C. DeMott, and D. Randall, 2008: Evaluation of the Simulated Interannual and Subseasonal Variability in an AMIP-Style Simulation Using the CSU Multiscale Modeling Framework. *J. Climate*, **21**, 413-431.

Kiladis G. N., C. D. Thorncroft, N. M. J. Hall, 2006: Three-dimensional structure and dynamics of African easterly waves. Part I: Observations. *J. Atmos. Sci.* **63**, 2212–2230.

Kiladis, G. N., M. C. Wheeler, P. T. Haertel, K. H. Straub, and P. E. Roundy, 2009: Convectively coupled equatorial waves, *Rev. Geophys.*, **47**, RG2003, doi 10.1029/2008RG000266.

Kwon, H.J., 1989: A reexamination of the genesis of African waves. *J. Atmos. Sci*, **46**, 3621-3631.

Lafore, J. P., C. Flamant, V. Giraud, F. Guichard, P. Knippertz, J. F. Mahfouf, P. Mascart, 2010: Introduction to the AMMA Special Issue on "Advances in understanding atmospheric processes over West Africa through the AMMA field campaign. *Quart. J. Roy. Meteor. Soc*, **136**, 2–7. doi:10.1002/qj.583

Lau, Kai-Hon, Ngar-Cheung Lau, 1992: The Energetics and Propagation Dynamics of Tropical Summertime Synoptic-Scale Disturbances. *Mon. Wea. Rev.*, **120**, 2523–2539. doi: http://dx.doi.org/10.1175/1520-0493(1992)120<2523:TEAPDO>2.0.CO;2

Lavaysse, C., C. Flamant, S. Janicot, D. J. Parker, J. P. Lafore, B. Sultan, and J. Pelon, 2009: Seasonal evolution of the West African heat low: a climatological perspective. *Climate Dynamics*, **33**, 313–330. doi:10.1007/s00382-009-0553-4

Lavender, S. L. and A. J. Matthews, 2009: Response of the West African Monsoon to the Madden–Julian Oscillation. *J. Climate*, **22**, 4097–4116. doi:10.1175/2009JCLI2773.1

Leroux, S., N. M. J. Hall, and G. N. Kiladis, 2010: A climatological study of transient-mean-flow interactions over West Africa. *Quart. J. Royal. Met. Soc*, **136**, 397–410. doi:10.1002/qj.474

Liebmann B. and C.A. Smith, 1996: Description of a Complete (Interpolated) Outgoing Longwave Radiation Dataset. *Bull. Amer. Meteor. Soc.,* **77**, 1275-1277.

Lin, X., and R.H. Johnson, 1996: Kinematic and Thermodynamic Characteristics of the flow over the Western Pacific Warm Pool during TOGA/COARE. *J. Atmos. Sci.*, **53**, 695-715

Maloney, E. D., and D. L. Hartmann, 1998: Frictional moisture convergence in a composite lifecycle of the Madden–Julian oscillation. *J. Climate*, **11**, 2387–2403.

Maloney, E. D., and S. K. Esbensen, 2007: Satellite and buoy observations of boreal summer intraseasonal variability in the tropical northeast Pacific. *Mon. Wea. Rev.*, **135**, 3–19.

Maloney, E. D. and J. Shaman, 2008: Intraseasonal Variability of the West African Monsoon and Atlantic ITCZ. *J. Climate*, **21**, 2898–2918. doi:10.1175/2007JCLI1999.1

Mass, C., 1979: A linear primitive equation model of African wave disturbances. *J. Atmos. Sci.*, **36**, 2075-2092.

Mathon, V., H. Laurent, and T. Lebel, 2002: Mesoscale Convective System Rainfall in the Sahel. *J. App. Meteo.*, **41**, 1081-1092.

Matthews, Adrian J., 2004: Intraseasonal Variability over Tropical Africa during Northern Summer. *J. Climate*, **17**, 2427–2440.
doi: http://dx.doi.org/10.1175/1520-0442(2004)017<2427:IVOTAD>2.0.CO;2

Mekonnen, A., C. D. Thorncroft, and A. R. Aiyyer, 2006: Analysis of convection and its association with African easterly waves. *J. Climate*, **19**, 5405–5421.
doi: http://dx.doi.org/10.1175/JCLI3920.1

Mitchell, T., and J. M. Wallace, 1992: The annual cycle in equatorial convection and sea surface temperature. *J. Climate,* **5,** 1140– 1156.

Mitchell, T. and Jones, 2005: An improved method of constructing a database of monthly climate observations and associated high-resolution grids. *Int. J. Climatology*, **25**, 693-712, Doi: 10.1002/joc.1181.

Mounier, F., S. Janicot, G. N. Kiladis, 2008: The West African Monsoon Dynamics. Part III: The Quasi-Biweekly Zonal Dipole. *J. Climate*, **21**, 1911–1928. doi:10.1175/2007JCLI1706.1

Ndomba, P.M., 2010: Development of rainfall curves for crops planting dates: a case study of Pangani River Basin in Tanzania. *Nile Basing Water Science and Engineering Journal*, **3**, 13-27.

Nguyen, H., C. D. Thorncroft, and C. Zhang, 2011: Guinean coastal rainfall of the West African Monsoon. *Q. J. R. Meteorol. Soc,* DOI:10.1002/qj.867.

Nicholson, S.E, 2000: The nature of rainfall variability over Africa on time scales of decades to millenia. Global and Planetary Change 26, 137–158

Norquist DC, Recker EE, Reed RJ. 1977. The energetics of African wave disturbances as observed during phase III of GATE. *Mon. Weather Rev.* **105**:334–342.

Okumura and Xie (2004) Interaction of the Atlantic Equatorial Cold Tongue and the African Monsoon. *J. Climate*, **17**, 3589-3602.

Ramel R., H. GallTe, C. Messager, 2006: On the northward shift of the west african monsoon. *Clim Dynm,* **26**, 429–440.

Randall, D., M. Khairoutdinov, A. Arakawa, and W. Grabowski, 2003: Breaking the Cloud Parameterization Deadlock. *Bull. Amer. Meteor. Soc.*, 1547-1564.

Reed, R.J., D. C. Norquist, and E. E. Recker, 1977: The structure and properties of African wave disturbances as observed during Phase III of GATE. *Mon. Wea. Rev.,* **105***, 317–333.*

Rennick, M. A., 1976: The generation of African waves. *J. Atmos. Sci.*, **33**, 1955–1969.

Reynolds, R. W., T. M. Smith, C. Liu, D. B. Chelton, K. S. Casey, and M. G. Schlax, 2007: Daily High-Resolution-Blended Analyses for Sea Surface Temperature. *J. Climate*, **20**, 5473–5496. doi:10.1175/2007JCLI1824.1

Richter I,, S.-P. Xie, 2008: On the origin of equatorial Atlantic biases in coupled general circulation models. *Clim Dyn.,* **31**, 587–598.

Rockström, J., and Coauthors, 2004: A watershed approach to upgrade rainfed agriculture in water scarce regions through water system innovations: An integrated research initiative on water for food and rural livelihoods in balance with ecosystem functions. *Phys. Chem. Earth,* **29**, 1109–1118.

Ruti, P. M., A. Dell'Aquila, 2010: The twentieth century African easterly waves in reanalysis systems and IPCC simulations, from intra-seasonal to inter-annual variability. *Clim Dyn.*, **35**, 1099-1117.

Sander, N., and S. C. Jones, 2008: Diagnostic measures for assessing numerical forecasts of African Easterly waves. *Meteorol. Z.*, **17**, 209 - 220. doi: 10.1127/0941-2948/2008/0269.

Serra, Y. L., G. N. Kiladis, M. F. Cronin, 2008: Horizontal and Vertical Structure of Easterly Waves in the Pacific ITCZ. *J. Atmos. Sci.*, **65**, 1266–1284. doi: http://dx.doi.org/10.1175/2007JAS2341.1

Serra Y. L., G. N. Kiladis, K. I. Hodges, 2010. Tracking and mean structure of easterly waves over the Intra-Americas Sea. *J. Climate*. **23**:4823–4840.

Simmons, A. J., 1977: A note on the instability of the African easterly jet. *J. Atmos. Sci.*, **34**, 1670–1674.

Smith, R. D., and P. R. Gent, Eds., 2002: Reference manual for the Parallel Ocean Program (POP): Ocean component of the Community Climate System Model (CCSM2.0 and 3.0). Los Alamos National Laboratory Tech Rep. LA-UR-02-2484, 75 pp. [Available online at http:// www.cesm.ucar.edu/models/ccsm3.0/pop/doc/manual.pdf.]

Sultan, B., and S. Janicot, 2000: Abrupt shift of the ITCZ over West Africa and intra-seasonal variability. *Geophys. Res. Lett*. **27**, 3353. doi:10.1029/1999GL011285

Sultan, B., S. Janicot, and A. Diedhiou, 2003: The West African monsoon dynamics. Part I: Documentation of intraseasonal variability. *J. Climate*, **16**, 3389–3406.

Sultan, B., and S. Janicot, 2003: The West African monsoon dynamics. Part II: The "preonset" and 'onset' of the summer monsoon. *J. Climate*, **16**, 3407–3427.

Sundqvist, H., 1988: Parameterization of condensation and associated clouds in models for weather prediction and general circulation simulation. Physically Based Modelling and Simulation of Climate and Climate Change, M. E. Schlesinger, Ed., Kluwer Academic, 433–461.

Stan, C., M. Khairoutdinov, C. A. DeMott, V. Krishnamurthy, D. M. Straus, D. A. Randall, J. L. Kinter, J. L. III, 2010: An ocean-atmosphere climate simulation with an embedded cloud resolving model. *Geophys. Res. Lett*., **37**, doi:10.1029/2009GL040822

Tarhule, Aondover, Zakari Saley-Bana, Peter J. Lamb, 2009: Rainwatch. *Bull. Amer. Meteor. Soc.*, **90**, 1607–1614. doi: http://dx.doi.org/10.1175/2009BAMS2697.1

Taylor, C. M., D. J. Parker, N. Kalthoff, M. A. Gaertner, N. Philippon, S. Bastin, P. P. Harris, 2011: New perspectives on land-atmosphere feedbacks from the African Monsoon Multidisciplinary Analysis. (J. Polcher, D. J. Parker, & A. T. Gaye, Eds.) *Atmospheric Science Letters*, **12**, 38–44. doi:10.1002/asl.336

Taylor, K.E., R.J. Stouffer, G.A. Meehl, 2012: An Overview of CMIP5 and the experiment design. *Bull. Amer. Meteor. Soc.*, **93**, 485-498. doi:10.1175/BAMS-D-11-00094.1.

Thayer-Calder, K. and D.A. Randall, 2009: The Role of Convective Moistening in the Madden-Julian Oscillation. *J. of Atmos. Sci.*, **66**, 3297-3312.

Thorncroft C. D., and B. J. Hoskins, 1994a: An idealized study of African easterly waves. I: A linear view. *Q. J. R. Meteorol. Soc,* **120**, 953–982.

Thorncroft C.D., B.J. Hoskins, 1994b: An idealized study of African easterly waves. II: A nonlinear view. *Q. J. R. Meteorol. Soc.* **120**, 983–1015.

Thorncroft, C. D., 1995: An idealized study of African easterly waves. Part III: More realistic basic states. *Quart. J. Roy.* Meteor. Soc., **121,** 1589–1614.

Thorncroft, C.D. , and K. I. Hodges, 2001: African easterly wave variability and its relationship to Atlantic tropical cyclone activity. *J. Climate,* **14,** 1166–1179.

Thorncroft CD, Hall NMJ, Kiladis GN. 2008. Three-dimensional structure and dynamics of African easterly waves. Part III: Genesis. *J. Atmos. Sci.* **65**:3596–3607.

Tompkins, Adrian M., Laura Feudale, 2010: Seasonal Ensemble Predictions of West African Monsoon Precipitation in the ECMWF System 3 with a Focus on the AMMA Special Observing Period in 2006. *Wea. Forecasting*, **25**, 768–788. doi: http://dx.doi.org/10.1175/2009WAF2222236.1

Vizy, E. K., and K. H. Cook, 2001: Mechanisms by which Gulf of Guinea and Eastern North Atlantic sea surface temperatures can influence African rainfall. *J. Climate*, **14**, 795-821.

Wang, B., and Coauthors, 2008: Advance and prospectus of sea- sonal prediction: Assessment of the APCC/CliPAS 14-model ensemble retrospective seasonal prediction (1980–2004). *Climate Dyn.*, **33**, 93–117, doi:10.1007/s00382-008-0460-0.

Wheeler, M., and G. N. Kiladis, 1999: Convectively coupled equatorial waves: Analysis of clouds in the wavenumberfrequency domain. *J. Atmos. Sci.*, **56,** 374–399.

Wheeler, M., G. N. Kiladis, P. J. Webster, 2000: Large-Scale Dynamical Fields Associated with Convectively Coupled Equatorial Waves. *J. Atmos. Sci.*, **57**, 613–640. doi: http://dx.doi.org/10.1175/1520-0469(2000)057<0613:LSDFAW>2.0.CO;2

Wu, M.-L. C., O. Reale, S. D. Schubert, M. J. Suarez, R. D. Koster, and P. J. Pegion, 2009: African Easterly Jet: Structure and Maintenance. *J. Climate*, **22**, 4459–4480. doi: 10.1175/2009JCLI2584.1

Xuem S, and J. A. Carton, 2004: Tropical Atlantic variability: Patterns, mechanisms, and impacts. *Earth Climate: The Ocean–Atmo- sphere Interaction, Geophys. Monogr.,* Amer. Geophys. Union, 121–141.

Yang, Gui-Ying, Julia Slingo, 2001: The Diurnal Cycle in the Tropics. *Mon. Wea. Rev.*, **129**, 784–801.doi: http://dx.doi.org/10.1175/1520-0493(2001)129<0784:TDCITT>2.0.CO;2

Zhang, G. J. and N. McFarlane, 1995: Role of convective-scale momentum transport in climate simulation. *Journal of Geophys. Res*. **100**. 148-227.

Zhang, C., P. Woodworth, G. Gu, 2007: The seasonal cycle in the lower troposphere over West Africa from sounding observations. *Quart. J. Royal. Met. Soc.*, **132**, 2559–2582. doi: 10.1256/qj.06.23